ABSTRACT

Title of Document: COMPLEX METAL OXIDE THIN FILM GROWTH BY METALORGANIC CHEMICAL VAPOR DEPOSITION

Seung-Yeul Yang, Doctor of Philosophy, 2005

Directed By: Professor Ramamoorthy Ramesh,
Department of Materials Science and Engineering

The phenomenon of ferroelectricity recently attracted great attention with the successful advances in the development of thin-film fabrication. This development enables the integration of ferroelectric materials directly into device fabrication processes such as MEMS and FeRAMs. The stringent need for high-density, high-speed, and low-power memory devices has prompted an immense interest in studying the size effects in ferroic systems. The thickness dependence of ferroelectricity and critical thickness, which is the thickness limit when the ferroelectricity disappears, has become an issue of tremendous interest for both scientific and technological point of view. In parallel, current nonvolatile memory manufacturing processes inevitably require a scalable process such as metal-organic chemical vapor deposition (MOCVD) to deposit the ferroelectric layers.

The process controls as well as the ferroelectric and piezoelectric properties of two ferroelectric material systems, lead zirconate titanate (PZT) and bismuth ferrite

(BFO), prepared by MOCVD is presented in this dissertation. A systematic study on deposition process control such as stoichiometric composition, structure change and growth temperature was carried out.

The scaling of ferroelectric properties with film thickness in PZT films has been investigated. PZT films show bulk-like properties for thickness above ~20 nm. It was observed that a progressive decrease in the ferroelectric polarization as well as the piezo-response as the thickness is decreased; films as thin as 3.6 nm are piezoelectric. In this work, the interpretation of the origins of this decrease as well as results of the MOCVD processing studies is studied.

Epitaxial BFO thin film, which is an interesting candidate for Pb-free ferro / piezoelectrics, was grown by MOCVD as the first challenge. The film composition and phase equilibrium are sensitive to the Bi:Fe supply ratio of precursors. In the optimized condition, an epitaxial single perovskite phase thin films were obtained. Electrical measurements using both quasi-static hysteresis and pulsed polarization measurements confirm the existence of ferroelectricity with a switching polarization of 110-120 μC/cm^2, ΔP (= P^* - $P^\wedge$). Out-of plane piezoelectric (d_{33}) measurements using an atomic force microscope yield a value of 50 – 55 pm/V.

COMPLEX METAL OXIDE THIN FILM GROWTH BY METALORGANIC CHEMICAL VAPOR DEPOSITION

By

Seung-Yeul Yang

Dissertation submitted to the Faculty of the Graduate School of the
University of Maryland, College Park, in partial fulfillment
of the requirements for the degree of
Doctor of Philosophy
2005

Advisory Committee:
Professor Ramamoorthy Ramesh, Chair/Advisor
Professor John N. Kidder, Jr.
Professor Ichiro Takeuchi
Professor Lourdes G. Salamanca-Riba
Professor Raymond A. Adomaitis

© Copyright by
Seung-Yeul Yang
2005

DEDICATION

To my mother and father…

ACKNOWLEDGEMENTS

First and foremost, I would like to express my sincere gratitude to my advisor, Prof. R. Ramesh, for his support, patience, and encouragement throughout my Ph. D. studies. His enthusiasm and the drive for the scientific pursuit were essential to the completion of this dissertation and have taught me innumerable lessons and insights on the research. I can never thank you enough to give me the opportunity to work on this challenging and exciting project.

I also would like to thank my former advisor Prof. J. Kidder for introducing me to the research of the metal oxide CVD. His guidance and assistance in getting my research started on the right foot have led me to fruitful goal. I have benefited from valuable discussions on design and set-up for the CVD system as well as the basic theory on the thin film growth. This dissertation is part of the research carried out through his vision throughout my research.

I am also grateful to Prof. L. Salamanca-Riba, Prof. I. Takeuchi and Prof. R. Adomaitis for taking time out of their busy schedules to review my work.

I am fortunate to have the opportunity to work with intelligent and energetic group collaborators, Dr. Florin Zavaliche, Dr. Tong Zhao, Ladan Mohaddes-Ardabili, Dr. Haimei Zheng, Jun Ouyang, Junling Wang, Dr. Bao-Ting Liu, A. Prasertchoung, and Dr. V. Nagarajan. Many parts of this dissertation would be impossible if it were not for the collaboration with you and it is your friendships and invaluable discussions that make the work for Ph. D. more precious.

I specially thank Dr. Florin Zavaliche for enlightening discussions on ferroelectrics and constant encouraging during my research.

I also want to show my gratitude to all the CONCEPT members at Berkeley for giving me helpful suggestions and assistance.

Finally, I would like to thank my wife So-Young and my lovely daughter Soomin for their understanding and love during my journey. Their support and encouragement was in the end what made this dissertation possible. It would have never been possible to have my research career without my parents' love, dedication and their faith in me. I would like to thank my sisters and family for their love and support. I own everything I achieved to them. This dissertation is dedicated to them.

TABLE OF CONTENTS

DEDICATION ii

ACKNOWLEDGEMENTS iii

TABLE OF CONTENTS v

LIST OF TABLES vii

LIST OF FIGURES viii

Chapter 1: Introduction 1
1.1 Ferroelectric materials 1
1.2 $Pb(Zr,Ti)O_3$ 4
1.3 Ferroelectric Random Access Memory (FeRAM) 10
1.4 Metal Organic Chemical Vapor Deposition (MOCVD) 12
1.5 Theoretical analysis in ferroelectric films 22

Chapter 2: Experimental techniques used in this study 25
2.1 Precursors for PZT film growth 25
2.2 Liquid delivery system (LDS) MOCVD 28
2.2.1 Lquid delivery system (LDS) 28
2.2.2 MOCVD system 29
2.3 Conductive metal oxide thin film growth 32
2.3.1 RF sputtering 33
2.3.2 Pulsed laser deposition (PLD) 34
2.4 Device fabrication 35
2.5 Characterization 37
2.5.1 X-ray Diffraction (XRD) 37
2.5.2 Rutherford backscattering (RBS) 38
2.5.3 Ferroelectric property characterization 40
2.5.4 Capacitance-Voltage measurement 42
2.5.5 Piezoelectric force microscopy (PFM) 42

Chapter 3: $Pb(Zr_{0.5}Ti_{0.5})O_3$ thin film growth on Si 45
3.1 Background 45
3.2 Growth condition control 47
3.3 Structural and electrical properties of $Pb(Zr_{0.5}Ti_{0.5})O_3$ films 54
3.4 Comparison of piezoelectric properties of different thickness and composition 63
3.5 Discussion 67

Chapter 4: Thickness effects in epitaxial $Pb(Zr,Ti)O_3$ films grown by MOCVD 69
4.1 Background 69

4.2 Thickness effects in PZT thin films : a model system 73
4.3 The thickness effects in $Pb(Zr_{0.2}Ti_{0.8})O_3$ thin films 80
4.4 Disccussion 95

Chapter 5: $BiFeO_3$ thin film growth by MOCVD... 97
5.1 Background 97
5.2 Growth conditions.. 99
5.3 Crystal structure 103
5.4 Surface morphology and Electrical properties... 105
5.5 Discussion 111

Chapter 6: Summary and future work.. 114

LIST OF TABLES

Table 2-1. Deposition parameters of PZT films prepared by liquid delivery MOCVD……………………………………………………………..29
Table 5-1. Deposition parameters of BFO films prepared by liquid delivery MOCVD……………………………………………………………..98

LIST OF FIGURES

Figure 1-1. Hysteresis loop in ferroelectric materials……………………………………2
Figure 1-2. The phase diagram of $PbZrO_3$ - $PbTiO_3$ solid solution system…………...4
Figure 1-3. The ABO_3 perovskite structure…………………………………………...6
Figure 1-4. (a) Ferroelectric and (b) Piezoelectric properties of $Pb(Zr_{1-x}Ti_x)O_3$……...8
Figure 1-5. Trend of Cell Circuit Architecture and Cell Capacitor Structure……….10
Figure 1-6. SEM images of PZT film deposited on a patterned substrate…………...12
Figure 1-7. Cross-sectional SEM images. PZT films grown on (a) 17 μm wide (2 : 1 aspect ratio) and (b) 5 μm wide (6 : 1 aspect ratio) 3-D trench structures……………………………………………………………13
Figure 1-8. Chemical structure of (a) β-diketonates and (b) its complex (tetramethyl-heptanedionate (thd))…………………………………………………17
Figure 1-9. Schematic diagram of MOCVD with conventional bubbler system…….18
Figure 1-10. Operation sequence in LDS MOCVD…………………………………20

Figure 2-1. The thermogravimetric (TG) curves show the good thermal compatible behavior for $Zr(dmhd)_4$ with $Pb(thd)_2$ and $Ti(O\textit{i}Pr)_2(thd)_2$……………25
Figure 2-2. Liquid line manifold…………………………………………………..26
Figure 2-3. The schematic of liquid delivery MOCVD system…………………...…28
Figure 2-4. The growth rate dependence of the liquid source supply rate…………...30
Figure 2-5. RF sputtering configuration.……………………………………………31
Figure 2-6. Schematic of PLD system………………………………………………33
Figure2-7. Sample structure after device fabrication……………………………...34
Figure 2-8. XRD measurement techniques………………………………………..35
Figure 2-9. RBS result for a sample of PZT film on STO substrate…………………36
Figure 2-10. Signal drive profile for hysteresis polarization measurement…………37
Figure 2-11. Sequence of voltage pulses……………………………………………38
Figure 2-12. Switching (P^*) and non-switching ($P^\wedge$) polarization…………………...38
Figure 2-13. Schematic of the experimental setup for piezoelectric measurements…39

Figure 3-1. Growth of epitaxial STO films on Si substrate…………………………44
Figure 3-2. The relation of atomic percent of Pb, Zr and Ti of PZT films was measured by RBS with precursor mixing ratio prepared at 650 ^oC and the same volume ratio (V(Pb) / V(Zr) = 1) of Pb and Zr precursors was used during deposition at 650 ^oC……………………………………45
Figure 3-3. The variation of Pb atomic percent grown at 650 ^oC with different liquid supply flow rate……………………………………………………..47
Figure 3-4. The effect of Pb stoichiometry on ferroelectric properties of PZT films……………………………………………………………….....48
Figure 3-5. Composition dependence on growth temperature………………………49
Figure 3-6. θ - 2θ XRD patterns from films deposited at different temperature…….50

Figure 3-7. (a) P-E hysteresis loops and (b) Switched polarization ($\Delta P = P^* - P_r$ (~ $2P_r$)) from films deposited at different temperature…………………...51
Figure 3-8. The dependence of oxygen flow rate on the film growth (a) O_2 : 0 sccm and (b) O_2 : 300 sccm. ………………………………………………52
Figure 3-9. A typical θ-2θ x-ray diffraction scan and ϕ-scan of LSCO/ PZT/LSCO capacitors deposited on STO/Si at 650 °C……………………………..53
Figure 3-10. The hysteresis response of 230 nm thick $Pb(Zr_{0.5}Ti_{0.5})$ capacitor sandwiched by LSCO electrodes at 1 V, 3 V and 5 V………………....54
Figure 3-11. Capacitance vs applied voltage measured with 230 nm thick $Pb(Zr_{0.5}Ti_{0.5})$ capacitor sandwiched by LSCO electrodes……………...55
Figure 3-12. Polarization (switched (P^*) – non-switched ($P^\wedge$)) and coercive voltage of LSCO/PZT/LSCO capacitors as a function of applied voltage……..56
Figure 3-13. Pulse-width dependence of polarization (switched (P^*) – non-switched ($P^\wedge$)) of LSCO/PZT/LSCO capacitors measured at 3V and 5 V, respectively……………………………………………………….…57
Figure 3-14. Fatigue resistant characteristics of LSCO/PZT/LSCO capacitors as a function of bipolar-pulsed cycles measured at 3 V and 5 V, respectively…………………………………………….……………58
Figure 3-15. Retention characteristics of LSCO/PZT/LSCO capacitors as a function of time measured at 3 V and 5 V, respectively………………………...59
Figure 3-16. Piezoelectric hysteresis loops of 230 nm and 1, 3, 5 μm-thick $Pb(Zr_{0.5}Ti_{0.5})O_3$ films……………………………………………….....60
Figure 3-17. The changes of piezoelectric coefficient (d_{33}) and coercive field (E_c) with film thickness; ○ d_{33} of PZT films, ■ E_c of PZT films…………62
Figure 3-18. The changes of piezoelectric coefficient (d_{33}) with change of Ti/(Zr+Ti) ratio; -♦- d_{33} of bulk PZT calculated by Haun *et al.*, ● d_{33} of thin PZT obtained from MOCVD..……………………………………….....63
Figure 3-19. The variation of ferroelectric properties with change of Ti/(Zr+Ti) ratio; -•- P_s of bulk PZT calculated by Haun *et al.*, ■ P_r from MOCVD, P_s from MOCVD, ♦ P_r from PLD, ◊ P_r from PLD, and o P_r from Sputtering……………………………………………………….…...64

Figure 4-1. (a) Evolution of the energy as a function of the soft-mode distortion ξ. (b) Induced dipoles, potentials and depolarizing fields along the [001] direction of the short-circuited ferroelectric capacitor………………....68
Figure 4-2. The lattice parameter constant variation with different composition of zirconium to titanium in PZT. Lattice constants for electrodes (LSCO and SRO) are also indicated……………………………………...…71
Figure 4-3 (a) P-E hysteresis loops and (b) Switching polarization and d_{33} for 20, 40, 70, 100 and 200 nm thick $Pb(Zr_{0.5}Ti_{0.5})O_3$ films on LSCO/STO substrate…………………………………………………….……73
Figure 4-4 (a) ΔP vs film thickness (b) d_{33} vs film thickness from MOCVD-$Pb(Zr_{0.5}Ti_{0.5})O_3$ films, (c) ΔP vs film thickness (d) d_{33} vs film thickness from Sputtering-$Pb(Zr_{0.5}Ti_{0.5})O_3$ films……………………………...75
Figure 4-5. AFM images of the SRO bottom electrode surface……………………..77

Figure 4- 6(a) A typical θ - 2θ x-ray diffraction scan of 130 nm thick PZT/SRO/STO. The in-plane ϕ-scan around the (101) peak shown in the inset. (b) *P-E* hysteresis loops measured at a frequency of 16 kHz. (c) PUND ($\Delta P = P^*$ (switched polarization) - $P^\wedge$ (non-switched polarization)) measurement. (d) Piezoelectric hysteresis loop measured at room temperature………79
Figure 4-7. Ferroelectric hysteresis loops as a function of electric field for 25, 34 and 130 nm thick PZT films measured at 16 kHz……………………….……81
Figure 4-8. Piezoelectric coefficients, d_{33}, loops as a function of electric field for 17, 25, 34 and 130 nm thick PZT films………………………………….....82
Figure 4-9 (a) Ferroelectric hysteresis loop and (b) piezoelectric coefficients, d_{33}, loop for 17 nm thick PZT film……………………………………….……....82
Figure 4-10 (a) low magnification and (b) high resolution cross-section TEM images of 34 nm thick PZT film………………………………………………83
Figure 4-11. Piezoelectric response images for (a) 34 nm (b) 17nm and (c) 8 nm thick films. Piezoelectric response heights of 863.4 mV, 562.5 mV and 357.1 mV were observed, respectively…………………………….………85
Figure 4-12 (a), (b) Cross-section TEM images of 3.6 nm thick PZT film. (c) Piezoelectric response images from 3.6 nm thick PZT films (8-10 unit cells). (d) Piezoelectric response of 5.2 mV was observed with ± 1.5 V and 0.3 V_{pp}……………………………………………..…………86
Figure 4-13. The behavior of ferroelectric order parameters in PZT films with film thickness. Normalized amplitudes from PFM (■), ΔP (Δ) and d_{33} (∇) measurements of $Pb(Zr_{0.2}Ti_{0.8})O_3$/SRO were plotted. The dash-line plot shows the experimental result from PLD-PZT (Nagarajan *et al.*). The dependence of polarization (ΔP) on thickness in $Pb(Zr_{0.5}Ti_{0.5})O_3$/LSCO is also plotted in same scale……………………………………….....88
Figure 4-14. XPS analysis on 4 and 17 nm thick PZT films. Normal (a), (c), (e), (g) and grazing incidence (b), (d), (f), (h) measurements. (a) and (b) : Pb (5d); (c) and (d) : Zr (3d); (e) and (f) : Ti (2p); (g) and (h) : O (1s)…...91
Figure 4-15. XPS spectrum of Zr 3d peak (Zr atoms present in the form of an oxide in PZT and hydroxylated metal species, probably of the form $PbZrO_x(OH)_{3-x}$)…………………………………………………..….92

Figure 5-1. Bi_2O_3 - Fe_2O_3 phase diagram……………………………………………96
Figure 5-2. The thermogravimetric (TG) curves for $Bi(thd)_3$ and $Fe(thd)_3$…………98
Figure 5-3. Relation between Bi and Fe atomic percentage in $BiFeO_3$ films as measured by Rutherford backscattering (RBS) and energy disperse spectrometry (EDS), for precursor mixing ratio prepared at growth temperature of 650 ^oC. Atomic percentage ratio in $Pb(Zr_xTi_{1-x})O_3$ is also plotted at the same scale for comparison………………………………99
Figure 5-4. θ - 2θ X-ray diffraction scans for (I) Fe-rich phase, (II) stoichiometric composition and (III) Bi-rich phase. * : $BiFeO_3$; ● : $SrRuO_3$; ○ : $SrTiO_3$…………………………………………………………………...102
Figure 5-5. Cross-sectional HRTEM image of BFO/SRO interface………………103

Figure 5-6. Surface morphologies (a), (b), (c) and out-of-plane piezoelectric response measurements (d), (e), (f) using a piezoelectric force microscopy (PFM). The thickness of films is ~250 nm……………………………………105
Figure 5-7 (a) Piezoelectric coefficients, d_{33}, loop as a function of applied voltage from 250 nm thick BFO film. (b) *P*-*E* hysteresis loops as a function of applied voltage from 250 nm thick BFO film measured at frequency of 20 kHz. (c) Pulsed polarization (ΔP) as a function of applied voltage at frequency of 20 kHz. (d) Pulse-width dependence of switched polarization (ΔP) in the range from 1μsec. to 1 msec. at 15 V……….107
Figure 5-8. *P*-*E* hysteresis loops obtained from BFO films on SRO / STO and SRO / STO / Si substrates. XRD patterns around (002) BFO peaks are shown in inset…………………………………………………………………...108
Figure 5-9. Comparison of (a) *P*-*E* hysteresis loops and (b) coercive fields dependence obtained from BFO and PZT films on SRO / STO……...110

Chapter 1: Introduction

1.1 Ferroelectric materials

One of the most fascinating aspects of chemistry and physics of oxide materials is a wide variety of the properties they exhibit. Multi-component metal oxides exist in a variety of compositions and crystal structures and their properties vary widely, from insulator to superconductors; and from paraelectric to ferroelectric leading to a vast range of potential applications.

Ferroelectric materials can be classified as non-linear dielectrics that exhibit an electric dipole moment in the absence of an external electric field. The first discovery of ferroelectric phenomenon was found in Rochelle salt [sodium potassium tartrate tetrahydrate ($NaKC_4H_4O_6{\cdot}4H_2O$)] by J. Valasek[1]. Up to date, more than two hundred pure materials and complex crystals are known to possess ferroelectric properties.

A crystal is said to be ferroelectric when it has two or more orientational states in the absence of an electrical field and can be shifted from one to another of these states by an electric field. Polarization is defined as the charge per unit area ($\frac{Q}{A}$) on a plane which is orthogonal to the direction of the polarization vector. The magnitude and orientation of the polarization vector, P, is dependent on the magnitude and orientation of the electric field (E) and crystal structure of the sample.

Accordingly, basic characteristic of all ferroelectric materials is the hysteretic behavior relating polarization (*P*) and applied field (*E*). The energy which is required to change the polarization direction is called "coercive field" (E_c). At zero fields, there are two remanent polarization states ($+P_r$ and $-P_r$) that can be used to store logical states '0' and '1' for memory device applications. The two zero-field values, $\pm P_r$, are equally stable.

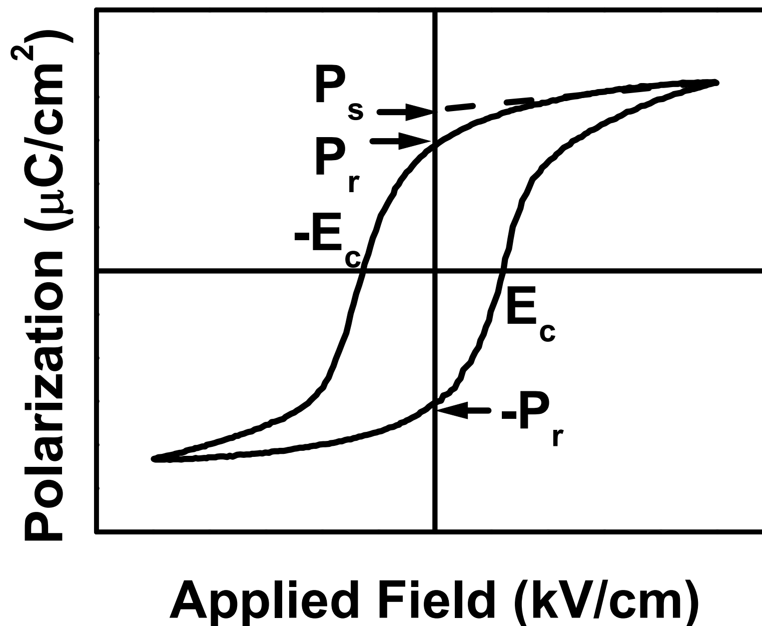

Figure 1-1. Hysteresis loop in ferroelectric materials.

Several key parameters quantify the hysteresis loop. The saturation polarization is the polarization due to maximum domain growth and spontaneous polarization (P_s) is extrapolated from P_{sat} via a tangent. The remanent polarization (P_r) is that remaining upon actual field removal (E = 0). As shown in Figure 1-1,

reduction of E to zero does not return the domain structure to equal volumes of opposing polarization. It is necessary to reverse the field to a level the coercive field (E_c) to achieve this result.

The phenomenon of ferroelectricity and potential device applications recently attracted the great attention for the successful advances in the development of thin-film fabrication of these materials.[2,3,4] This development enables the integration of ferroelectric materials in high quality thin film form directly into device fabrication processes.[5,6]

Thin films of metal oxides are finding a rapidly growing application in advanced materials technology. Ferroelectric thin films have been being developed for a variety of electronic devices. The hysteresis phenomenon in the P–E curve cause ferroelectric materials to be an outstanding candidate for the nonvolatile storage of information in the type of Ferroelectric Random Access Memory (FeRAM).[7,8]

FeRAM is a RAM-based device that uses the ferroelectric effect to store information as an electric polarization in the absence of an applied electric field. No applied field or voltage is required to maintain the memory, which is why the device is termed “nonvolatile”.

The polarization of the entire crystal can be switched from up (+1) to down (0) by reversing the applied field. The memory function is obtained by switching the remanent polarization between two polarization directions by applying appropriate voltages across the capacitor. Among the many desirable attributes for a memory device, the ferroelectric thin film capacitors should show following properties;

•Nonvolatile Memory Characteristics

•Low Writing Voltages (~2V)

•Fast Writing Speeds (<100 ns)

•No Limitation in the Number of Writings

1.2 Pb(Zr,Ti)O$_3$

Lead titanate zirconate, Pb(Zr,Ti)O_3 (PZT), is a solid solution of lead titanate ($PbTiO_3$) and lead zirconate ($PbZrO_3$) and has a perovskite-type structure. Depending on the proportions of $PbZrO_3$ and $PbTiO_3$ and the temperature, PZT composition has a particular crystal structure.

In Figure 1-2, the PZT phase diagram is shown. At high temperature (above the curie temperature), a centro-symmetric cubic paraelectric phase (P_C) is stable. In the $PbTiO_3$ rich phase, a ferroelectric tetragonal phase (F_T) with a spontaneous polarization direction along the [001] direction forms. The tetragonal phase changes to a rhombohedral phase (F_R) at a morphotrophic phase boundary (MPB), which is the zirconate-to-titanate ratio of 52:48 at room temperature, to the $PbZrO_3$ rich phase. In this case (rhombohedral phase), the direction of a spontaneous polarization is along [111].

PZT is well known materials with the perovskite structure which have useful ferroelectric and electro-optic properties. Recent studies showed that PZT materials offer high permittivity for capacitors, large spontaneous polarization for nonvolatile

memory devices, large electromechanical coupling coefficient for surface acoustic wave (SAW) applications, and good optical properties for electro-optic devices.

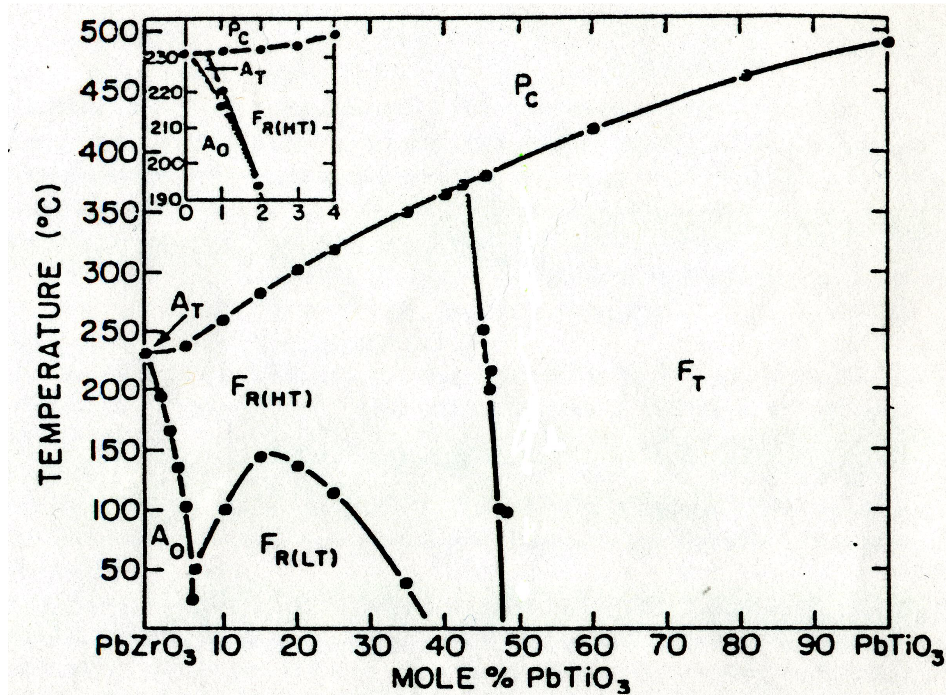

Figure 1-2. The phase diagram of $PbZrO_3$ - $PbTiO_3$ solid solution system.[9]

The principle perovskite structure found in ferroelectric materials is a simple cubic structure containing three different ions of the form ABO_3. The A and B atoms represent +2 and +4 ions, respectively, while the O atom is the oxygen -2 ion. This ABO_3 structure can be thought of as face centered cubic (FCC) lattice with A atoms at the corners and the oxygen atoms on the faces. The B atom is located at the center

of the lattice. This structure can be thought of as each B atom is octahedrally coordinated with six oxygen atoms, with an A atom in the center.

In PZT, Ti^{4+} ions occupy the centers of each cube; Pb^{2+} ions are located at the corners; and O^{2-} ions are centered on each face. The cubic perovskite structure shown in Figure 1-3 is found above the Curie temperature (T_c). Above the Curie temperature these materials have a centrosymmetric structure and this phase is known as paraelectric phase. The Curie temperature of PZT varies in the range of 250 – 480 ^{o}C depending on the composition.

The transition over the Curie temperature affects both structural and physical properties of the material. Upon cooling just below this temperature, PZT undergoes a phase transformation from cubic to a tetragonal modification. In this case, PZT is said to be ferroelectric below Curie temperature. Accordingly, the structure (Tetragonal) of PZT is asymmetrical at room temperature.

As a result, the overall center of positive charge for the distribution of cations within the unit cell is separate from the overall center of negative charge for the anion distribution. This is equivalent to a permanent electrical dipole (spontaneous polarization, P_s) in the tetragonal PZT unit cell. In contrast to a cubic material, the dipole structure of tetragonal unit cell allows for a large polarization of the material in response to an electric field.

The ferroelectric material can have zero polarization under zero applied fields due to a random orientation of microscopic-scale domain regions. Under an applied field, unit cell dipole orientations parallel to the applied field direction are favored.[10]

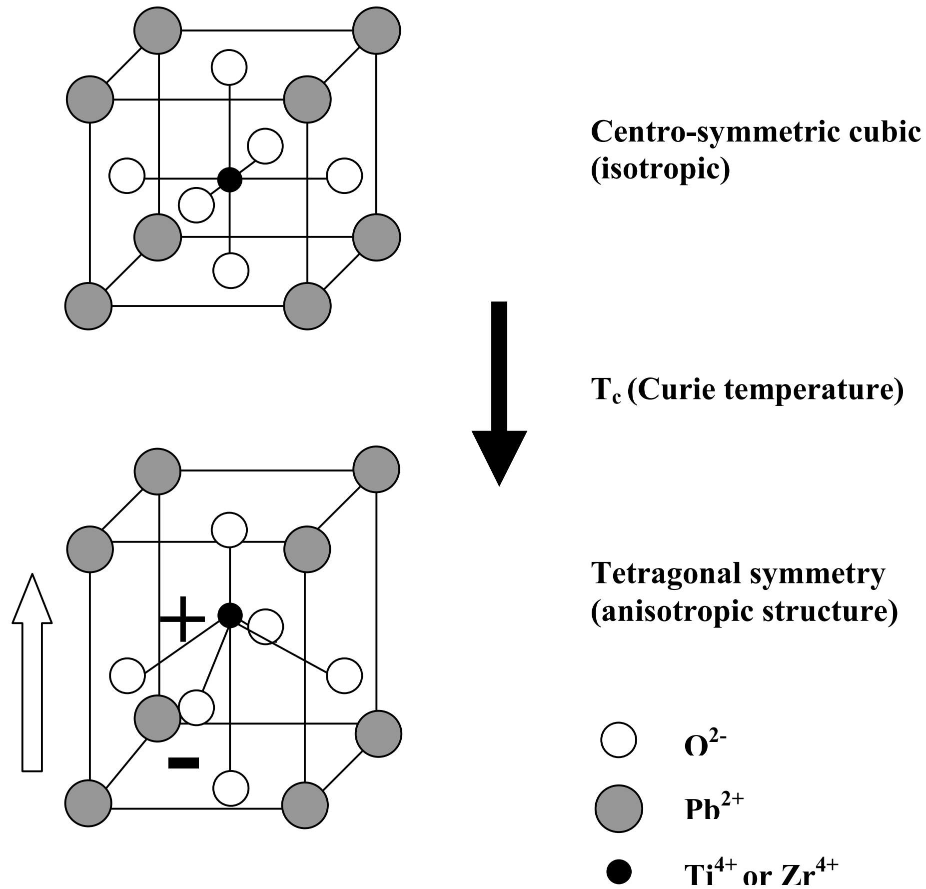

Figure 1-3. The ABO_3 perovskite structure.

Ferroelectric $Pb(Zr_XTi_{1-X})O_3$ film is one of the most promising materials for a FRAM capacitor because of its high phase transformation temperature (T_c), high remanent polarization (P_r) and low working voltage (V_c). Because of these advantages, $Pb(Zr,Ti)O_3$ thin film has been widely investigated for application to FeRAM. Among the many desirable attributes for a memory device, the ferroelectric thin film

capacitors should show large values of switched polarization (ΔP) for short read and write pulses and low coercive voltages. This is motivated by the fact that they will be used in circuits that will typically be integrated using 100 ns wide pulses.

The major properties and device application of PZT can be summarized as;

Piezoelectricity : Sensors and Actuators

Pyroelectricity : IR detector

High Permittivity : Integrated Capacitors

Electro-optic Effect : Optical Wave guides and Light modulators

Ferroelectricity : Non-volatile Memories

Piezoelectricity is the electromechanical coupling phenomena, which is the electrical response to mechanical pressure application. Conversely, electrical signals can make the mechanical deformation. By applying an external voltage the magnitude or the state of the polarization is changed and, consequently, the dimension of the materials can be modified ($\varepsilon = dE$, where ε is strain, d is piezoelectric coefficient, and E is electric field).

The piezoelectric response of ferroelectric PZT films has been extensively studied for years. From this, there is strong interest in introducing ferroelectric PZT materials for microelectromechanical systems (MEMS), because they have large piezoelectric coefficients which may further enhance the performance of sensing and actuation devices.

In bulk ceramics, the piezoelectric and ferroelectric properties vary substantially with the compositional parameter of Zr/Ti ratio.

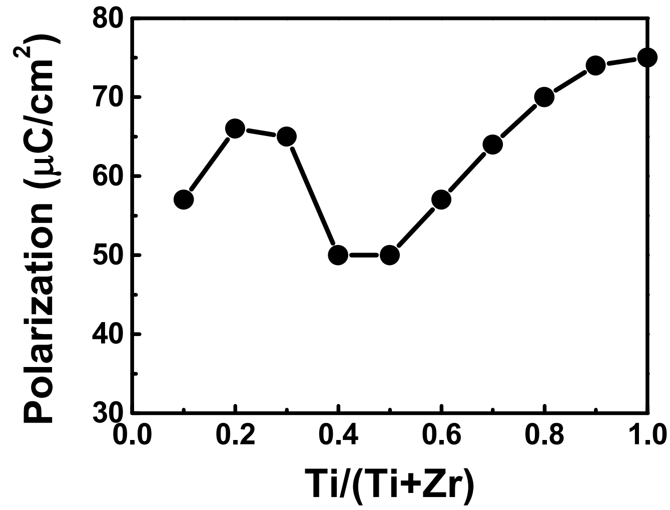

(a)

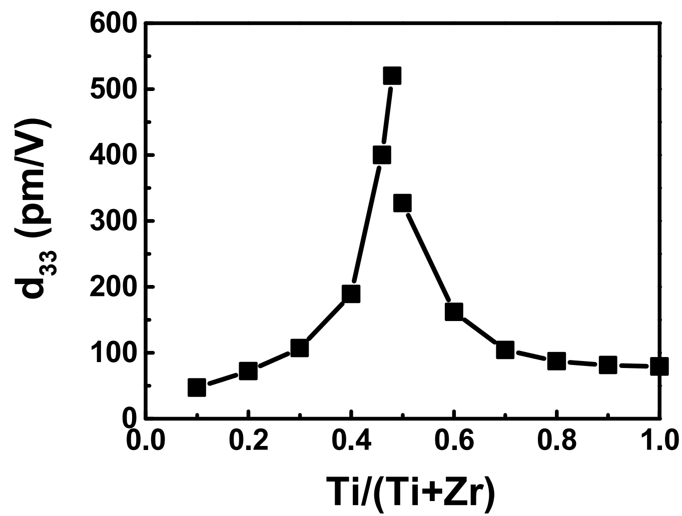

(b)

Figure 1-4. (a) Ferroelectric and (b) Piezoelectric properties of $Pb(Zr_{1-x}Ti_x)O_3$.

In the case of bulk PZT ceramics, the maximum values of piezoelectric coefficients and relative permittivity can be achieved near the morphotropic boundary phase (MBP) composition. The intrinsic ferroelectric and piezoelectric properties with different composition (Zr/(Zr+Ti)) were illustrated (based on the calculations by Haun, 1989, Ferroelectrics)[11].

The effect of Zr/Ti ratios on piezoelectric and ferroelectric has been investigated in thin film PZT. However, the reported piezoelectric coefficients in PZT thin films are scattered, which are believed to arise from both the difficulty in accurate characterization of piezoelectric response in thin films and the sensitive nature of film properties to many parameters other than composition, such as crystallographic orientation, film thickness and microstructure.

1.3 Ferroelectric Random Access Memory (FeRAM)

In the past decade, memory chips with low power consumption and low cost have attracted more and more attention. FRAM offers low-voltage operation and high-speed access as Dynamic Random Access Memory (DRAM) and Static Random Access Memory (SRAM), while containing the nonvolatile data storage and low power consumption of Flash Memory. Figure 1-5 shows the FRAM technology roadmap and the trend of cell circuit architecture and cell capacitor structure. The circuit configuration of memory cells can be either a reliable 2T/2C type (two

transistors and two capacitors) or a 1T/1C type (one transistor and one capacitor) that allows high-density integration.

A FRAM memory cell is fabricated by depositing crystalline ferroelectric film between two electrode plates to form a capacitor. The acute need for compatibility of high-density, high-speed, and low-power memory devices have demanded aggressive scaling of ferroelectric capacitor. The increase in the area of the device can be achieved using the solid stack capacitor structure to compensate the reduced switching charge per cell resulting from the shrinkage of cell size (Figure 1-5).

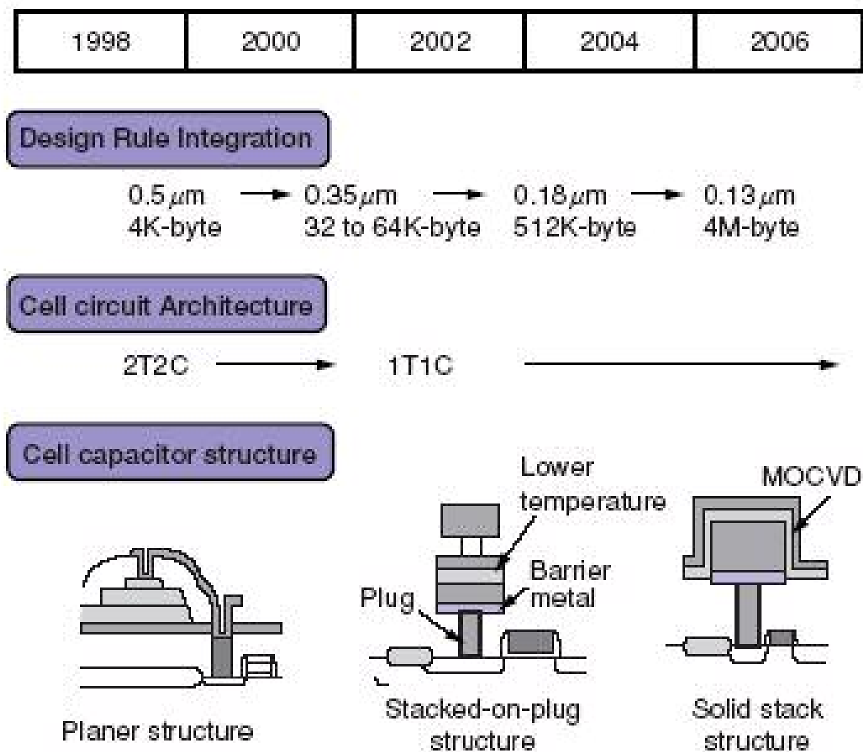

Figure 1-5. Trend of Cell Circuit Architecture and Cell Capacitor Structure (from Fujitsu's FRAM technology solution).[12]

In the fabrication of solid stack capacitor, a key factor is to facilitate the coating of the steps in the ferroelectric film. Therefore, the development of practical preparation process, such as metalorganic chemical vapor deposition (MOCVD), is inevitably required to realize a high-density FeRAM.

1.4 Metal Organic Chemical Vapor Deposition (MOCVD)

The major scientific and technological advances related to the field of ferroelectric thin films made in past decade have been possible because of significant advances in the development and optimization of thin film deposition techniques as well as the development of integration scheme and device design.

A variety of techniques have been used for the deposition of ferroelectric thin films. In general, the thin film deposition techniques can be divided into three major categories;

(1) Physical vapor deposition (PVD): radio-frequency and magnetron sputtering, ion beam sputtering, molecular beam epitaxy (MBE), pulsed laser deposition (PLD)
(2) Solution deposition: sol-gel, metalorganic deposition
(3) Chemical vapor deposition (CVD): metalorganic chemical vapor deposition (MOCVD), atomic layer deposition (ALD)

When ferroelectric capacitors with an effective area larger than the footprint area are desired for high-density integration, three dimensional (3D) capacitor structures should be introduced. Among these deposition techniques, MOCVD offers the greatest potential advantages over other deposition techniques because of its excellent conformal step coverage, controllability of composition, high deposition rate, the possibility of scaling up the process to commercial base production, and compatibility with current Si processes.

In particular, good conformal step coverage is unique in MOCVD so that it enables extension to three-dimensional structures of very small feature sizes with aspect ratios > 1 required for high density FeRAM devices as well as microelectronics.

The technology of MOCVD for oxides has demonstrated explosive advances in the past ten years because of popular interests in ferroelectric as well as oxide superconducting and dielectric materials.[13,14,15,16,17,18,19,20,21]

The step coverage of films grown by MOCVD (MOCVD system in Univ. of Maryland) is shown in figure 1-6.

PZT film was grown on 17 μm wide (2 : 1 aspect ratio) and 5 μm wide (6 : 1 aspect ratio) 3-D trench structures which are processed into silicon substrate. A cross-sectional scanning electron microscopy (SEM) images are shown in figure 1-7.

All surfaces appear to be covered with PZT film and conformality was found to be 85 % and 70 % for 17 μm and 5 μm wide trench, respectively.

The conformality of film on a trench structure is defined as;

$$Conformality = \frac{\min.\,thickness\ of\ \ film}{\max.\,thickness\ of\ \ film}$$

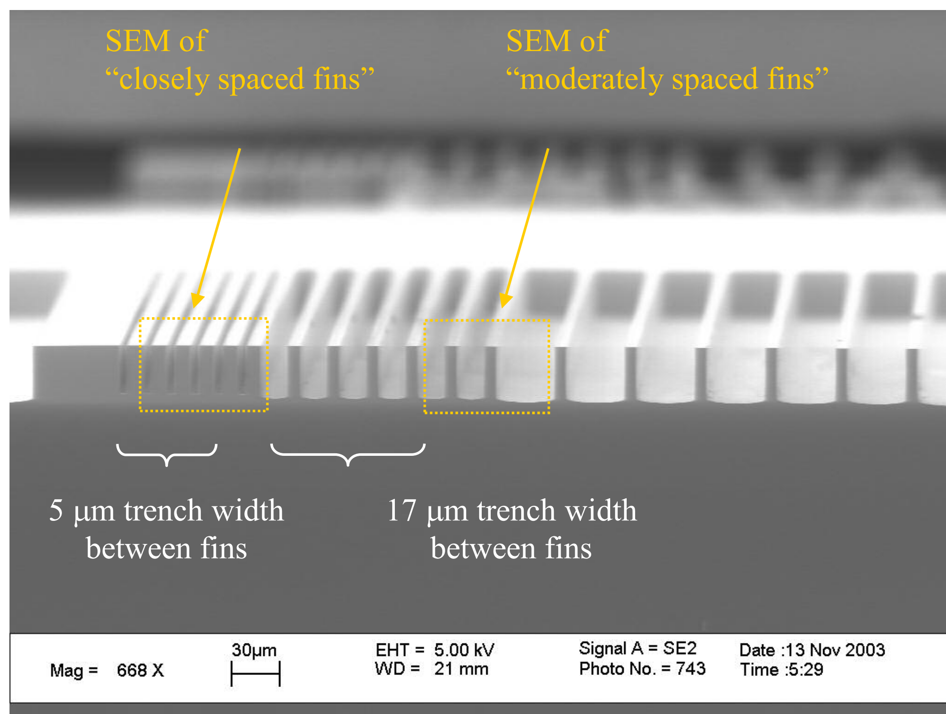

Figure 1-6. SEM images of PZT film deposited on a patterned substrate.

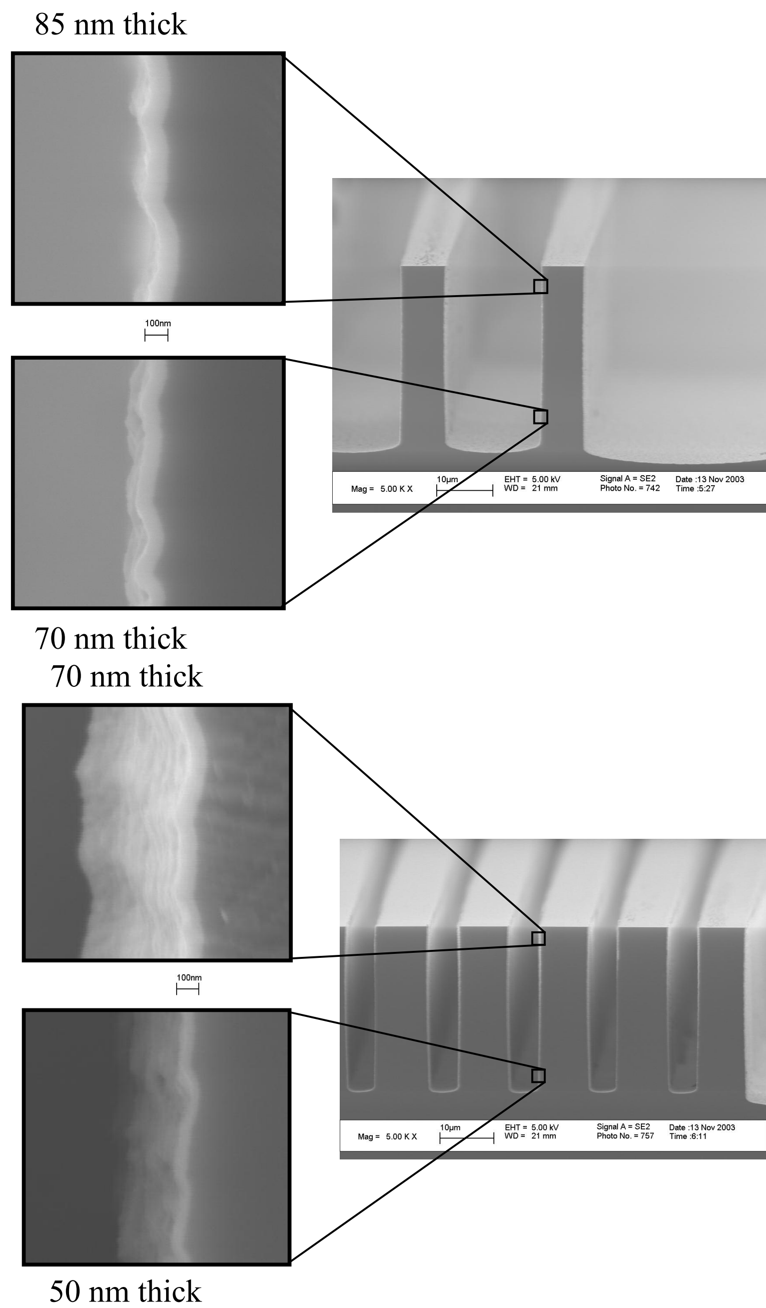

Figure 1-7. Cross-sectional SEM images. PZT films grown on (a) 17 μm wide (2 : 1 aspect ratio) and (b) 5 μm wide (6 : 1 aspect ratio) 3-D trench structures.

The MOCVD technique involves transporting a metal as a volatile metalorganic compound in the vapor phase followed by thermal decomposition usually in the presence of oxygen on an appropriate substrate.

It is important that the precursors are volatile enough to be transported efficiently at source temperatures which are below the precursor decomposition temperature. In other words, there should be an adequate temperature window between vaporization and decomposition. The precursors used need to be compatible and not pre-react. They should decompose to form the desired metal oxide in the same temperature region.

A thorough investigation into the growth mechanism requires dedicated experiments. The basic chemical reaction flow in MOCVD process can be simplified as follows;

1. Generation and transport of precursors in the gas phase.
2. Adsorption to substrate surface of partially decomposed metal organic source.
3. Reaction of the adsorbates to form the intermediate oxide compounds.
4. Intermediate adsorption complexes of the individual oxides are incorporated as a second phase in to the film or they may react with each other to form multi-component metal oxide.

The characteristics of deposited oxide films thus show crucial dependence on the selection of precursor compounds, deposition temperature, deposition environment, and kinetic factors such as the precursor partial pressure and flow rate.

There are two basic regimes in which to deposit films. The deposition regimes are either kinetically limited or mass transport limited. At the low temperature conditions the deposition rate is “kinetics-limited”, i.e. controlled by the rate of reaction of adsorbed species on the substrate surface, and is strongly influenced by temperature. On the other hand, at the higher temperatures the deposition rate is “transport-limited”, i.e. control by the transport rate of precursor to the surface.

In general, there are two methods for obtaining the crystallized ferroelectric phase: the first is direct crystallization from the gas phase (the direct crystallization process) and the second is solid-phase transformation from other solid phases deposited at low temperature, such as the amorphous phase (the solid-phase process). The latter case is mainly used to get high step coverage under reaction rate-limiting conditions (kinetics-limited). However, these low temperature conditions sometimes include imperfect decomposition of the starting source materials. This makes a large amount of the residue produced from the starting materials, such as the element carbon. On the other hand, the former process has been widely investigated in order to obtain epitaxially grown films to study the fundamental properties of ferroelectric thin films.

The first successful deposition of perovskite Pb-based ferroelectric thin films by CVD was reported by Nakagawa *et at.* in "Preparation of $PbTiO_3$ ferroelectric thin film by chemical vapor deposition".[22] They deposited $PbTiO_3$ films by using $TiCl_4$, $PbCl_2$, O_2, and H_2O as source materials. Several problems were pointed from their studies: (1) very high evaporation temperature (700 ^{o}C) was required for $PbCl_2$, (2) poor composition uniformity in $PbTiO_3$ films, and (3) crystallographic imperfections

due to water and/or chloride contamination. Obviously, chlorides are not ideal precursors for the CVD process to prepare metal oxide thin films.

By carefully selecting the organic compounds, the undesirable contaminations in films can be completely excluded. Metalorganic compounds are now used almost exclusively for the deposition of oxide thin films.

MOCVD of PZT films was first adopted in the early 1990s[23] and significant progress has been made to optimize the process control of growth parameters, precursor delivery method, and precursor chemistry.[24,25,26,27,28,29] The success of an MOCVD process depends critically on the availability of volatile and stable precursor materials.

A considerable number of advances have occurred in the area of precursor development as well as delivery techniques.[30,31,32,33]

It is necessarily required that appropriate organometallic precursors be selected in order to obtain desired properties and quality of the thin film. The ideal precursors for MOCVD have to meet the following requirements;

(1) High vapor pressure at low vaporization temperature.
(2) Low decomposition temperature.
(3) Large enough temperature "window" between vaporization and decomposition temperatures.
(4) No contaminations from the organic constituents of the precursors.
(5) Stable under ambient conditions.
(6) Nontoxic.

All of these conditions are seldom met in a single organometallic precursor. Several types of metalorganic compounds have been commonly used as precursors to grow metal oxide thin films including metal alkyls, metal alkoxides, and metal β-diketonates. Most of the metalorganic precursors have reasonable vapor pressures at relative low temperatures. Although metal alkoxides and metal β-diketonates tend to be less volatile than their alkyl equivalents, they are easier to handle and are much less toxic.

The chemical structure of β-diketonates and its complex (tetramethyl heptanedionate (thd)) are shown in Figure 1-8.

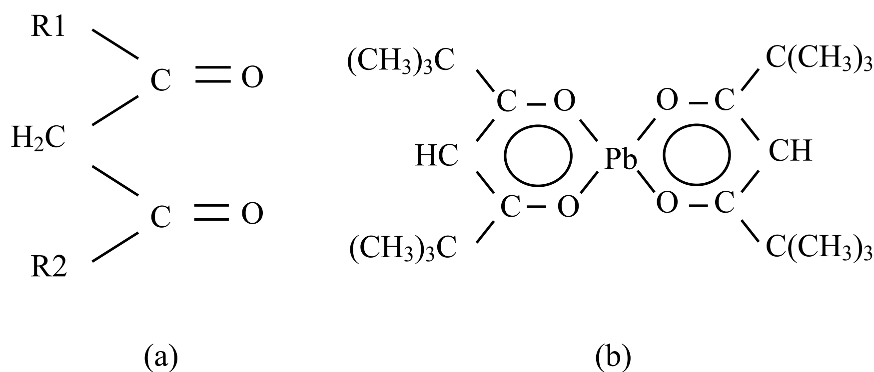

Figure 1-8. Chemical structure of (a) β-diketonates and (b) its complex (tetramethyl-heptanedionate (thd)).

The method of flowing gas through a precursor container under temperature control to carry the bubbled or vaporized material into a reaction chamber is referred

to as a "bubbler" system. A typical schematic design of thermal MOCVD with bubbler system is illustrated in Figure 1-9.

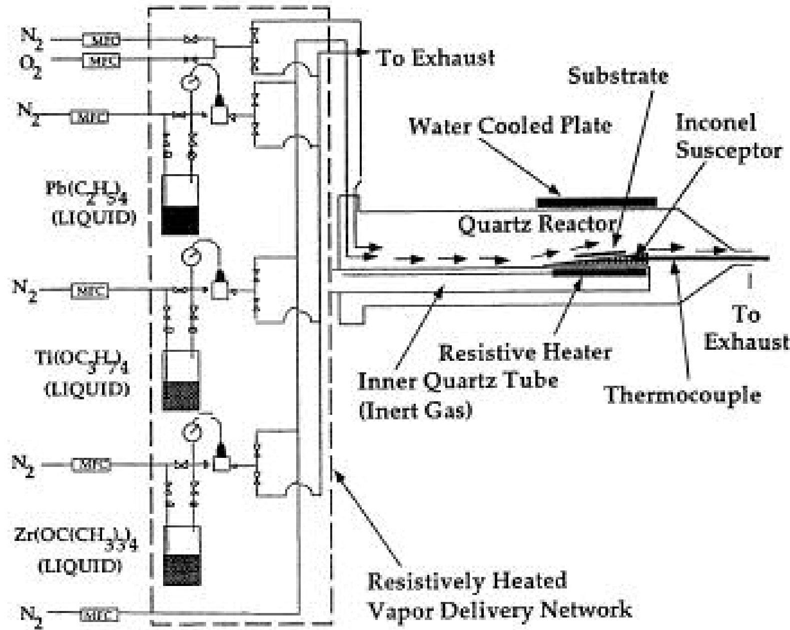

Figure 1-9. Schematic diagram of MOCVD with conventional bubbler system.[34]

Available metal β-diketonate precursors generally have very low vapor pressures, so that high source temperatures are required to obtain adequate mass transport for MOCVD process. In conventional bubbler system, a carrier gas is passed through a precursor held at a high temperature for the duration of the deposition process, this can lead to thermal ageing and decomposition of the precursor prior to transport into a reactor.[35,36]

One of the most promising methods of alternative precursor delivery is liquid delivery system (LDS) MOCVD. In this process, the low-vapor-pressure solid precursors are dissolved in an appropriate organic solvent to form a solid solution. LDS systems are operated by introducing liquid mixtures at high pressure into a hot vaporization cell where the solution is flash evaporated and then transported to the process chamber. In this way the precursor is only subjected to heating in the small "hot cell" during evaporation rather than for the duration of the MOCVD process.

Advantages of LDS can be summarized as;

1. Maintain high accuracy and control flow conditions.
2. Delivery is not affected by source temperature.
3. Flexibility – no pressure drop across the delivery devices.
4. Reduced material decomposition – With LDS, the liquid is not exposed to heat or reactive carrier gases over extended period of time thereby reducing the concern of material decomposition prior to entering process chamber.
5. Minimize need for heated lines.
6. Delivery of low vapor pressure materials at high mass flow rates.
7. Delivery of materials to high-pressure processes.
8. Can take advantage of solution chemistries.

The basic operating sequence of liquid delivery system (LDS) is illustrated in Figure 1-10.

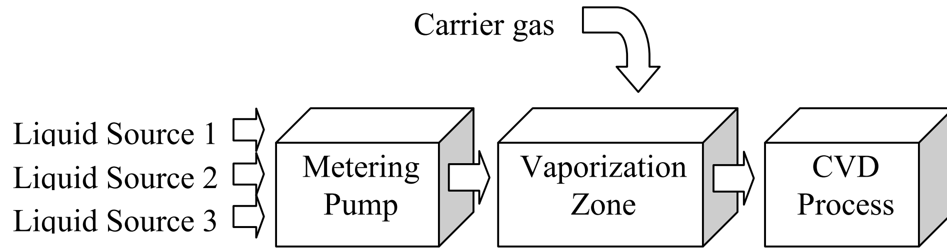

Figure 1-10. Operation sequence in LDS MOCVD.

Contrary to the conventional bubbling MOCVD system, the concept of LDS includes transfer of liquid precursor from the source container at ambient temperature through a pump to a vaporization cell (vaporizer) which is heated to high temperature.

1.5 Theoretical analysis in ferroelectric films

Traditionally, most of phenomenological results from ferroelectric materials have been explained using the theoretical calculations based on the frame of mean-field Landau-Ginzburg thermodynamic theory as described in Eq. (1-1).[37]

$$F(P) = F_0 + \frac{1}{2}\alpha P^2 + \frac{1}{4}\beta P^4 + \frac{1}{6}\delta P^6 + ... \qquad (1\text{-}1)$$

where, α, β and δ are the dielectric stiffness and higher-order stiffness coefficients at constant strain and P is polarization.

with external electric field (E) [Eq. (1-2)],

$$F(P) = F_0 + \frac{1}{2}\alpha P^2 + \frac{1}{4}\beta P^4 + \frac{1}{6}\delta P^6 + ... - EP \tag{1-2}$$

However, these theoretical calculations were established only by considering of a bulk single crystal or freestanding film. Therefore, additional concepts must be considered to describe theoretical analysis on substrate-constrained single domain epitaxial films grown on much thicker substrates. In this case, the clamping effect by the in-plane lattice misfit may affect considerably its phase state and physical properties, and additional strain-term must be included. This concept was well established by Roytburd *et al*.[38] and expressed as Eq. (1-3).

$$F(P) = F_0 + \frac{1}{2}\alpha P^2 + \frac{1}{4}\beta P^4 + \frac{1}{6}\delta P^6 + ... - EP + \frac{\{\varepsilon_M^0 - Q_{12}[P^2 - (P_0^b)^2]\}^2}{S} \tag{1-3}$$

where, $S = S_{11}^P + S_{12}^P$, S_{ij}^P are the biaxial in-plane elastic compliances under constant polarization; P_0^b is the spontaneous polarization of the free standing film or bulk; ε_M^0 is the effective in-plane misfit; and Q_{12} is the in-plane electrostrictive constant.

As the interest of the real device application of ferroelectric thin films has been growing up, the theoretical analysis has been focused on demonstrating the phenomena in a device structure (short-circuit condition) and nano-scale films.

Recently, theoretical investigations using the first principles calculations predicted the ferroelectric ground state and size effects in peroskite-type ferroelectric films. From the first principles calculations, it was found that “depolarizing field” is a key parameter to determine the critical thickness of ferroelectric thin films in device structure.[39,40,41,42]

The size effect in PZT thin films will be discussed in chapter 4 in detail.

Chapter 2: Experimental techniques used in this study

2.1 Precursors for PZT film growth

Of the various metalorganic precursors useful for preparing the PZT thin films, metalorganic Pb precursors and metalorganic Ti precursors are relatively well developed and can be volatilized at relatively low temperatures. By contrast, metalorganic Zr precursors are disadvantageous in that they are very difficult to volatilize.

Although good quality PbO films were obtained from tetraethyl lead (TEL), the extremely toxic nature of this precursor may prevent its use in safety and large-scale applications.[43,44,45,46] Lead alkoxides, for example lead t-butoxide, are liquids at room temperature and possess significant vapor pressures, which also creates toxicity problems. [47] Alternatively, Bis (2,2,6,6-tetramethyl-3,5-heptanedionate) lead ($Pb(thd)_2$) has been widely used as an metalorganic source for the preparation of thin films of Pb-containing ferroelectric materials because of their high chemical and thermal stability.[48,49,50]

$Ti(OiPr)_2(thd)_2$, mixed alkoxide/β-diketonate, is coordinately saturated and therefore less prone to reactive degradation than titanium alkoxides such as $Ti(OiPr)_4$. Moreover, $Ti(OiPr)_2(thd)_2$ is chemically compatible with $Pb(thd)_2$ and preferred when $Pb(thd)_2$ is selected as a lead source.[51,52]

Conventionally, it is tetra (2,2,6,6-tetramethyl-3,5-heptanedione) zirconium ($Zr(thd)_4$) that is the most useful in providing a zirconium source for PZT thin films. $Zr(thd)_4$ exhibits outstanding thermal stability in that it is not decomposed at up to 300 ^oC. In addition, $Zr(thd)_4$ is very resistant to moisture, unlike other Zr precursors. However, this Zr source for PZT thin film growth has a vaporization temperature that is much higher than those of the other sources (Pb and Ti sources). Accordingly, the gap in vaporizing point between the Zr source and the other sources is large. For example, $Zr(thd)_4$ is volatilized at a temperature of about 220 ^oC to 240 ^oC, while $Pb(thd)_2$ and $Ti(O\textit{i}Pr)_2(thd)_2$ have a vaporizing temperature of about 150 ^oC and about 170 ^oC, respectively. Consequently, it is difficult to control the temperature of a vaporizer cell or preheat tube in which volatilized Pb, Ti and Zr precursors are mixed just before entering a reactor. For example, if the preheat temperature is controlled for the Pb or Ti precursor, the gas phase $Zr(thd)_4$ can be easily solidified. On the other hand, if the preheat temperature is raised for the Zr precursor, the Pb and Ti precursors are decomposed or changed before entering the reactor. Consequently, in spite of superior thermal stability and moisture resistance, $Zr(thd)_4$ is disadvantageous because of its low volatility.

Zirconium alkoxides, such as $Zr(O\textit{i}Pr)_4$ and $Zr(OBu^t)_4$ are predicted to be much less thermally stable than $Zr(thd)_4$ but are highly air and moisture sensitive which make them difficult to manufacture in pure form and too unstable for long term storage. Tetrakis(2,6-dimethyl-3,5-heptanedionate) zirconium ($Zr(dmhd)_4$) is a new metalorganic source with chemically stable but has 25 - 30 ^oC lower vaporization

temperature than that of $Zr(thd)_4$, which can makes better thermal compatibility with $Ti(OiPr)_2(thd)_2$ and $Pb(thd)_2$.

In this study, 0.3 mol/L bis(2,2,6,6-tetramethyl-3,5-heptanedionate)lead, $Pb(thd)_2$, in Tetrahydrofuran (THF), 0.3 mol/L di(isopropoxyde)bis(2,2,6,6-tetramethyl-3,5-heptanedionate)titanium, $Ti(O\textit{i}Pr)_2(thd)_2$, in THF, and 0.3 mol/L tetrakis(2,6-dimethyl-3,5-heptanedionate)zirconium, $Zr(dmhd)_4$, in THF (all from Mitsubishi Materials Corporation) were used as metalorganic precursors.

The good thermal compatibility of $Zr(dmhd)_4$ with $Pb(thd)_2$ and $Ti(O\textit{i}Pr)_2(thd)_2$ was confirmed by thermogravimetric (TG) curves as shown in Figure 2-1.

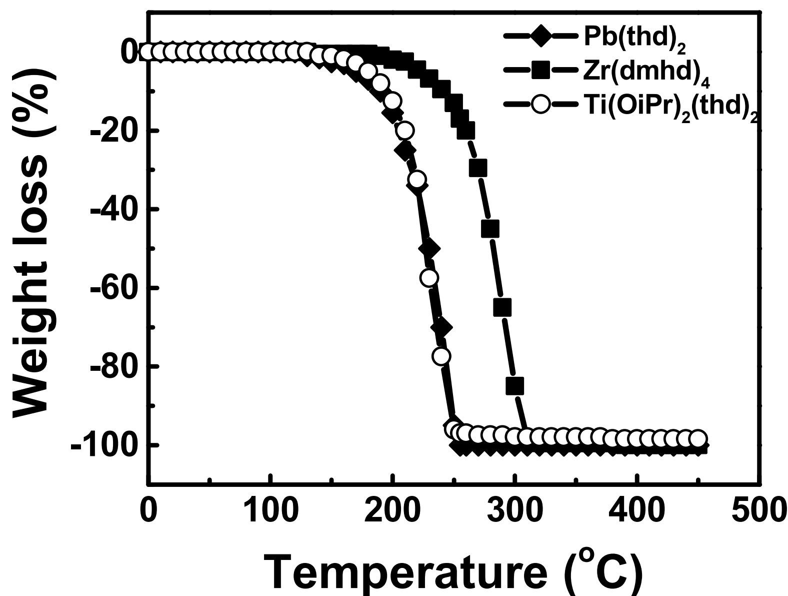

Figure 2-1. The thermogravimetric (TG) curves show the good thermal compatible behavior for $Zr(dmhd)_4$ with $Pb(thd)_2$ and $Ti(O\textit{i}Pr)_2(thd)_2$.

TG results were measured at 1 atm Ar atmosphere by Mitsubishi Materials Corporation. Thermal properties of $Pb(thd)_2$ and $Ti(O\textit{i}Pr)_2(thd)_2$ showed very similar behaviors. Although $Zr(dmhd)_4$ is more compatible with $Pb(thd)_2$ and $Ti(O\textit{i}Pr)_2(thd)_2$ than $Zr(thd)_4$, $Zr(dmhd)_4$ still has about 50 ^{o}C higher thermal decomposition temperature. The promising characteristics from TG analysis is that all the precursors completely decompose without leaving residues which make difficulty in process reproducibility and system maintenance.

2.2 Liquid delivery system (LDS) MOCVD

2.2.1 Lquid delivery system (LDS)

The standard design elements of typical Liquid delivery system are schematically illustrated in Figure 2-2.

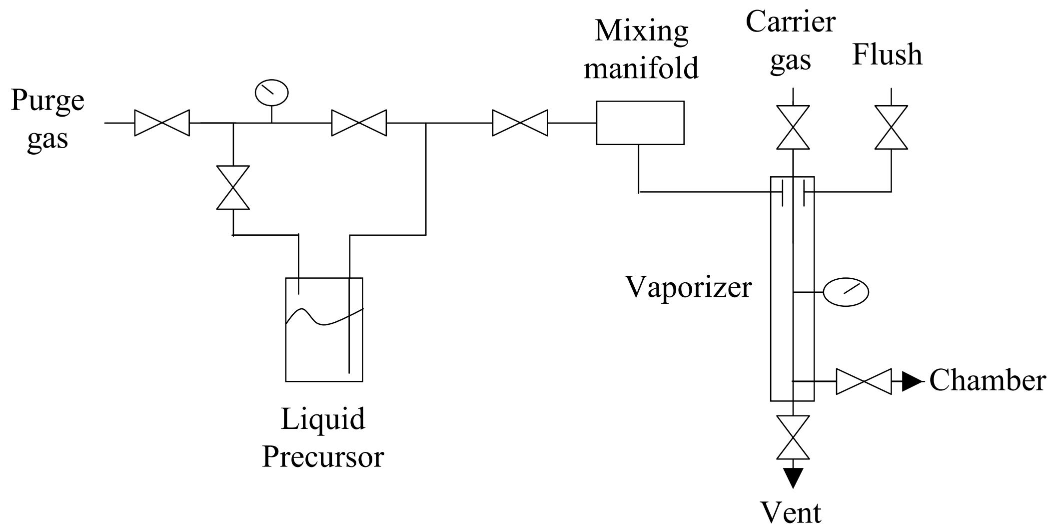

Figure 2-2. Liquid line manifold.

The precursor solutions were delivered using a computer-controlled positive displacement pump with mixing manifold. Three liquid precursors were mixed at specified volumetric ratios in a computer controlled mixing manifold and then transported to the vaporization cell. The mixing of the precursors occurs before the pump and is performed on a time basis, with each channel open for a specified percentage of the total fill stroke of the dual-piston pump. When the low pressure side of the pump is filled, the mixed liquid is transferred to the high pressure side where it is delivered to the vaporizer through a high pressure (≥200 psi) check valve. The vaporization zone was maintained at the appropriate temperature with four-zone heating jackets.

2.2.2 MOCVD system

PZT films were prepared by liquid delivery metalorganic chemical vapor deposition (MOCVD). The schematic diagram of the MOCVD system is shown in Figure 2-3. Vaporized source gas was transported by ultra-high purified Ar carrier gas to a vertical warm-type chamber. During deposition, the vaporizer was switched between the deposition chamber and a bypass to the vacuum system so that the vaporization process stabilized before the introduction of the precursor into the deposition chamber. All the down-stream parts, including the chamber, were heated to a temperature of 5 - 10 ^{o}C higher than the vaporizer temperature to avoid condensation of gas phase source material. The cold traps filled with liquid nitrogen which is connected at the down stream of a reactor, in the meanwhile, remove un-

reacted reagents. The substrate temperature was monitored by a thermocouple which was directly placed inside the center of the substrate holder.

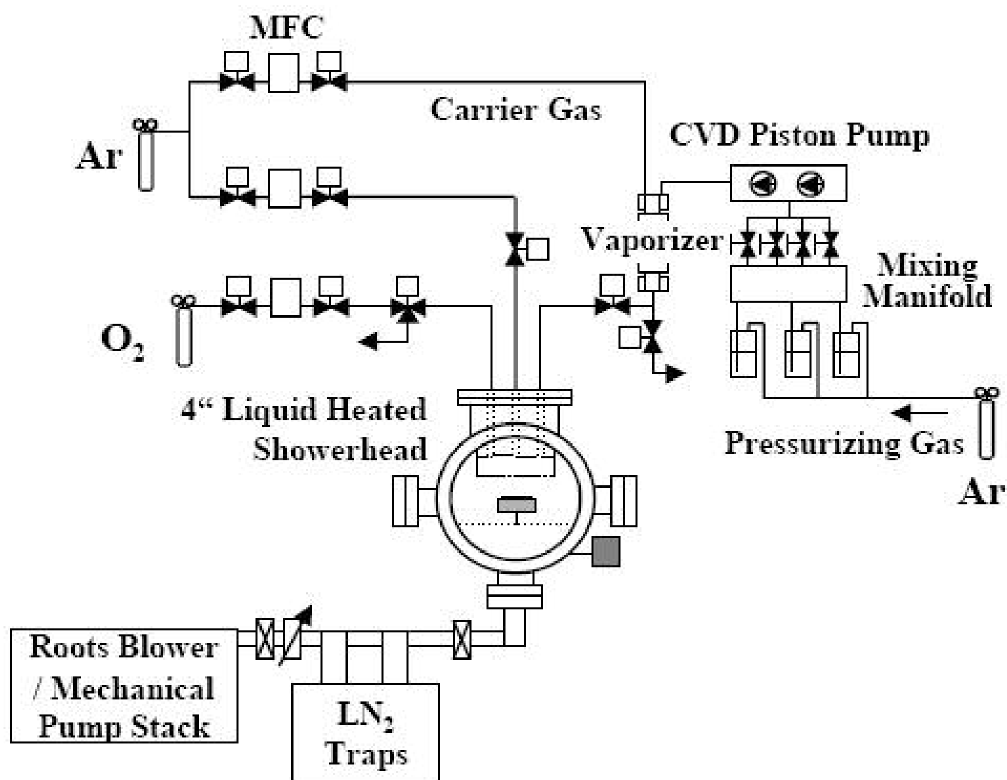

Figure 2-3. The schematic of liquid delivery MOCVD system.

Before loading into chamber, substrates were cleaned in sequence of trichloroethylene (TCE), acetone and isopropanol. The chamber was pumped to a base pressure of 1×10^{-3} Torr prior to ramping the temperature of the substrate heater. The heating and cooling rates were controlled with 20 ^{o}C/min and 5 ^{o}C/min, respectively. At the beginning of the deposition, the source vapors accompanied with Ar carrier gas were flowed through the bypass line; oxygen was flowed through the

deposition chamber to prevent the oxygen vacancy generation in substrate and minimize the back diffusion of source vapors into the chamber. This bypass process was continued for about 3 minutes before beginning the deposition process. After the bypass process, the bypass valve was closed and the main valve of the reaction chamber was opened to start the deposition. At the end of the run the evaporators and all the gases were shut off, and the reactor was evacuated to base pressure before backfilling with air to atmospheric pressure.

High-purity O_2 was used as an oxidizing gas during the deposition that was performed at various substrate temperatures, ranging from 450 ^{o}C to 650 ^{o}C. The deposition rate was in excess of 130 -150 Å/min at 650 ^{o}C.

The detailed deposition parameters are summarized in Table 2-1.

Precursors	$Pb(thd)_2$ $Zr(dmhd)_4$ $Ti(OiPr)_2(thd)_2$
Vaporizer temperature	190 - 210 ^{o}C
Carrier gas flow rate	200 sccm
O_2 gas flow rate	500 sccm
Substrate temperature	450 – 650 ^{o}C
Process pressure	2 Torr
Liquid solution flow rate	0.2 ml/min.

Table 2-1. Deposition parameters of PZT films prepared by liquid delivery MOCVD.

The growth rate of film was feasibly controlled by changing the liquid supply rate. The growth rate change with different liquid source supply rate is shown in Figure 2-4. The growth rate of PZT films linearly increased with the increase of the supply liquid source rate.

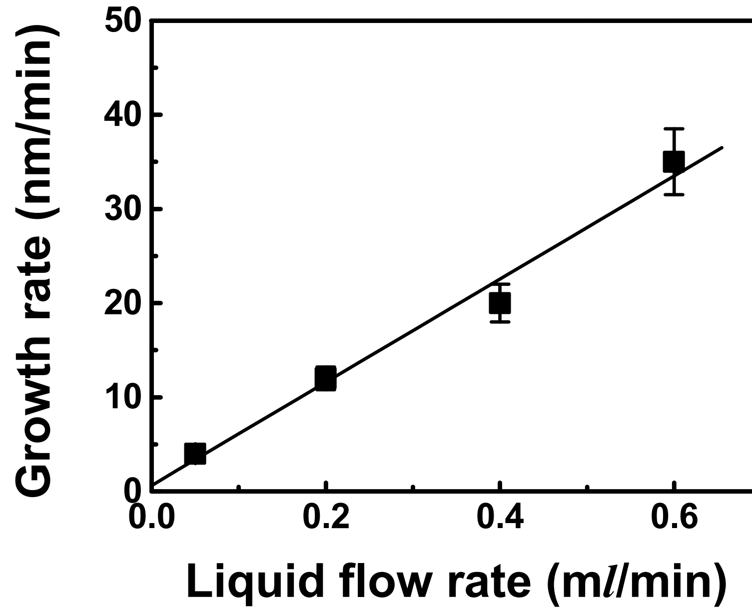

Figure 2-4. The growth rate dependence of the liquid source supply rate.

2.3 Conductive metal oxide thin film growth

Metal platinum (Pt) has generally been used as a substrate in the fabrication of PZT films. However, PZT films deposited on Pt electrode have critical problems such as polarization fatigue with periodic pulses. Although fatigue mechanism has not been clarified, it has been reported that the decrease in polarization values with

periodic pulses is related to domain pinning by the charged defects accumulated at grain boundaries, domain boundaries and PZT/electrode interfaces.[53,54] Oxygen vacancies that are mobile in PZT are the most probable charged defects. It has been suggested that the Pt substrate must be replaced with conducting oxides such as RuO_2, IrO_2, $(La_XSr_{1-X})CoO_3$ and $Sr_{0.5}Ru_{0.5}O_3$ to avoid the fatigue due to oxygen vacancies.[55,56,5758]

Conductive metal oxide layers such as $La_{0.5}Sr_{0.5}CoO_3$ (LSCO) and $Sr_{0.5}Ru_{0.5}O_3$ (SRO) were used as bottom electrode layers.

2.3.1 RF sputtering

For RF sputtering, a high-frequency generator is used generating electromagnetic power in the MHz Region (typically 13.56 MHz). Therefore, the sputtering target is alternatively bombarded by ions and then electrons to avoid charge build-up which limits the use of dc-sputtering for insulating thin film deposition.

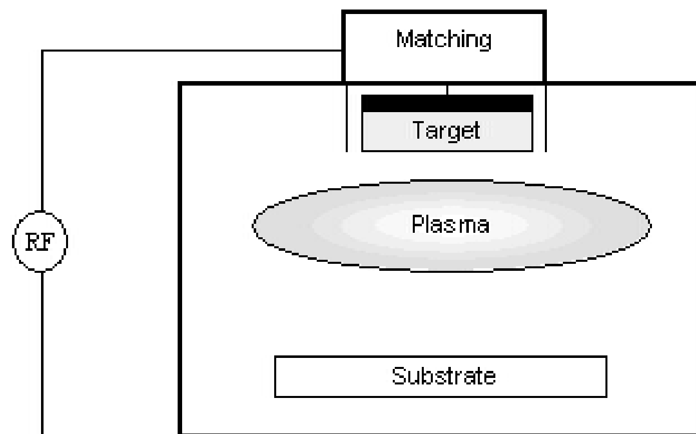

Figure 2-5. RF sputtering configuration.

50 – 60 nm of LSCO or SRO electrode layers were deposited at room temperature on $SrTiO_3$ / Si or $SrTiO_3$ substrates by RF sputtering with a power of 300 W for 30 min. A mixed gas with a ratio of 5 : 1 for Ar : O_2 was used as the reactive and the oxidation source.

The samples were then annealed at 600 – 650 ^{o}C for 1 hour in an oxygen-flowing tube furnace to obtain an epitaxial buffer layer for PZT films. The cooling rate was set to 5 ^{o}C/min after annealing.

2.3.2 Pulsed laser deposition (PLD)

PLD was used to prepare $Sr_{0.5}Ru_{0.5}O_3$ thin films. In the PLD technique, a laser beam (most frequently an excimer laser) is directed at a solid target. The interaction of the pulsed laser beam with the target produces a plume of material that is transported toward a heated substrate placed directly in the line of the plume.

50 - 60 nm thick SRO layers were prepared at 630 ^{o}C by pulsed laser deposition (PLD) where KrF laser with a wavelength of 248 nm was used. The deposition was carried out at 200 mTorr of oxygen for 30min and the samples were cooled down from growth temperature in 1 atmosphere of oxygen to prevent the occurrence of high oxygen vacancy concentration.

The schematic diagram of a PLD chamber is illustrated in Figure 2-6.

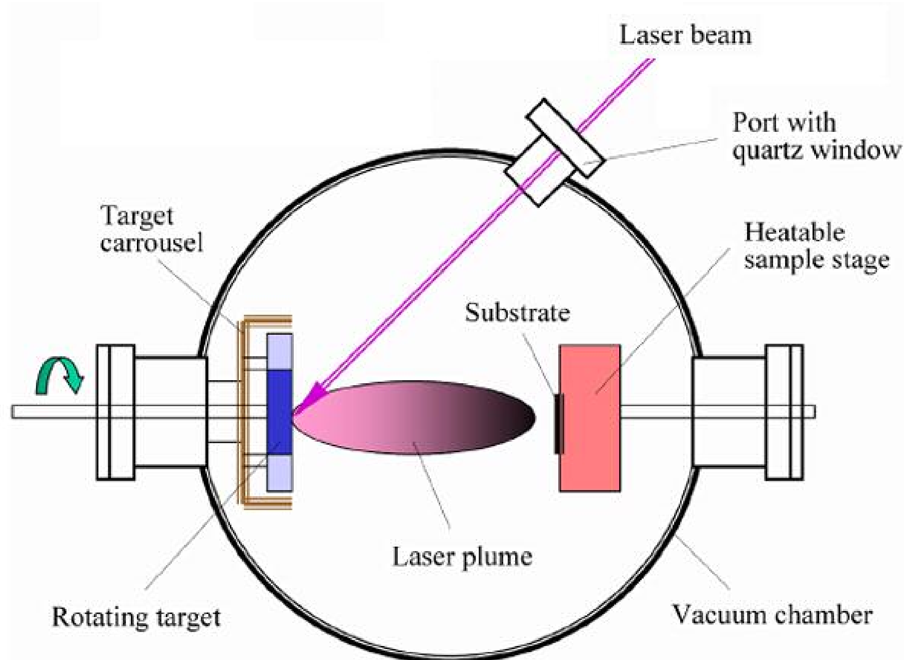

Figure 2-6. Schematic of PLD system [59].

2.4 Device fabrication

To complete the capacitor stack for the electrical and electromechanical measurement, Pt / LSCO or Pt was deposited as top electrodes at room temperature, using RF sputtering and PLD.

A standard positive photoresist (AZ 1512, Clariant Co.) was spin-coated on PZT surface with 4500 rpm for 40 seconds. Baking at 110 ^{o}C for 10 min. was followed to remove stabilizer from photoresist layer and make it to be condensed. The sample was covered by a photo-mask with proper patterning size and then exposed to ultra-violet (UV) light for 1 min. Developing process (AZ 400K developer) performs

photoresist removal by breaking down the structure of the exposed region and shapes circular holes. Care must be taken to avoid overdeveloping or incomplete developing which can be a critical factor to define the precise dimension and good contact between electrode and PZT films.

This was followed by LSCO and Pt deposition at room temperature. The standard lift-off was used to make discrete top electrodes. In lift-off process, samples were dipped in acetone that dissolves underlying photoresist layer. The typical thickness of Pt top electrodes was 60 - 80 nm. The circular electrode diameter was between 18 and 50 μm. This process formed device structure for electrical measurement.

The final sample structure is shown in Figure 2-7.

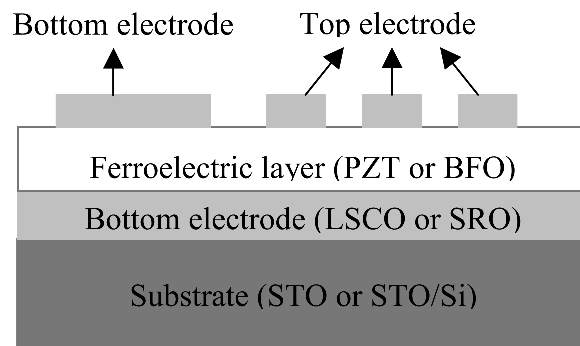

Figure2-7. Sample structure after device fabrication.

2.5 Characterization

2.5.1 X-ray Diffraction (XRD)

X-ray diffraction (XRD) is a powerful method, which is widely used for the characterization of crystalline and structural properties with non-destructivity. When monochromatic X-ray radiation is incident upon the sample, a part of the radiation is scattered from the sample atoms. Scattered X-rays constructively interfere when certain conditions are satisfied. This phenomenon is known as diffraction of X-rays. Two incident rays are scattered from two atomic planes of the crystal. The traveling difference of two rays is equal to the double product of the interatomic plane distance d_{hkl} and the sin function of the incident angle θ. If the traveling difference is equal to an integer number of the incident X-ray wavelength then the constructive interference of the diffracted beam occurs and a sharp diffraction peak can be observed.

This is expressed by Bragg's Law [Eq. (2-1)];

$$n\lambda = 2d \sin \theta \tag{2-1}$$

where n is an integer, λ is the wavelength of X-rays (generally, Cu K_α (1.54056Å)), d is the lattice interatomic spacing and θ is the diffraction angle.

In the case of thin films, lattice mismatch between the grown film and the substrate occurs, which is an important factor in thin film material properties as well

as epitaxial devices. Thus, the complete set of XRD experiments enables to determine and compare the lattice parameters of the substrate and the grown films.

In this study, XRD measurements were carried out by Siemens D5000 four-circle diffractometer with monochromatized Cu K_{α} radiation. A typical θ - 2θ scans, ω - rocking curves and ϕ scans were performed in the XRD studies.

The XRD measurement techniques are schematically illustrated in Figure 2-8.

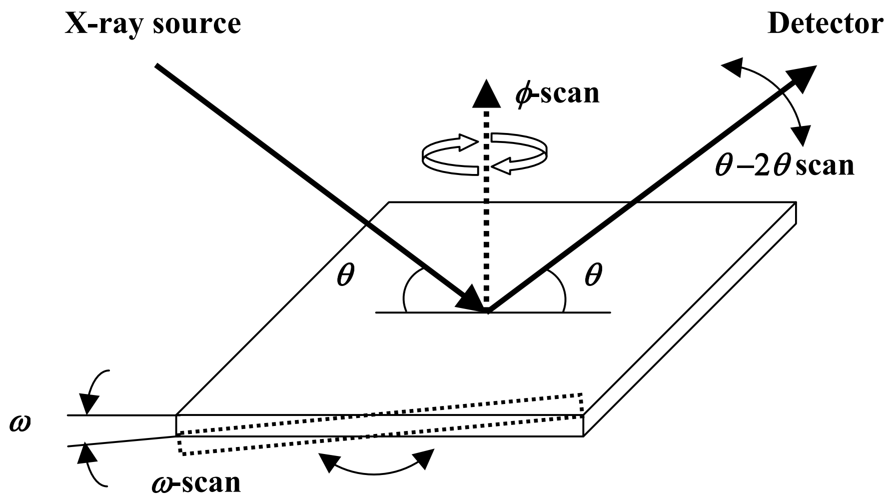

Figure 2-8. XRD measurement techniques.

2.5.2 Rutherford backscattering (RBS)

Rutherford backscattering (RBS) was employed for analyses of the composition and thickness of films with various growth conditions. A 2.00 MeV $4He^{+}$ ion beam was directed at normal incidence to the sample surface and then

detected at a scattering angle of 168°. Channeling measurements were used to evaluate the heteroepitaxial quality of PZT films.

Figure 2-9 shows a typical RBS result of a $Pb(Zr_{0.2}Ti_{0.8})O_3$ film. The calculated minimum-channeling yield obtained from random spectrum and aligned spectrum was 10 - 15 % from PZT films grown on STO substrate, which indicates an excellent crystalline property of PZT films.

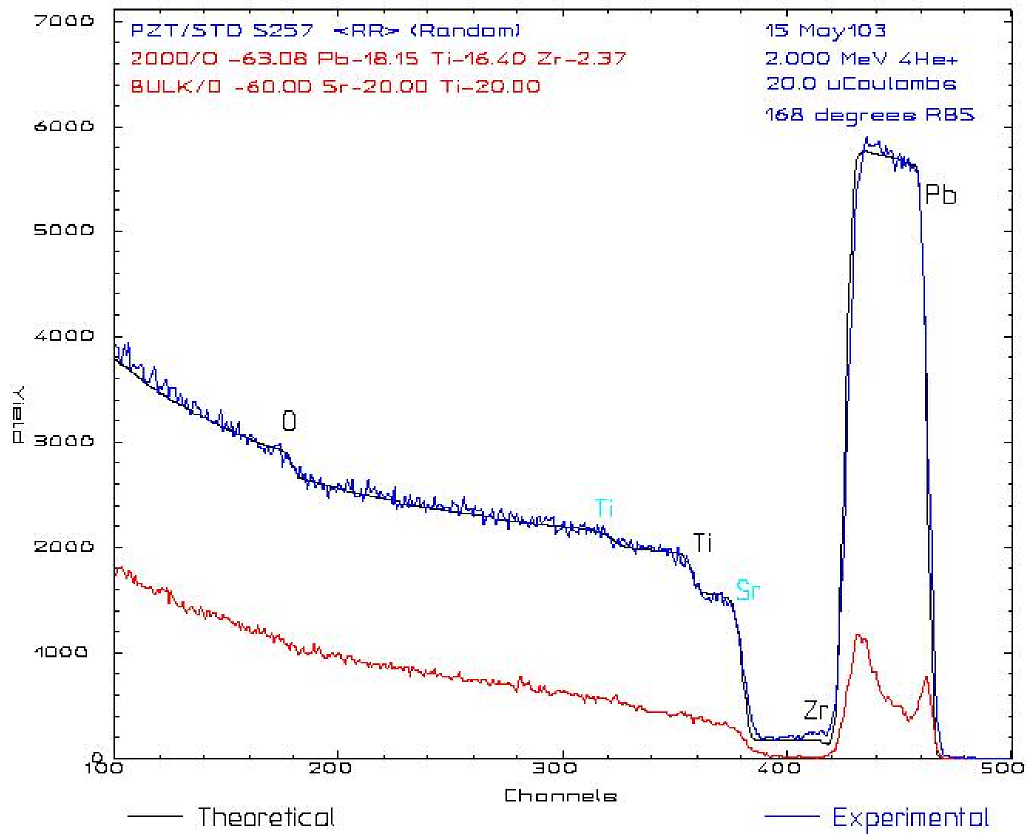

Figure 2-9. RBS result for a sample of PZT film on STO substrate.

2.5.3 Ferroelectric property characterization

The ferroelectric properties were characterized using a Radiant Technologies (RT) 6000 ferroelectric test system which is available for measurements of charge hysteresis, pulse response, bipolar resistivity, pulse polarization cycling vs. fatigue cycling and retention loss vs. time.

Hysteresis polarization measurement

In Figure 2-10, the hysteresis drive profile is illustrated. The hysteresis measurement is performed by applying two single triangle waves which have opposite voltage. A triangle wave with the input positive voltage ($+V_{max}$) is applied first and the negative voltage ($-V_{max}$) is followed. The measure charge values at each step are plotted as polarization ($Q/A = \mu C/cm^2$) vs. voltage.

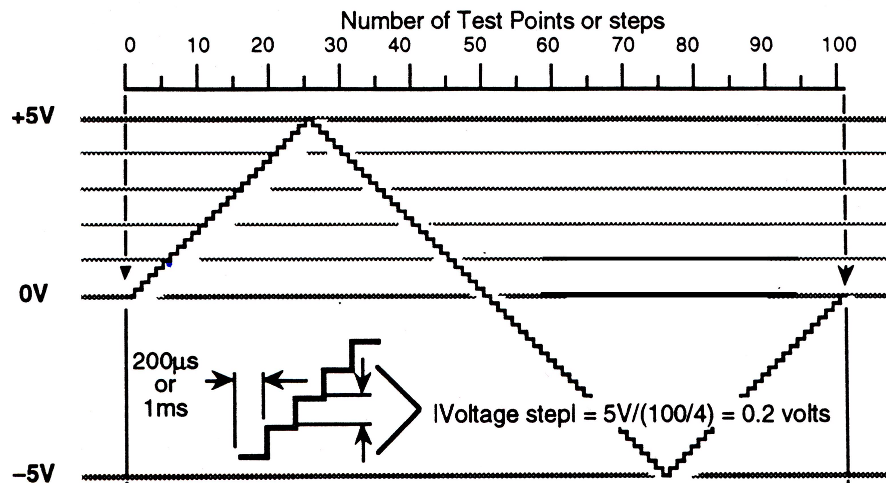

Figure 2-10. Signal drive profile for hysteresis polarization measurement.

Pulse polarization measurement

The pulse sequence to extract the switching polarization, called PUND, is shown in Figure 2-11. Switched and non-switched polarization is measured and polarization induced by domain switching ($\Delta P = P^* - P^\wedge$) can be determined. In ideal case, the polarization measured from hysteresis loop measurement must be equal to the switching polarization obtained from a pulse polarization ($2P_r \approx \Delta P$).

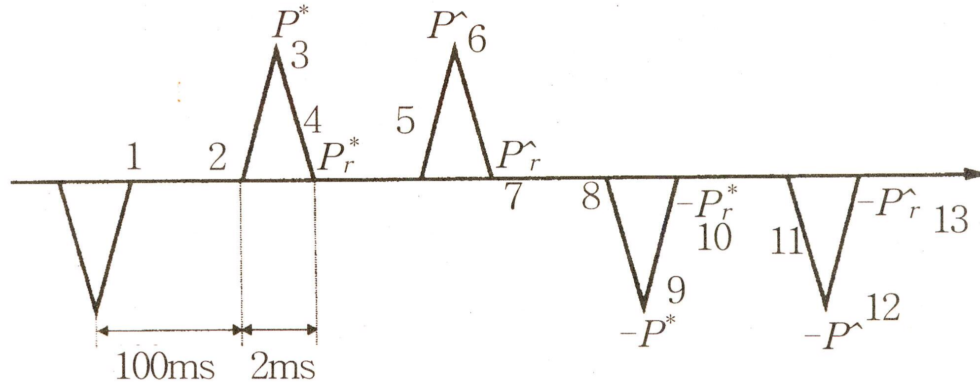

Figure 2-11. Sequence of voltage pulses.

First sample is poled with one direction by negative pulse and the polarization state after poling is marked as 1. This polarization state ($-P_r$) is switched by following two pulses with opposite bias. The switched polarization (P^*) and non-switched polarization ($P^\wedge$) is measured from these two pulses. Consequently, intrinsic switching polarization can be obtained from the relation of $\Delta P = P^* - P^\wedge$.

By doing this measurement, non-ferroelectric switching polarization induced mainly by defects can be distinguished from ferroelectric domain switching. The sequence of pulse and corresponding polarization state are illustrated in Figure 2-12.

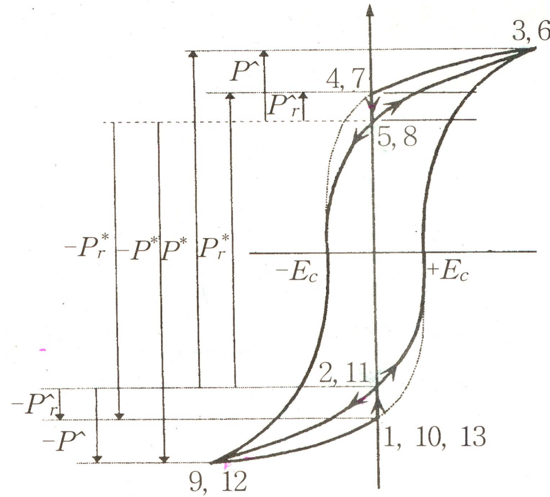

Figure 2-12. Switching (P^*) and non-switching ($P^{\wedge}$) polarization.

2.5.4 Capacitance-Voltage measurement

An HP 4194 gain impedance analyzer (Hewlett-Packard) was used for dielectric property measurement at room temperature.

A small signal with 50 - 100 mV amplitude and various oscillation signal between 100 Hz and 100 kHz in frequency was applied to the test capacitors while a dc-bias was swept with up (negative bias to positive bias) or down (positive bias to negative bias) sweep direction. The small signal capacitance was recorded and the dielectric constant was calculated from the parallel plate equation [Eq. (2-2)];

$$C = \frac{\varepsilon_0 \varepsilon_r A}{t} \tag{2-2}$$

where, C is the capacitance, ε_0 is the permittivity of free space, ε_r is relative dielectric constant of the ferroelectric layer, A is electrode area and t is thickness.

2.5.5 Piezoelectric force microscopy (PFM)

The piezoelectric measurements and the domain structure in thin film, i.e., quantitative piezoelectric coefficient (d_{33}) and piezoresponse domain imaging, were carried out using piezoelectric force microscopy (PFM). A commercial Digital Instruments Nanoscope IIIA Multimode scanning probe microscope, equipped with standard silicon tips coated with Pt/Ir alloy for electrical conduction is used. The schematic experimental setup is shown in Figure 2-13.

PFM measurement is based on the detection of the local electromechanical vibration of the ferroelectric sample induced by an external ac voltage. An external voltage with a frequency ω was applied on the film surface through the tip, which generates a sample surface vibration with the same frequency due to the converse piezoelectric effect. The lock-in amplifier detects the modulated deflection signal from the cantilever which oscillates together with the sample. During measurement, the frequency of the applied voltage was much lower than the cantilever resonant frequency in order to avoid mechanical resonance of the cantilever.

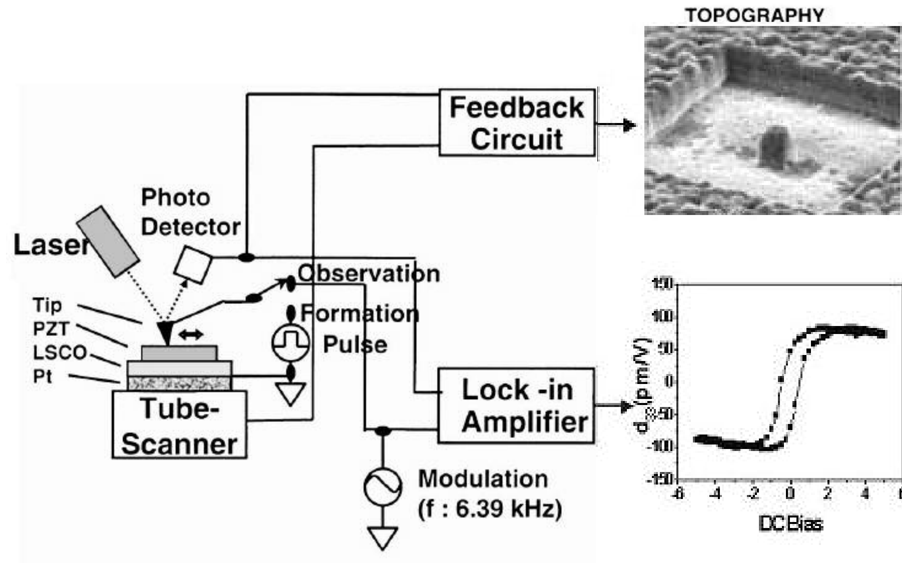

Figure 2-13. Schematic of the experimental setup for piezoelectric measurements.[60]

In piezoelectric imaging, the voltage is applied directly on the surface of sample through the conducting tip, which is used as a movable top electrode. By scanning along the sample surface, the domain configuration of the sample can be mapped out. The typical force constant of these tips was 5 N/m and the apex radius was approximately 20 nm. The contact force was estimated to be around 70 − 100 nN.

In a quantitative d_{33} measurement, the output signal from the photodiode was calibrated using a quartz-coated with top and bottom Au electrodes (2.3 pm/V).

The voltage is applied on the capacitor through the tip to top electrode. This not only makes a homogenous electric field under the electrode, but also prevents the build up of electrostatic interaction between the cantilever and the sample. The measurement frequency of 6.39 kHz was used. Each capacitor was driven at particular dc voltage to study the field dependence.

Chapter 3: $Pb(Zr_{0.5}Ti_{0.5})O_3$ thin film growth on Si

3.1 Background

Lead zirconate titanate (PZT) ferroelectric thin films have been extensively studied as candidates for use in nonvolatile ferroelectric random memories (FeRAMs)[61,62,63], field effect devices[64,65], microelectromechanical systems (MEMS)[66], and pyroelectric sensors[67]. Efforts to integrate ferroelectric thin films with Si-CMOS technology have been greatly increased to enable commercially viable, high-density, nonvolatile ferroelectric memories and other devices. However, the polycrystalline nature of the PZT layer that is typically deposited on platinum-coated silicon wafers can lead to the suppression of ferroelectric and piezoelectric properties of the films. To improve such properties, employing the appropriate substrate must be considered to lower the strain introduced by the mismatch of the substrate and the ferroelectric as well as to control the PZT orientation to the desired direction.

Up to date, there has been significant progress in the growth of epitaxial oxides on semiconductors.[68, 69, 70, 71] Of specific interest is the development of epitaxial $SrTiO_3$ (STO) on silicon for use as an alternative gate dielectric.[72,73,74] By using insulating STO layer as a template/barrier, the epitaxial growth of ferroelectric layers by a sol-gel method has been recently demonstrated.[75]

The orientation of epitaxial STO layer on Si substrate is illustrated in Figure 3-1. The STO layer allows the growth of a highly textured/epitaxial film, ensuring

high polarization as well as uniform properties over large scales and small feature sizes. Such an approach is especially important when the ferroelectric grain size is commensurate with that of the lateral dimensions of the storage cell. This combination of ferroelectric thin film into a bulk semiconductor devices raises practical issues due to the properties of the ferroelectric thin film itself and to process integration.

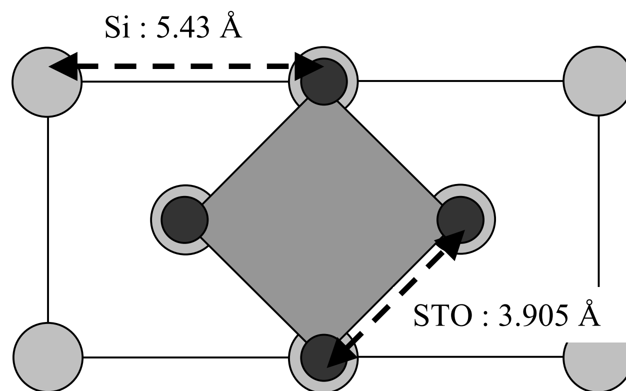

Figure 3-1. Growth of epitaxial STO films on Si substrate

In this chapter the structural and physical properties of $LaSrCoO_3$ / $Pb(Zr_XTi_{1-X})O_3$ / $LaSrCoO_3$ (LSCO/PZT/LSCO) capacitors, which can provide a solution to the polarization fatigue problem, will be presented. In this study the dependence of PZT film composition with the precursor mixing ratio, growth temperature, and switching properties of epitaxial $Pb(Zr_{0.5}Ti_{0.5})O_3$ capacitors are addressed.

3.2 Growth condition control

In order to fully control the MOCVD deposition process, the ratio of Zr/(Zr+Ti) in $Pb(Zr_XTi_{1-X})O_3$ films as a function of the Zr and Ti precursor ratios (V(Zr) / V(Ti)) was mapped out. In this study x ranged from 0.2 to 0.8 at a deposition temperature of 650 °C. The dependence of PZT composition with various temperatures at specific precursor ratios was also investigated. Figure 3–2 shows the relationship of Zr/(Zr+Ti) atomic ratio in the PZT films measured by RBS versus supply precursor source mixing ratios.

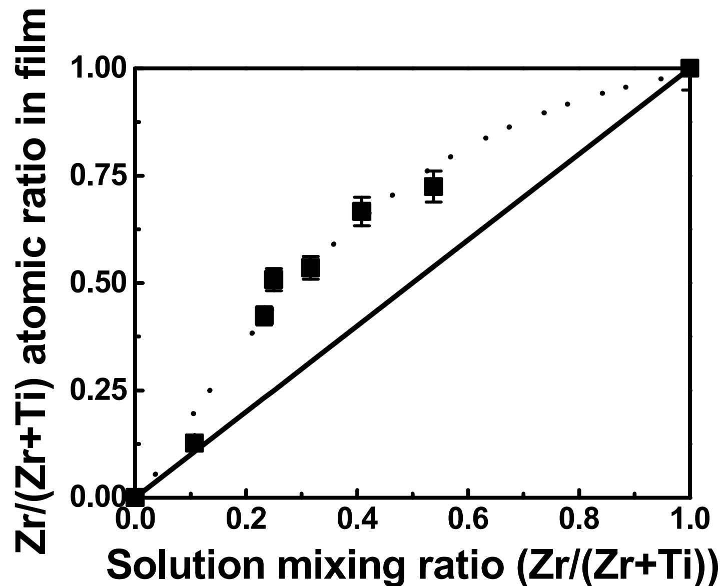

Figure 3-2. The relation of atomic percent of Pb, Zr and Ti of PZT films was measured by RBS with precursor mixing ratio prepared at 650 °C and the same volume ratio (V(Pb) / V(Zr) = 1) of Pb and Zr precursors was used during deposition at 650 °C.

The volumetric ratio of Pb was fixed between 20 - 30 % to get a proper stoichiometric composition of Pb/(Pb+Zr+Ti) (~ 0.5). Even though the entire range of compositions (0<Zr/(Zr+Ti)<1) of PZT films were able to be obtained with proper solution mixing ratios, non-ideal solution behavior was observed. Keijser *et al*. experimentally determined a non-ideality factor for a conventional bubbler system where each precursor was thermally controlled separately.[76] Non-ideality factor (K) can be obtained by the following Eq. (3-1),

$$\frac{x}{1-x} = K\frac{x_g}{1-x_g} \tag{3-1}$$

where, x and x_g denote Zr/(Zr+Ti) ratio in film and gas phase, respectively.

As an approximation, we assume x_g can be directly replaced with x_l (liquid mixing ratio of Zr/(Zr+Ti)). The obtained K value was 2.6, which is higher than the result of 1.49 reported by Keijser *et al*. While conventional bubbler systems deliver each precursor separately, liquid delivery systems have only one hot vaporization cell where mixtures of three different precursors are vaporized simultaneously and then delivered to the chamber together. Since the three precursors have different thermal properties, such as evaporation temperature and thermal volatility, volumetric solution mixing ratio cannot be the same as the supply gas ratio of each component at a fixed temperature which means that x_l is not equivalent to x_g and other calibration factors must be added to Eq. (3-1) to compensate for different thermal volatility. Even though the K's for liquid and gas delivery are not physically equivalent, they are still

useful in describing the relative ease of composition control, independent of delivery method. Despite the relatively high non-ideality factor, it was still possible to reproducibly control film composition.

Figure 3-3 shows the variation of Pb concentration in the film with changing supply mixing ratio at a substrate temperature of 650 ^{o}C. Pb concentration in the film became saturated at a supply mixing ratio of 20 % (Pb/(Pb+Ti+Zr) = 0.5).

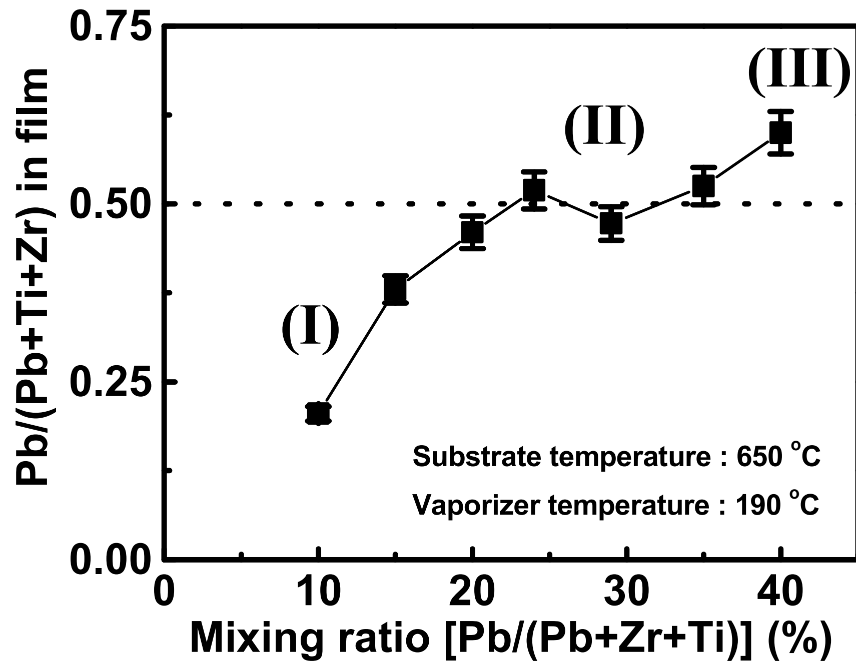

Figure 3-3. The variation of Pb atomic percent grown at 650 ^{o}C with different liquid supply flow rate.

This behavior is consistent with the well-known Pb concentration self-regulation mechanism.[76,77,78] This self-regulation behavior can be explained by the

existence of an equilibrium state between adsorption to substrate surface and desorption to gas phase. The higher vapor pressure of PbO compared with ZrO_2 and TiO_2 allows it to be readily re-evaporated from substrate at high temperature. Competitive reactions between adsorption and re-evaporation on the substrate results in a plateau, which can be used as process window.

The ferroelectric properties of PZT films were significantly influenced by the Pb stoichiometry composition as shown in Figure 3-4.

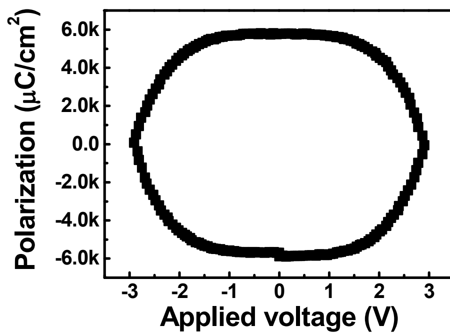

(a) Pb-excess composition

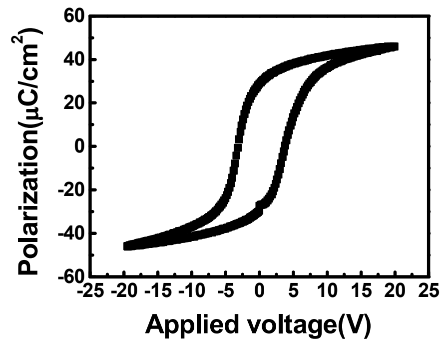

(b) stoichiometric composition

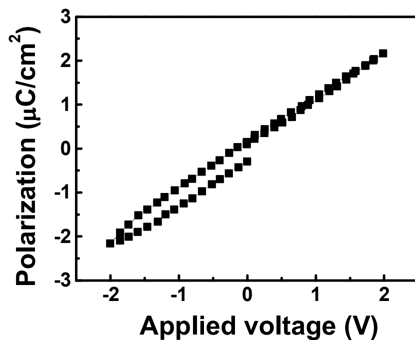

Figure 3-4. The effect of Pb stoichiometry on ferroelectric properties of PZT films.

(c) Pb-deficient composition

No hysteresis behavior or balloon-like opened-hysteresis loops were observed from samples which have more than 10 % Pb excess. Saturated hysteresis loops were obtained from 18.5 % < Pb_{film} < 21 % composition of PZT films which correspond to 7.5 % deficient and 5% excess from stoichiometric Pb composition. On the other hand, dielectric linear response was measured from Pb deficient films.

The variation of composition of each element in film with growth temperature was shown in Figure 3-5. Volumetric mixing ratio of liquid sources was 29 : 29 : 52 of Pb : Zr : Ti and vaporizer temperature was fixed at 190 ^{o}C.

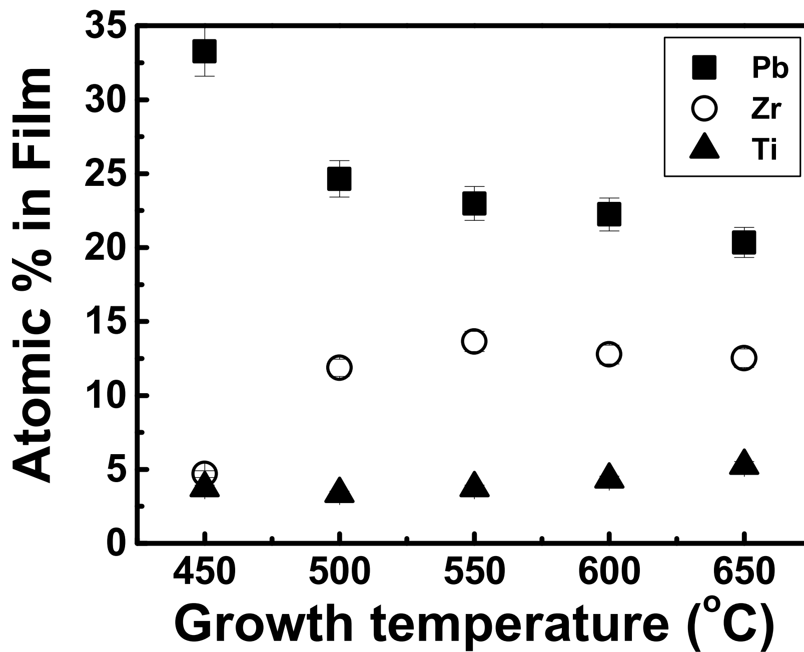

Figure 3-5. Composition dependence on growth temperature.

It was observed that Pb in PZT films decreases with increase of growth temperature because of highly volatile thermal property meanwhile Ti has a slight increase in the PZT films. The content of Zr in PZT films increased below 550 °C and then saturated. From this plot, it was found that the lowest temperature to get stoichiometric composition (0.9 < Pb/(Zr+Ti) < 1.1) is about 550 °C and Pb atomic ratio in films drastically increased at low temperature occurred (lower than 500 °C).

The XRD patterns of PZT films deposited at various temperatures are shown in Figure 3-6. As expected from composition measurement, highly [*00l*] oriented PZT films without any secondary phase were formed above growth temperature of 500 °C. However, only PbO peak was observed from film deposited at 450 °C.

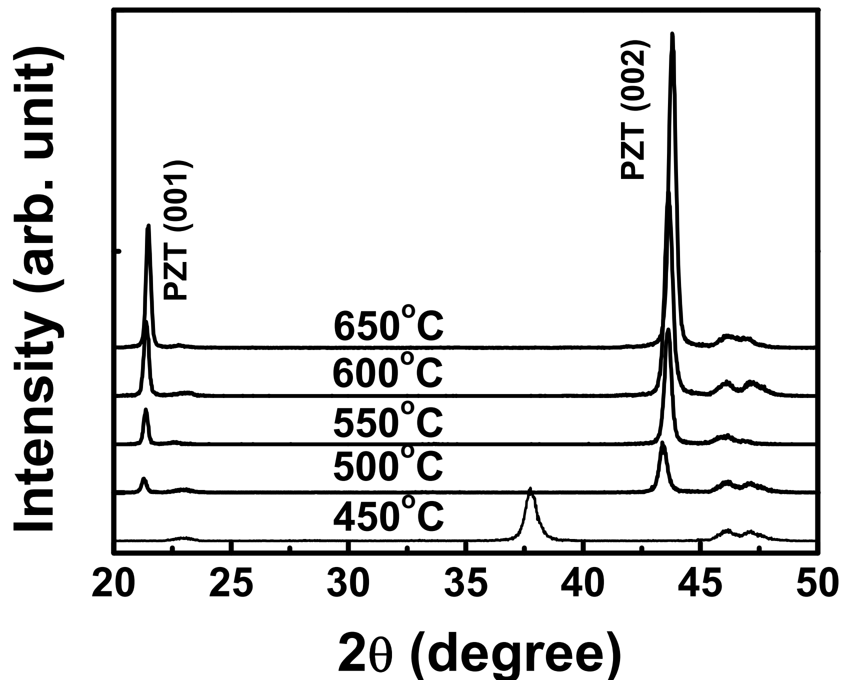

Figure 3-6. θ - 2θ XRD patterns from films deposited at different temperature.

P-E hysteresis loops and switched polarization ($\Delta P = P^* - P_r$ ($\sim 2P_r$)) were measured from these films. The higher polarization values were obtained from films grown at high temperature as shown in Figure 3-7, which results from the better crystallinity with high process temperature within stoichiometric composition.

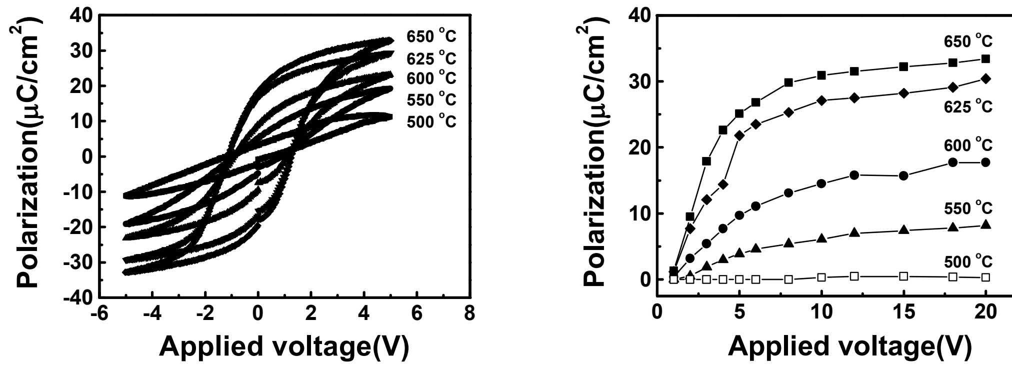

Figure 3-7. (a) *P-E* hysteresis loops and (b) Switched polarization ($\Delta P = P^* - P_r$ ($\sim 2P_r$)) from films deposited at different temperature.

Pure oxygen was used an as oxidation source for the PZT thin film growth. The deposition of metal oxides can theoretically be achieved without an added oxidant source because a metal-oxygen bond is already present in metal β-diketonate complex. On the other hand, metalorganic precursors contain carbon element already, which can be the critical factor of the leakage problem when it is incorporated into the films. Therefore it is necessary to add oxygen gas to fully convert the hydro-carbon in β-diketonates complex to CO_2 and H_2O. The dependence of the oxygen flow rate on the PZT film growth is shown in Figure 3-8.

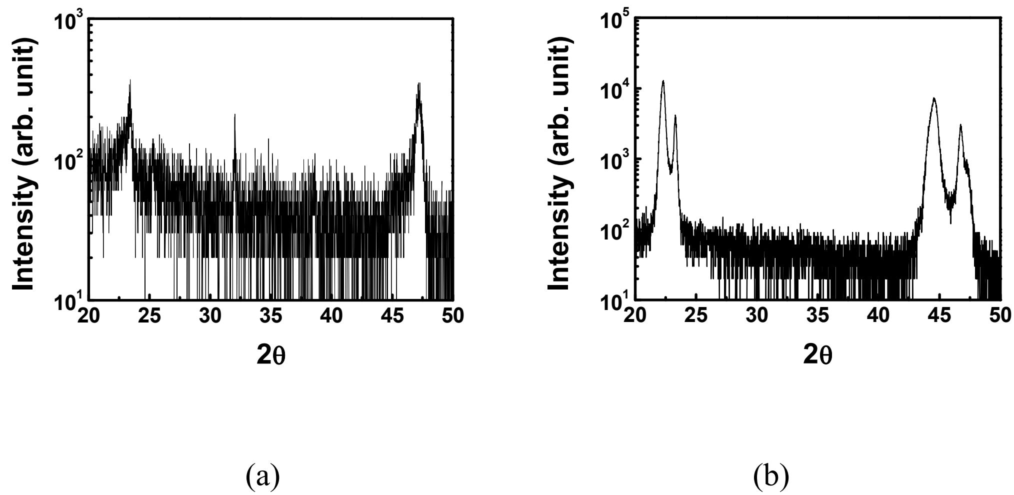

(a) (b)

Figure 3-8. The dependence of oxygen flow rate on the film growth (a) O_2 : 0 sccm and (b) O_2 : 300 sccm.

Perovskite PZT phase was not formed without oxygen supply while the epitaxial films were obtained with minimum oxygen flow rate of 300 sccm. Oxygen flow rate of 500 sccm which is the pressure of 0.9 torr in chamber was used as a growth condition.

3.3 Structural and electrical properties of $Pb(Zr_{0.5}Ti_{0.5})O_3$ films

$Pb(Zr_{0.5}Ti_{0.5})O_3$ films were obtained with the solution mixing ratio of 20 : 20 : 60 from Pb : Zr : Ti. This composition is close to the morphotropic phase boundary (MPB). This composition possesses a lower coercive field, and large d_{33}, which is strong candidate for nonvolatile memory and new microelectromechanical systems (MEMS).

A typical θ - 2θ x-ray diffraction scan of LSCO/PZT/LSCO is shown in Figure 3-9, indicating that the LSCO/PZT/LSCO heterostructure is highly [*00l*] oriented without any secondary phase. The in-plane ϕ-scan around the (101) peak shown in the inset in Fig. 3-9 further confirms that the films grow with the expected four-fold symmetry. A *c*-axis lattice parameter of 4.08 Å was calculated from the diffraction patterns.

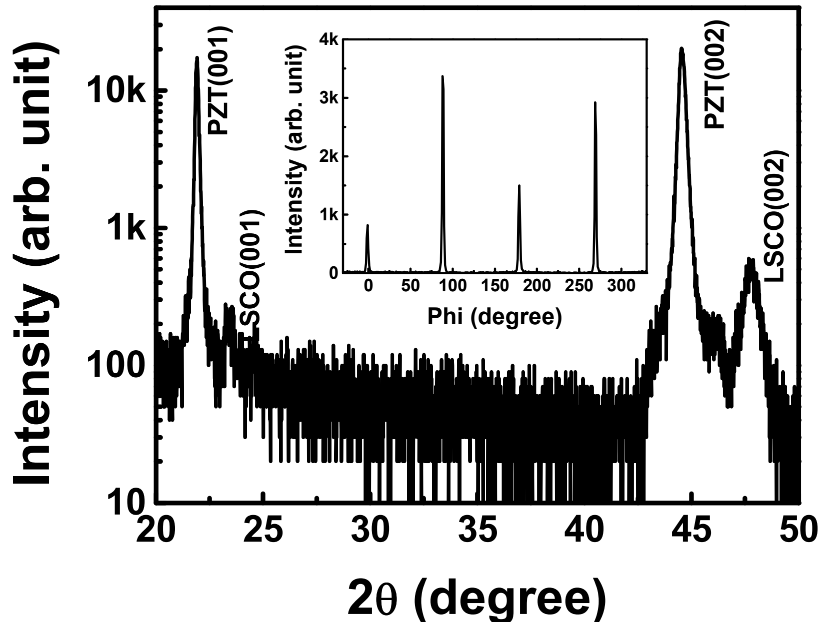

Figure 3-9. A typical θ-2θ x-ray diffraction scan and ϕ-scan of LSCO/ PZT/LSCO capacitors deposited on STO/Si at 650 °C.

The capacitors were subjected to a variety of stringent electrical tests to probe their performance characteristics. The hysteresis loops of 230 nm thick PZT films measured at 1 V, 3 V, and 5 V are shown in Figure 3-10. The measured resistivity

was found to be in the order of $4 - 8 \times 10^{10}$ Ω-cm. The remanent polarization (P_r) and coercive field (E_c) measured at 3 V were about 25 μC/cm² and 27.5 kV/cm, and about 31 μC/cm² and 30 kV/cm at 5 V, respectively. This high polarization and low coercive field are very favorable for FeRAM application.

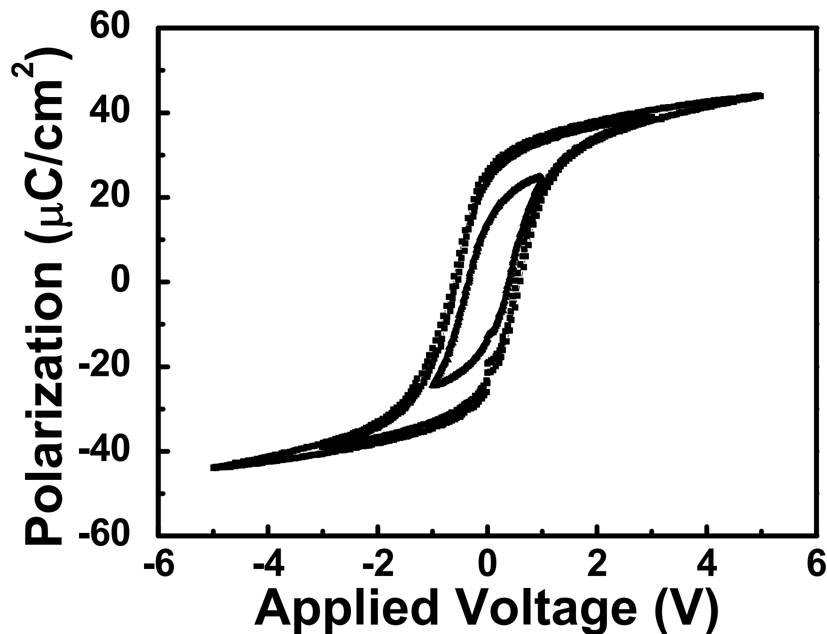

Figure 3-10. The hysteresis response of 230 nm thick $Pb(Zr_{0.5}Ti_{0.5})$ capacitor sandwiched by LSCO electrodes at 1 V, 3 V and 5 V.

Capacitance curves measured on this film are shown in Figure 3-11. The measurements were made for disk shape capacitors with an area of 2.2×10^{-5} cm². A capacitance of 158 pF at 6390 Hz, and the dielectric constant (ε_r) calculated from this value is 1600 at peak points were measured. (ε_r was calculated from equation of

$\varepsilon_r = \frac{t \times C}{\varepsilon_0 \times A}$, where t is thickness, C is capacitance, ε_0 is permittivity of free space and A is electrode area). This value is close to the results obtained for films of similar compositions and thicknesses grown by CVD.[79]

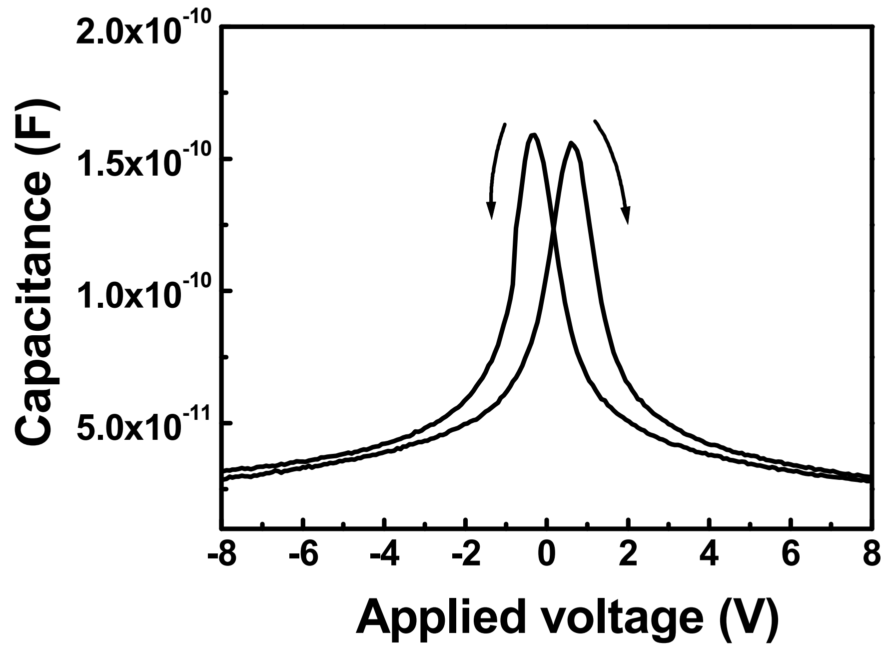

Figure 3-11. Capacitance vs applied voltage measured with 230 nm thick $Pb(Zr_{0.5}Ti_{0.5})$ capacitor sandwiched by LSCO electrodes.

In order to further characterize the capacitors, the pulsed polarization ($\Delta P = P^* - P^\wedge$) as a function of applied voltage is displayed in Figure 3-12.

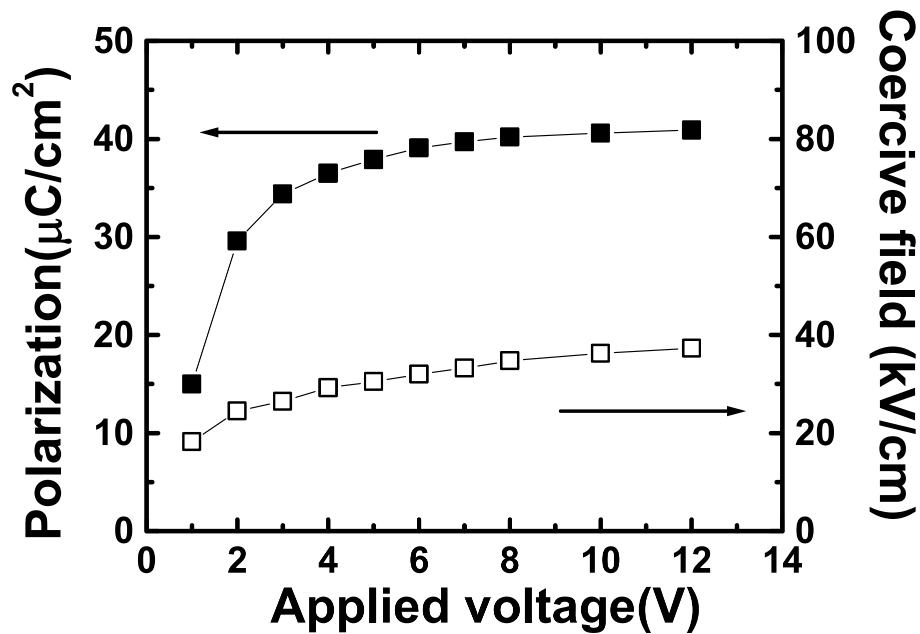

Figure 3-12. Polarization (switched (P^*) – non-switched ($P^\wedge$)) and coercive voltage of LSCO/PZT/LSCO capacitors as a function of applied voltage.

It indicates a pulsed polarization value of 34 μC/cm^2 and 36 μC/cm^2 corresponding to 3 V and 5 V, respectively. In addition, the coercive field versus the applied voltage is shown in the same figure. This figure shows that it saturates with increasing the applied voltage; the coercive field is only 37.3 kV/cm (0.75 V) at 12 V, which is consistent with the properties of PZT near MPB [80] and ideal for low voltage application.

Figure 3-13 shows the dependence of pulsed polarization (ΔP) on pulse-width. A key point of reference is the value of this pulse polarization at a pulse width of 1 μsec. The LSCO / PZT / LSCO capacitors show favorable pulse width dependence,

i.e. the polarization measured at 5 V is 33 μC/cm^2 at 1 μsec pulse width and increases to about 40 μC/cm^2 at 1000 μsec. It is still 23 μC/cm^2 at 3 V for a pulse width of 1 μsec. Quantitative fits of the pulse width dependence for the samples yield a slope that is essentially constant (2.5 - 3 μC/cm^2 per decade) although the slope measured at 5 V is slightly smaller. The weak pulse-width dependence of polarization for the samples prepared by MOCVD demonstrates that these capacitors are promising candidates for high-speed FeRAM application.

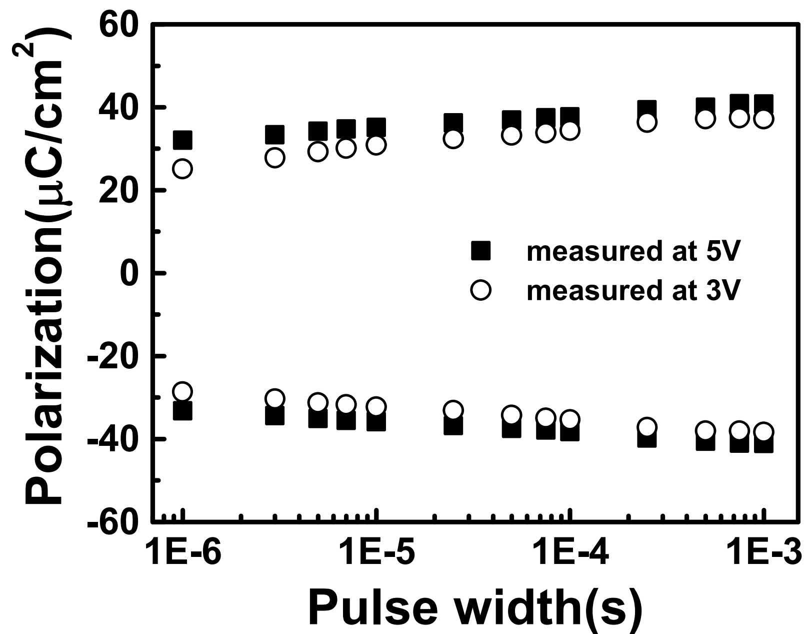

Figure 3-13. Pulse-width dependence of polarization (switched (*P**) – non-switched (*P^*)) of LSCO/PZT/LSCO capacitors measured at 3V and 5 V, respectively.

A key issue in ferroelectric materials is the degradation of properties as a result of a large number of switching cycles and this effect is known as fatigue. A

critical drawback in early ferroelectric memories was the fact that the total switched charge decreased with use. Typically switched charge degraded to ~50 % of its initial value after 10^6 writing/read cycles. This is crucial problem for ferroelectric memories and fatigue in ferroelectric devices has been studied for many years. It has been clearly demonstrated that the use of a conducting perovskite electrode (such as LSCO) can eliminate polarization fatigue.[81] Figure 3-14 shows the test capacitors subjected to polarization fatigue testing via bipolar-pulsed cycles of both 3 V and 5 V at 1 MHz. Fatigue characteristics of LSCO/PZT/LSCO capacitors measured at different voltages shows no observable degradation up to 10^{11} cycles.

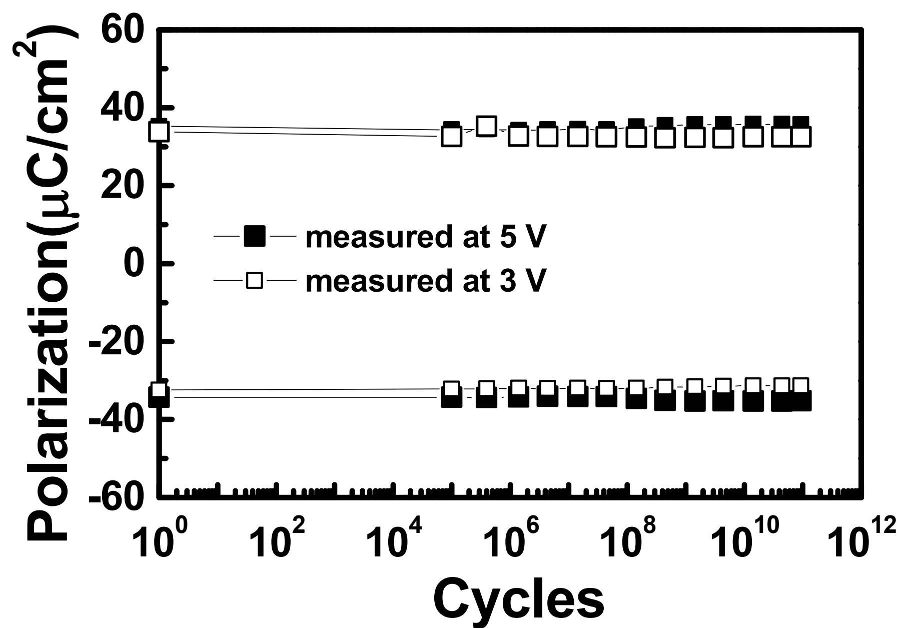

Figure 3-14. Fatigue resistant characteristics of LSCO/PZT/LSCO capacitors as a function of bipolar-pulsed cycles measured at 3 V and 5 V, respectively.

In order to confirm that the capacitors still retain a logic state (either ”1” or “0”) after cycling, capacitors were subjected to the retention test. During a retention test the decay in stored charge (polarization) of a capacitor which has already been stored as a “1” or “0” logic state is measured as a function of time. The retention tests were performed by applying a write pulse of 3 V and 5 V to a test capacitor, after a specific period of time, and then applying two read pulses using the same voltage as write voltage to measure the polarization. The difference of switched polarization (P^*) and nonswitched polarization ($P^\wedge$) is used to characterize the ability of retention to distinguish the two logic states. Figure 3-15 shows desirable retention characteristics measured at 3V and 5 V. The polarization of test capacitors did not decrease apparently up to 10^5 sec.

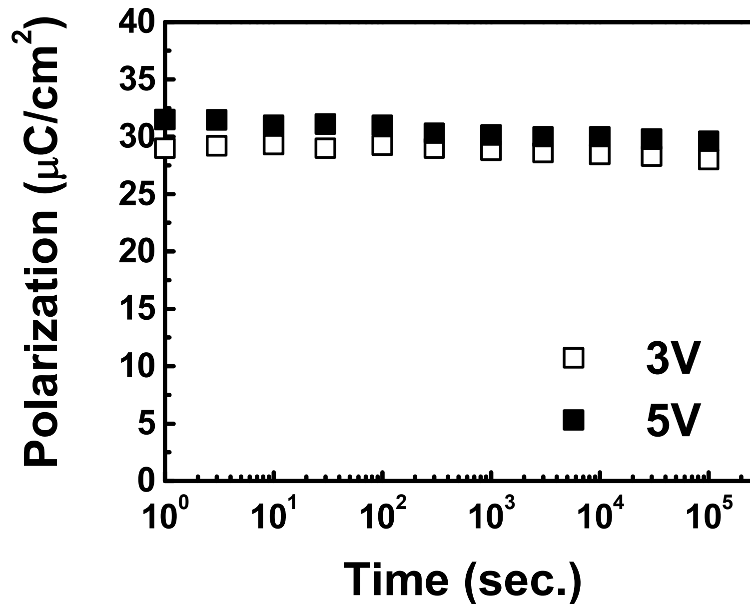

Figure 3-15. Retention characteristics of LSCO/PZT/LSCO capacitors as a function of time measured at 3 V and 5 V, respectively.

PZT with composition around MPB is known to display anomalously high dielectric and piezoelectric responses, which has also been observed in thin films. Accordingly, PZT thick films have attracted a great deal of attention as actuators with applications in MEMS devices.

The piezoelectric hysteresis loops for this MPB composition samples were measured by using piezoresponse microscopy, which has been successfully used to characterize piezoelectric properties of PZT capacitors.[82, 83] Figure 3-16 shows the piezoelectric hysteresis loops obtained from 230 nm- and 1, 3, 5 μm-thick $Pb(Zr_{0.5}Ti_{0.5})O_3$ films. The obtained maximum out-of-plane piezoelectric coefficients, i.e., d_{33}, were 199, 208, 226 and 218 pm/V, respectively, which are higher than values reported by other studies but still smaller than bulk value.

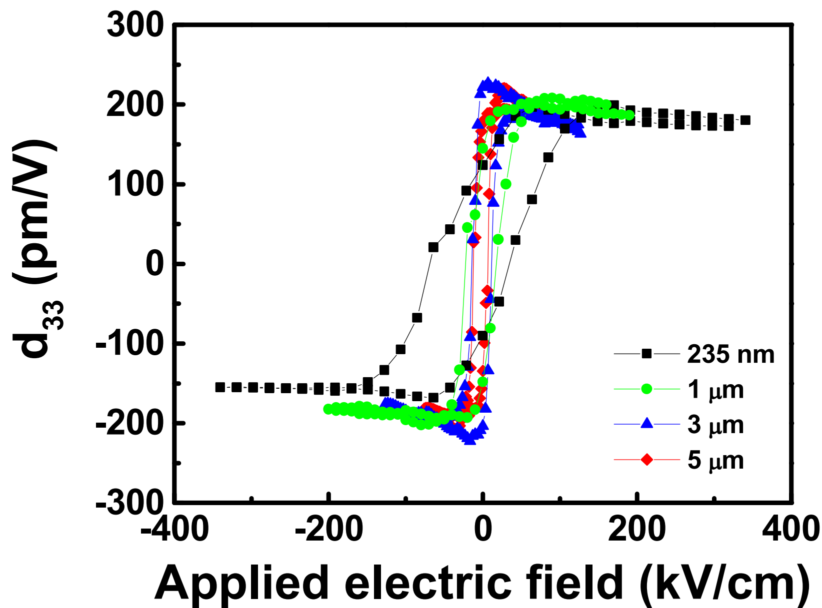

Figure 3-16. Piezoelectric hysteresis loops of 230 nm and 1, 3, 5 μm-thick $Pb(Zr_{0.5}Ti_{0.5})O_3$ films.

Further analysis on d_{33} values of films compared to that of bulk will be discussed in following section.

3.4 Comparison of piezoelectric properties of different thickness and composition

As indicated in previous section, the PZT family of ceramics is widely used in piezoelectric and dielectric applications. It was reported that compositions near the morphotropic phase boundary (MPB) have the largest piezoelectric constants.[84] Especially, [001] oriented bulk PZT shows maximum values of 327 pm/V for the tetragonal phase and above 500 pm/V for the rhombohedral phase. In this study, PZT films with different thickness from 230 nm to 5 μm were fabricated and piezoelectric properties were measured and compared with bulk values.

In order to avoid the complication induced by large discontinuity of d_{33} between tetragonal and rhombohedral structures, first we identified the structure of all the samples. Careful measurements were performed by ϕ-scan and in plane lattice parameter measurement. All the samples showed four-fold symmetry, which reveals the cube-on-cube epitaxy, and tetragonal structure was confirmed by calculation of *c/a* ratio (between 1.005 and 1.01). The obtained *c/a* values, which are smaller than that of bulk (1.025), illustrates the in-plane tensile stress in PZT films induced by the thermal mismatch between films and the Si substrate.

Figure 3-17 showed the variation of d_{33} values and coercive fields obtained from 230 nm, 1 μm, 3 μm and 5 μm thick films. The obtained d_{33} values showed

almost constant values between 199 pm/V and 225 pm/V within experimental error, while coercive field decreased sharply up to 1 μm and saturated at 10 kV/cm. In a previous study, the effect of misfit on d_{33} was demonstrated, where the d_{33} of PZT films on Si substrate were theoretically predicted. The obtained values in this study agree well with the previously reported results.[85]

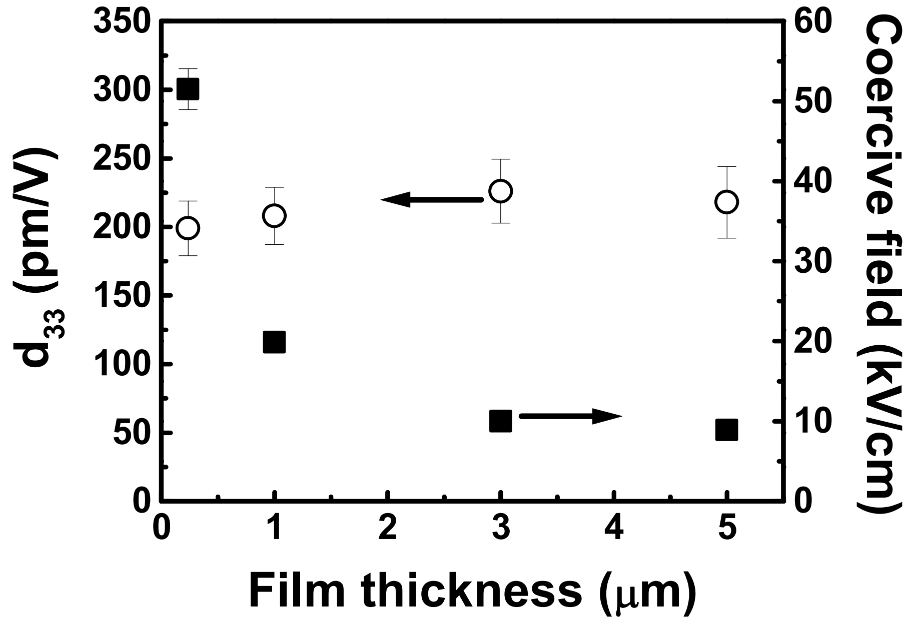

Figure 3-17. The changes of piezoelectric coefficient (d_{33}) and coercive field (E_c) with film thickness; ○ d_{33} of PZT films, ■ E_c of PZT films

The compositional dependence of d_{33} on the Zr/(Zr+Ti) ratio has been further investigated. All the samples were prepared with the thickness at 230±20 nm. Figure 3-18 demonstrates the relationship of experiment measured film d_{33} and the theoretical bulk d_{33} (by Haun *et al*) with the composition of PZT films.[86] The maximum d_{33}, 199 pm/V, was obtained at MPB composition. This tendency is in

good agreement with those of bulk PZT. For reference, the dependences of d_{33} on the Zr : Ti ratio obtained from PZT films grown by PLD and sol-gel are plotted in the same figure.[75,85] All the films were prepared on the same type of substrate (LSCO/STO/Si). Although the experimentally measured values of d_{33} are still significantly smaller than those theoretically predicted by Haun *et al*, PZT films prepared by different growth methods show a similar values and trend.

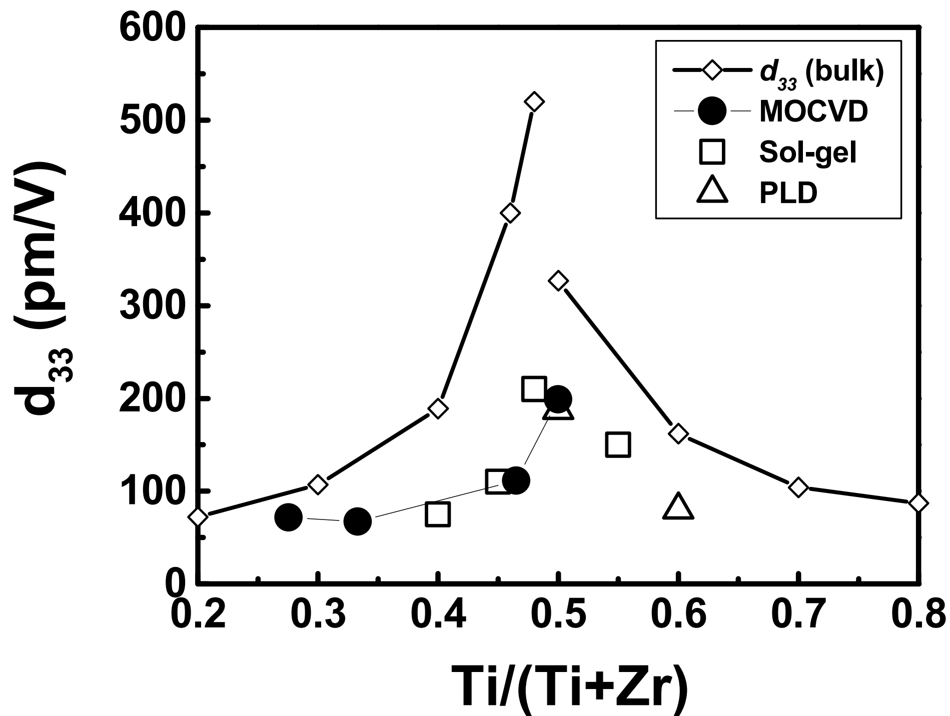

Figure 3-18. The changes of piezoelectric coefficient (d_{33}) with change of Ti/(Zr+Ti) ratio; -♦- d_{33} of bulk PZT calculated by Haun *et al*., ● d_{33} of thin PZT obtained from MOCVD.

The values of remanent polarization (P_r) and saturation polarization (P_s) from these hysteresis loops are plotted in Figure 3-19. For 0.27<x=[Ti/(Ti+Zr)]<0.55, P_r values were in the range of 20–33 μC/cm^2 and showed a clear dependence on x with a minimum near the morphotropic boundary.

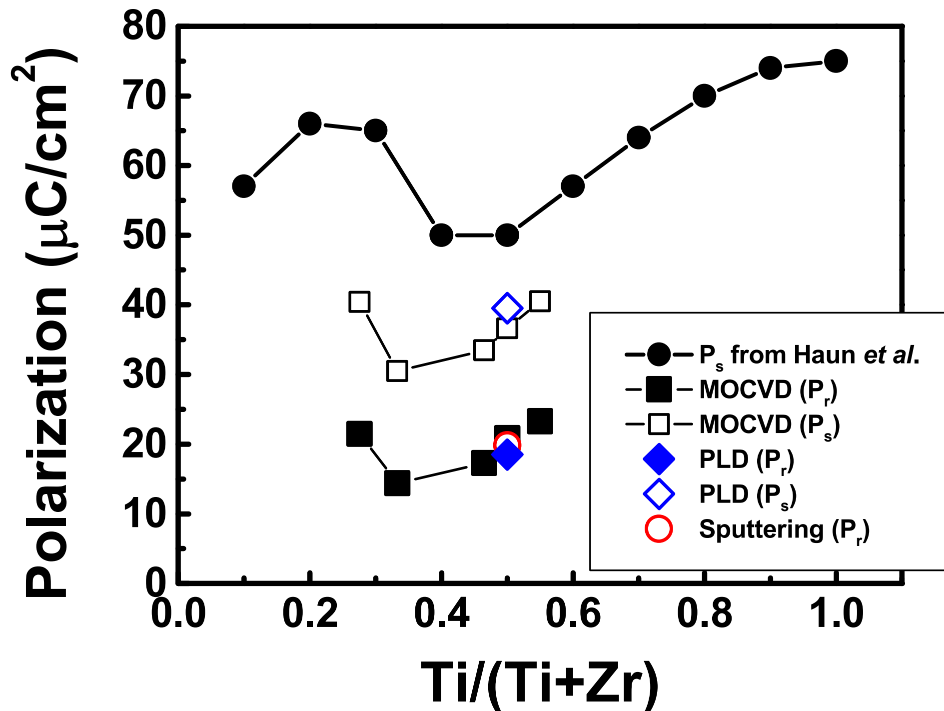

Figure 3-19. The variation of ferroelectric properties with change of Ti/(Zr+Ti) ratio; -•- P_s of bulk PZT calculated by Haun *et al.*, ■ P_r from MOCVD, P_s from MOCVD, ♦ P_r from PLD, ◊ P_r from PLD, and o P_r from Sputtering.

The P_r values for rhombohedral compositions were measured along <001> direction, but the polarization vector in these phases lies along the pseudocubic <111> direction. Consequently, for rhombohedral compositions, only a projection of

the total polarization vector on the <001> was measured and actual values of P_r must be higher than obtained values. The variation trend showed very similar to the theoretical values by Haun *et al*. but still showed small values, which is attributed to the thermal stress by the Si substrate and lattice mismatch strain between LSCO and PZT layers. These effects will be discussed in next chapter.

3.5 Discussion

It should be mentioned that measured piezoelectric coefficients are still smaller than theoretical value for bulk-PZT. This may be caused by several factors, for example, the clamping from substrate, which can be reduced by creating sub-micron islands of PZT capacitors (by Focused Ion Beam etching (FIB)). Accordingly, d_{33} values close to theoretical prediction from FIB processed PZT capacitors have been obtained where PZT films were prepared by pulsed laser deposition (PLD).[85] These results suggest that d_{33} values are substantially suppressed in continuous films by the clamping from the substrate.

The piezoelectric coefficient (d_{33}) can be expressed as a function of polarization (P), relative permittivity (ε_{33}), and electrostrictive coefficient (Q) according to the Eq. (3-2).[87]

$$d_{33} = 2Q\varepsilon_{33}P \qquad (3\text{-}2)$$

The suppression of d_{33} by the clamping from substrate can be expressed by the Eq. (3-3).[88]

$$d_{33}^{f} = d_{33}^{b} - \frac{2S_{13}^{E}}{S_{11}^{E} + S_{12}^{E}} d_{31}^{b} \tag{3-3}$$

where, f and b denotes "film" and "bulk", respectively, and S_{ij} are elastic compliances.

Considering the 50/50 composition films,

d_{31}^{b} = - 156 pm/v, d_{33}^{b} = 327 pm/v (in tetragonal phase boundary),

S_{13}^{E} = - 4.22×10^{-12} m^{2}/N, S_{11}^{E} = 12.4×10^{-12} m^{2}/N, S_{12}^{E} = - 4.06×10^{-12} m^{2}/N,[86]

then,

$d_{33\ (001)}^{f}$ = 327 – 158 = 169 pm/v is expected from for single c-domains and closed to experimentally observed values.

Chapter 4: Thickness effects in epitaxial $Pb(Zr,Ti)O_3$ films grown by MOCVD

4.1 Background

The stringent need for high-density, high-speed, and low-power memory devices has prompted an immense interest in studying the size effect in ferroic systems. However, a progressive degradation of ferroelectric properties has been generally observed including the decrease of remnant polarization, the increase of coercive field and a lower phase transition temperature with decreasing film thickness.[89,90,91] Consequently, the critical thickness of a ferroelectric thin film, *i.e.*, the thickness limit when the ferroelectricity becomes unstable, has become an issue of tremendous interest.

Based on the research performed during the last decade, several models have been proposed to explain the size effect including both experimentally induced imperfect film structures originating from deposition process, and theoretically predicted intrinsic phenomena. The former describes the presence of a non-switching and low-permittivity layer at the ferroelectric-electrode interface; meanwhile the other comprises depletion, surface intrinsic effect and depolarizing effects. However, both theoretical and experimental results have shown that critical thickness has been changed with time.

Larsen *et al.* proposed blocking layer model where the presence of a non-ferroelectric blocking layer in ferroelctric capacitors made with PZT films[92]. By correcting for the influence of this layer, it was found that there is no thickness dependence of ferroelectric properties, at least down to a thickness of 0.1 - 0.2 μm. Meanwhile, Yanase *et al*. successfully reported sharp hysteresis loops and low leakage in a 12 nm thick $BaTiO_3$ film grown on $SrRuO_3$ bottom electrodes, with a $2P_r$ value of 65 $\mu C/cm^2$.[93] Moreover, the recent first principle calculations for a realistic $BaTiO_3$ thin films between two epitaxial metallic $SrRuO_3$ electrodes under short circuit conditions have shown that the critical thickness for ferroelectricity is of the order of 6 unit cells which corresponds to 2.4 nm[94] where the reason for the disappearance of a stable polar state was demonstrated to be a depolarizing electrostatic field.

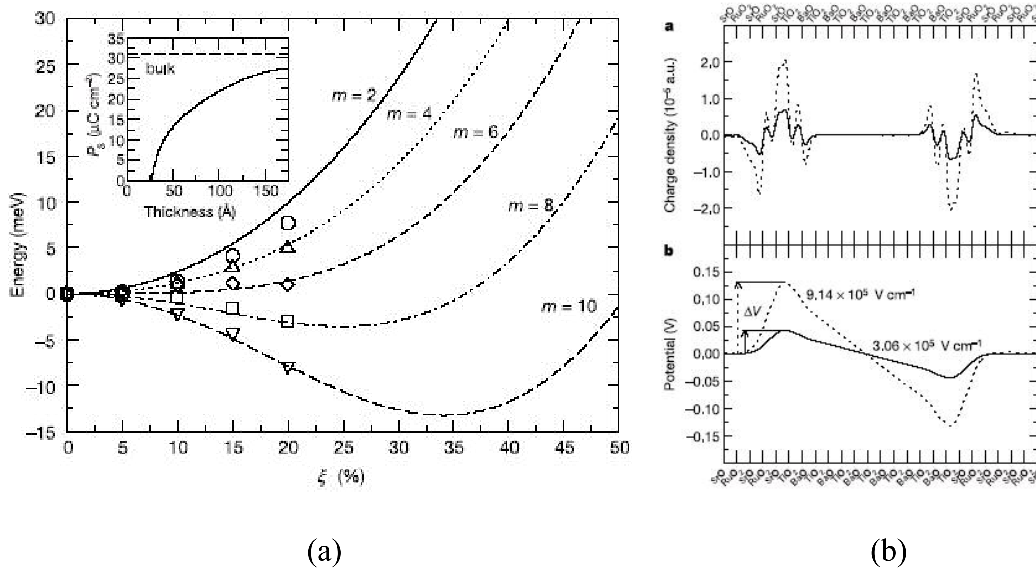

(a) (b)

Figure 4-1. (a) Evolution of the energy as a function of the soft-mode distortion ξ. (b) Induced dipoles, potentials and depolarizing fields along the [001] direction of the short-circuited ferroelectric capacitor. [Ref. 94]

In parallel, current nonvolatile memory manufacturing processes require a scalable process such as metalorganic chemical vapor deposition (MOCVD) to grow ferroelectric layers. Attempts to scale the operating voltage by reducing PZT thickness are generally hampered by a substantial increase in coercive field (E_c) and a marked decrease in switched polarization (P_{sw}), particularly below 100 nm. Accordingly, the research on thin film (t_{film}<100 nm) growth by MOCVD has been intensified to improve the properties and the understanding of size dependent phenomena in thin films.

Physical vapor deposition (PVD) techniques, such as pulsed laser deposition (PLD) and sputtering, have been employed to prepare samples for studying the size effect in thin films because of the facile control of the stoichiometry.[89,95,96] Only a few quantitative studies on the properties of ultra-thin $Pb(Zr_xTi_{1-x})O_3$ (PZT) films grown by MOCVD have been reported.[90,97] However, quantitative results on the effects of thickness scaling down to a few 10's nm have been rarely reported because of the complications in the chemical reaction and difficulties in controlling the growth process in CVD. The experimental data, even for hundred of nanometers thick films, have shown polarization values smaller than those predicted by theoretical calculations. These findings have been explained by the presence of non-ferroelectric interfacial layers and/or dislocations in films prepared by MOCVD.[92,98] Up to date, only a few films with intrinsic polarization values have been reported.[99] In order to investigate this size effect, preparing high quality films is the most important pre-condition.

Another key aspect for reliable quantitative analysis of ultra-thin films is to employ a suitable measurement technique. Traditionally, *P-E* hysteresis loop measurements have been used to evaluate the ferroelectric properties in thin films. However, polarization measurements for ultra-thin films are primarily dominated by leakage and other methods are required.

A variety of techniques have been introduced to investigate ferroelectricity of ultra thin film. Fong *et al*. observed ferroelectric phase of $PbTiO_3$ on STO substrate down to 3 unit cell thickness by observing the stripe domain formation with synchrotron X-ray technique.[100] Another example is that polarization dynamics in ferroelectric films has been successfully studied at sub-micron scale with scanning probe microscopy techniques. Notable examples are the works of Ahn *et al.* and Tybell *et al.* in which the time dependence of local piezoelectric and electric field signals suggests a stable ferroelectric polarization in PZT films down to thickness of 40 Å (10 unit cell).[101] The advantage of the piezoelectric force microscopy (PFM) technique is the reduced sensitivity to leakage currents, which is a major problem in measuring ferroelectric properties for ultra-thin films. Previous research also has shown that the polarization dynamics in ferroelectric films can be successfully studied at submicron scale with scanning probe microscopy techniques.[101,102,103]

The approach in this study is based on two steps. First, epitaxial PZT films with bulk-like properties were prepared, to enable the extraction of intrinsic properties from extrinsic effects. Second, the thickness effect is investigated by probing the local piezoelectric response by PFM.

4.2 Thickness effects in PZT thin films : a model system

Selecting suitable buffer layers between substrate and film can control the strain in the film. In the case of capacitor devices, bottom electrode layers can play a critical role as a buffer layer as well as conducting layer. Accordingly, the choice of electrode materials must be considered for desirable electrical and crystalline properties of PZT.

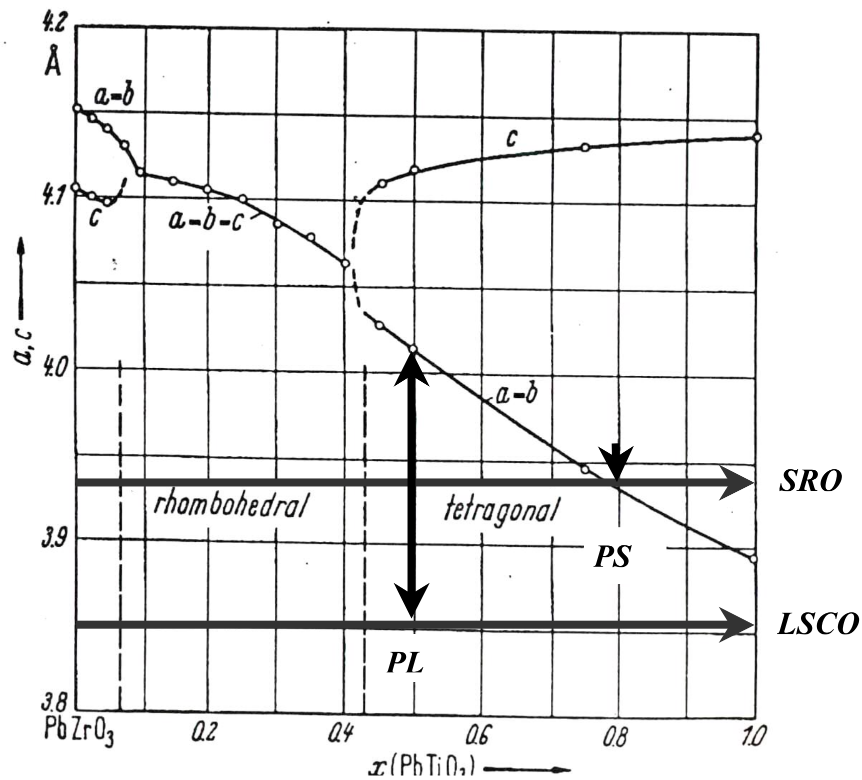

Figure 4-2. The lattice parameter constant variation with different composition of zirconium to titanium in PZT. Lattice constants for electrodes (LSCO and SRO) are also indicated.

Figure 4-2 demonstrates the lattice parameter constant variation with different composition of zirconium to titanium in PZT. The key factor of this figure is to compare the in-plane lattice constant misfit strain between PZT and electrodes. This misfit strain can be expressed as Eq. (4-1).

$$\varepsilon_M = \frac{a_{PZT} - a_{electrode}}{a_{PZT}} \qquad (4\text{-}1)$$

Lattice mismatch between LSCO bottom electrode and $Pb(Zr_{0.5}Ti_{0.5})O_3$ is pointed as *PL*, which is about 3.75 % misfit strain. On the other hand, $SrRuO_3$, which is also conductive metal oxide, can be outstanding candidate as a bottom electrode layer because of its excellent lattice match with STO and $Pb(Zr_{0.2}Ti_{0.8})O_3$.

First, different thickness of $Pb(Zr_{0.5}Ti_{0.5})O_3$ films were prepared on LSCO/STO substrates. $SrTiO_3$ was selected as a substrate because the thermal mismatch with PZT thin film is smaller than that with Si substrate. *P-E* hysteresis loops and switching polarization (ΔP) obtained from 20, 40, 70, 100 and 200 nm thick $Pb(Zr_{0.5}Ti_{0.5})O_3$ films are shown in Figures 4-3(a) and (b). It was observed that the decrease of polarization in the wide range of the thickness as film thickness decreased and smaller polarization than theoretically expected intrinsic value was obtained even with 200 nm thick films.

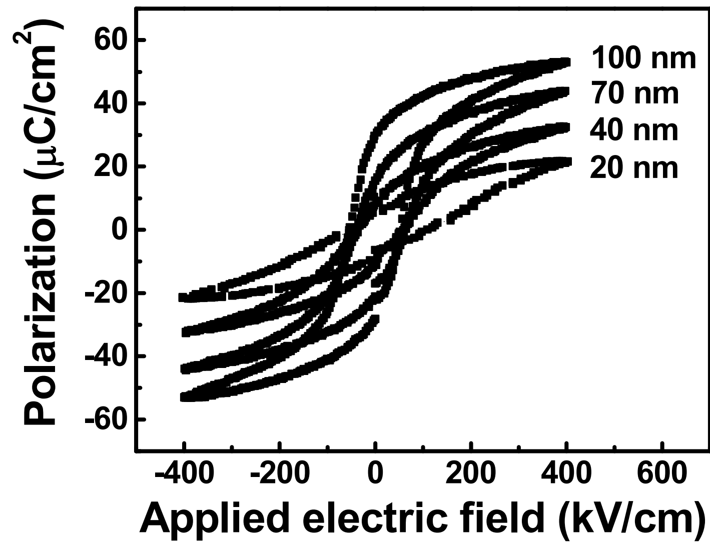

(a)

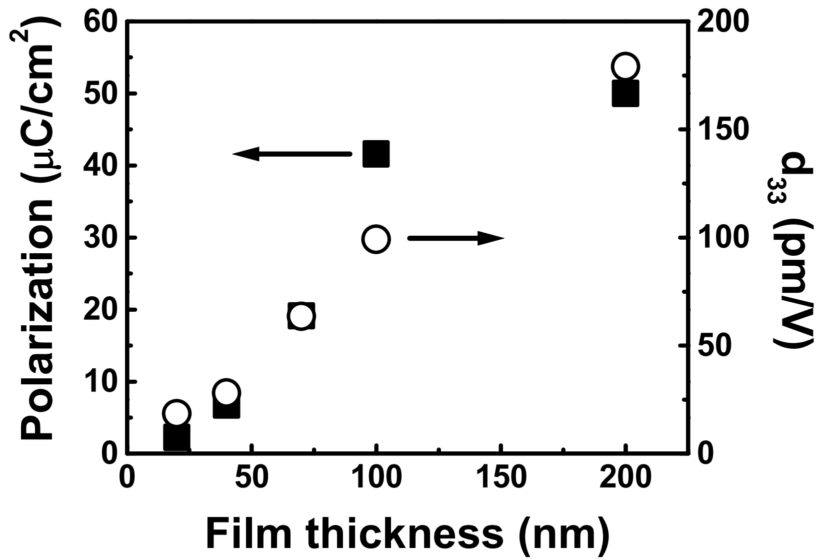

(b)

Figure 4-3 (a) *P-E* hysteresis loops and (b) Switching polarization and d_{33} for 20, 40, 70, 100 and 200 nm thick $Pb(Zr_{0.5}Ti_{0.5})O_3$ films on LSCO/STO substrate.

In order to confirm the film quality, the thickness dependence of the polarization and piezoelectric coefficient obtained from MOCVD-$Pb(Zr_{0.5}Ti_{0.5})O_3$ films was compared with the results obtained from $Pb(Zr_{0.5}Ti_{0.5})O_3$ films grown by sputtering method (prepared by Prof. Eom group in Univ. of Wisconsin-Madison). As shown in Figure 4-4, similar switching polarization (ΔP) and d_{33} values and scaling behaviors were obtained from $Pb(Zr_{0.5}Ti_{0.5})O_3$ films prepared by two different growth methods. Both ΔP and d_{33} show the drastic decrease around 250 - 300 nm.

In epitaxial films and heterostructures, the strain due to lattice mismatch between the film and the substrate can be relaxed by the formation of misfit dislocations at the film-substrate interface. The relation between the critical thickness for the formation of misfit dislocation and misfit strain can be described by the Matthews-Blakesee model [Eq. (4-2)].

$$h_C = \frac{b}{8\pi(1+\nu)\varepsilon}\left[\ln\left(\frac{h_C}{b}\right)+1\right] \qquad (4\text{-}2)$$

where, h_c is the critical thickness for misfit dislocation formation, ν is the Poisson's ratio, b is the Burger's vector, and ε is the lattice mismatch.

This misfit dislocation acts as an extrinsic dominating factors, such as depolarizing field formation, in the scaling of polarization,[104,105,106] which can be significantly suppressed by selecting an optimum combination of substrate and PZT-composition.

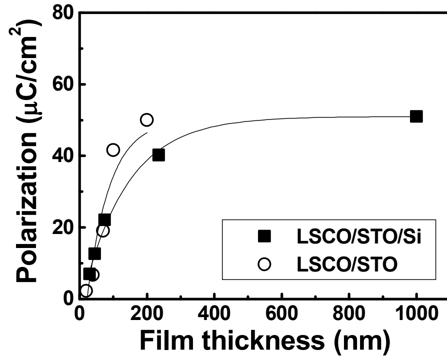

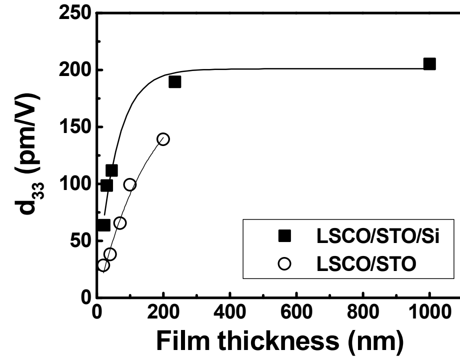

(a) (b)

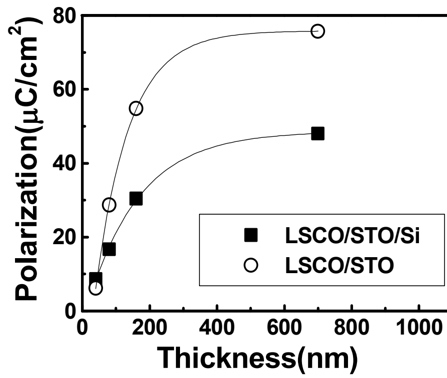

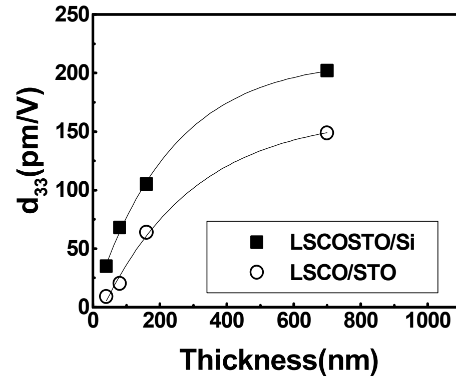

(c) (d)

Figure 4-4 (a) ΔP vs film thickness (b) d_{33} vs film thickness from MOCVD-$Pb(Zr_{0.5}Ti_{0.5})O_3$ films, (c) ΔP vs film thickness (d) d_{33} vs film thickness from Sputtering-$Pb(Zr_{0.5}Ti_{0.5})O_3$ films.

As indicated in Figure 4-2, the approach of lattice engineering scheme to investigate the thickness dependence was changed (from *PL* to *PS*).

As far as the composition of PZT films is concerned, we have focused on $Pb(Zr_{0.2}Ti_{0.8})O_3$ with the conducting perovskite, $SrRuO_3$ (SRO) [pseudocubic with a=0.393 nm (calculated from the orthorhombic lattice parameters of a = 0.557, b = 0.553, and c = 0.785 nm)]. SRO is one of the most promising conductive metallic oxides with very good thermal conductivity and stability, and high resistance to chemical corrosion. $Pb(Zr_{0.2}Ti_{0.8})O_3$ thin films were prepared on $SrRuO_3$(SRO) / $SrTiO_3$(STO) (001) substrates by liquid delivery MOCVD. SRO bottom electrode with 50 - 60 nm thickness was deposited by pulsed laser deposition (PLD) at 630 ^{o}C for 35 minutes.

AFM topographic images of the as-grown SRO bottom electrode surface (Figure 4-5) showed that the surface is atomically flat terraces separated by single and double atomic steps. Thus, these layers are applicable to the heteroepitaxial growth of further oxide layers in applications requiring a conducting bottom layer.

The high surface quality (near-perfect) for under-layer is preliminarily required to minimize leakage and surface roughness of PZT films.

For the quantitative electrical and electromechanical measurement, Pt was deposited as the top electrode with 18-32 mm diameter circular pads patterned by standard lift-off lithography processes.

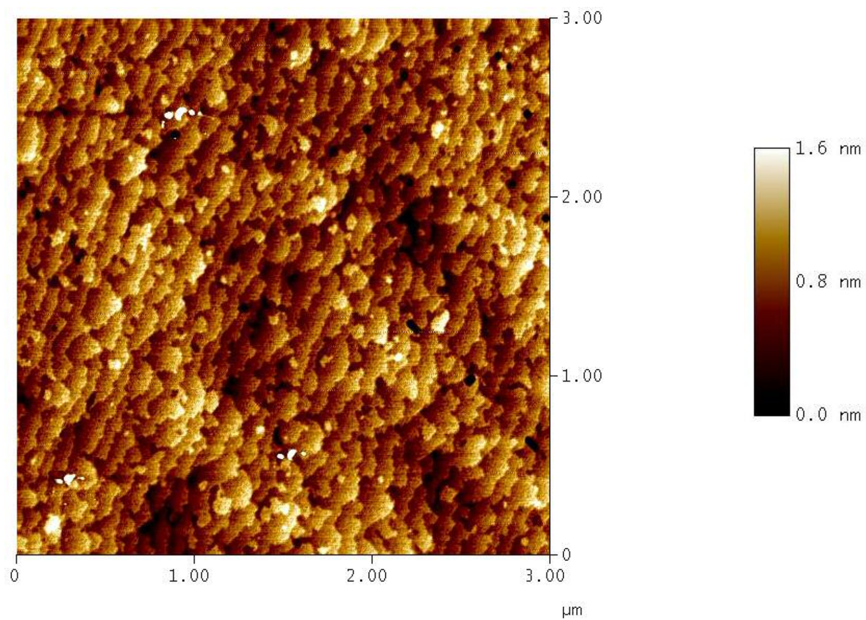

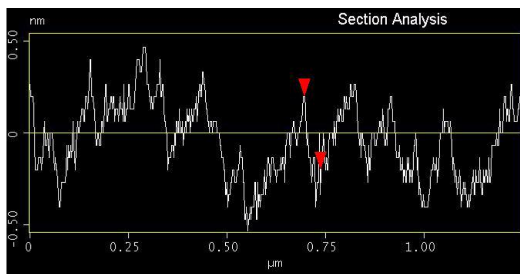

Figure 4-5. AFM images of the SRO bottom electrode surface

4.3 The thickness effects in $Pb(Zr_{0.2}Ti_{0.8})O_3$ thin films

Prior to studying ultra thin films, we prepared and studied the ferroelectric properties of relatively thick PZT films (~130 nm).

A typical θ - 2θ x-ray diffraction scan of PZT/SRO is shown in Figure 4-6 (a), indicating that the PZT/SRO heterostructure is highly [*00l*] oriented without any secondary phase. The in-plane ϕ-scan around the (101) peak shown in the inset in Figure 4-6 (a) further confirms that the films grow with the expected cube on cube four-fold symmetry. A *c*-axis lattice parameter of 4.14 Å was calculated from (002) peak from the PZT diffraction patterns.

These films exhibited excellent crystalline property with ω - rocking full width at half maximum (FWHM) of 0.26^{o} and the minimum-channeling yield (obtained from RBS) of 10 - 15 %.

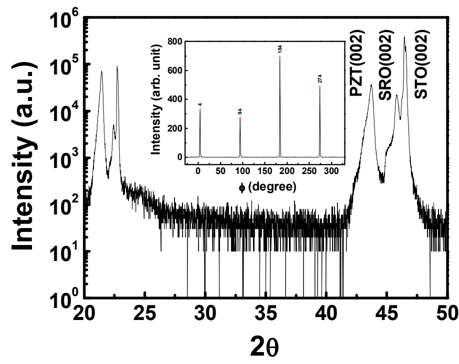

(a)

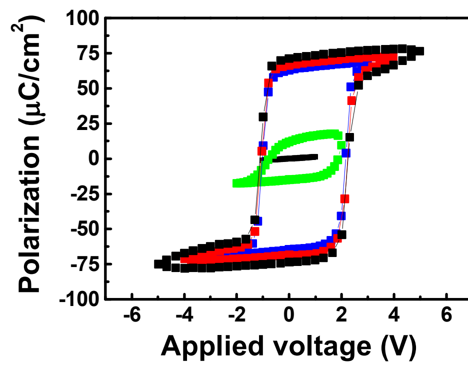

(b)

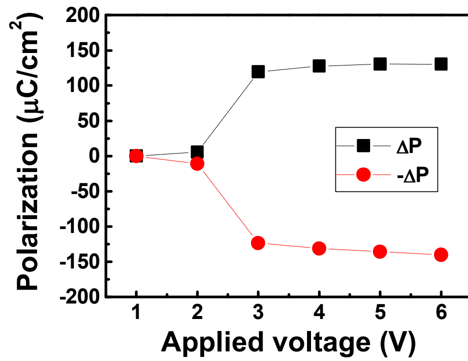

(c)

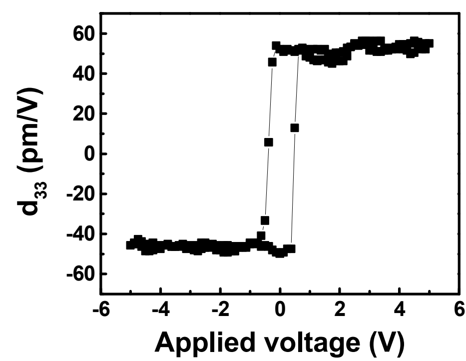

(d)

Figure 4- 6(a) A typical θ - 2θ x-ray diffraction scan of 130 nm thick PZT/SRO/STO. The in-plane ϕ-scan around the (101) peak shown in the inset. (b) *P-E* hysteresis loops measured at a frequency of 16 kHz. (c) PUND ($\Delta P = P^{*}$ (switched polarization) - $P^{\wedge}$ (non-switched polarization)) measurement. (d) Piezoelectric hysteresis loop measured at room temperature.

Sharp and square P-E hysteresis loops were obtained, with the remanent polarization values ($2P_r$) of about 145 μC/cm^2 as shown in Figure 4-6 (b), which correspond to bulk-like ferroelectric properties.[107] To extract the intrinsic polarization switching, PUND (ΔP = P^*, *i.e.* switched polarization, - $P^\wedge$, *i.e.* non-switched polarization) measurements were also performed and it was confirmed that obtained values of $2P_r$ are consistent with the switched polarization, ΔP [Figure 4-6(c)].

The out-of-plane piezoelectric coefficient (d_{33}) value of 60 – 65 pm/V obtained from piezoelectric hysteresis loop is shown in Figure 4-6(d). The experimentally obtained piezoelectric coefficient is in good agreement with theoretical calculations for d_{33} of clamped PZT films.[108,109]

A set of hysteresis loops for 25, 34 and 130 nm thick films measured at a frequency of 16 kHz is shown in Figure 4-7. The remanent polarization values ($2Pr$) of 140 - 150 μC/cm^2 were also observed with 25 and 34 nm thick films. Asymmetric coercive fields were observed due to the asymmetric electrical boundary conditions between the top (Pt/PZT) and bottom (PZT/ SRO) electrode interfaces. Small openings were observed in the hysteresis loops of the 25 and 34 nm thick films which are attributed to the leakage component effects in Pt top electrode side. The intrinsic polarization switching was measured by pulse polarization measurement [PUND, ΔP = P^*, *i.e.* switched polarization, - $P^\wedge$, *i.e.* non-switched polarization] which is less likely convoluted by leakage and nonlinear dielectric effects, and these polarization values were confirmed.

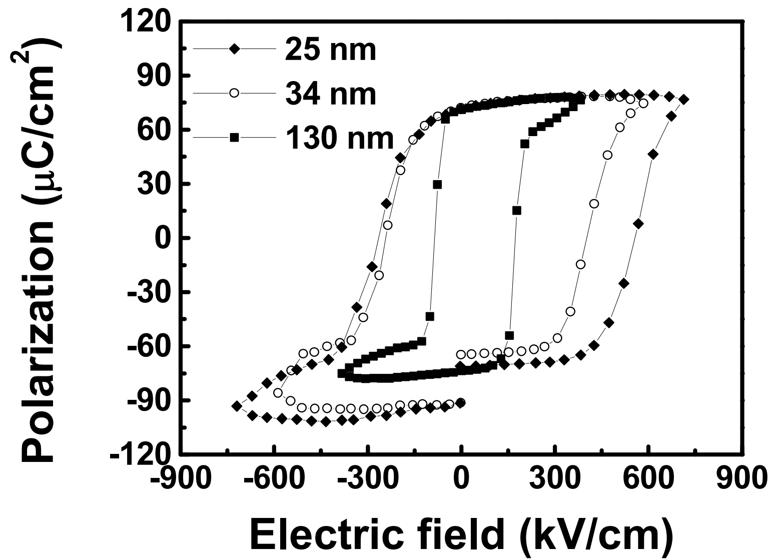

Figure 4-7. Ferroelectric hysteresis loops as a function of electric field for 25, 34 and 130 nm thick PZT films measured at 16 kHz.

Figure 4-8 shows piezoelectric hysteresis loops measured at room temperature. Out-of-plane piezoelectric coefficient (d_{33}) values of 55 – 65 pm/V in the thickness range of 17 – 130 nm were obtained. For the 17 nm thick film, a saturated d_{33} (E) hysteresis loop with 55 pm/V was observed, but unsaturated *P-E* polarization loops due to high leakage current density were measured. This demonstrates that the quantitative determination of d_{33} using an AFM setup is significantly less convoluted by leakage, because the mechanical displacement of the cantilever is solely used for this measurement. However, due to the large top electrode size, measurements on films thinner than about 17 nm were mainly affected by leakage, and the results were unreliable. *P-E* and d_{33}-E hysteresis loops obtained from 17 nm thick film are shown in Figure 4- 9.

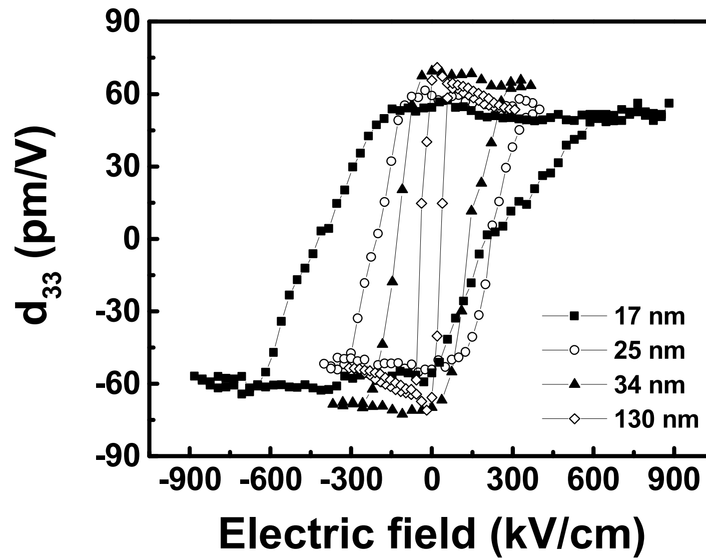

Figure 4-8. Piezoelectric coefficients, d_{33}, loops as a function of electric field for 17, 25, 34 and 130 nm thick PZT films.

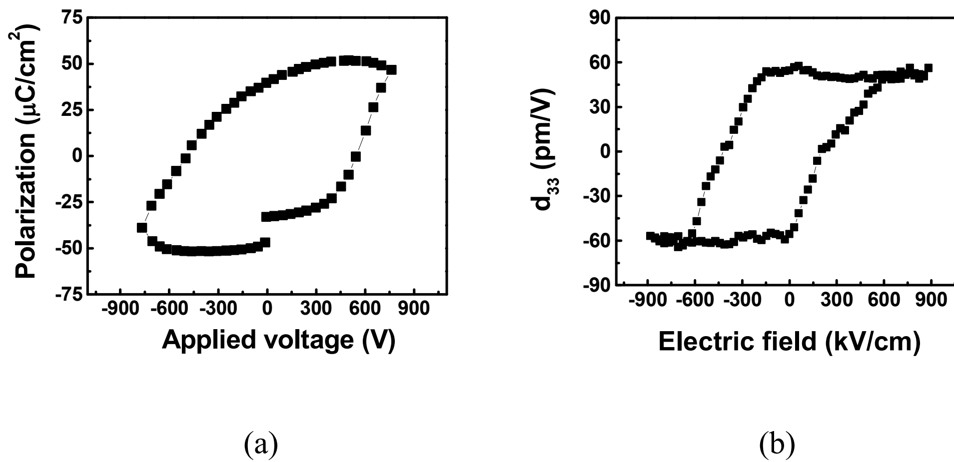

(a) (b)

Figure 4-9 (a) Ferroelectric hysteresis loop and (b) piezoelectric coefficients, d_{33}, loop for 17 nm thick PZT film.

Therefore, local out-of-plane piezoelectric response measurements were performed to study ferroelectricity in films thinner than 20 nm. The film thickness was determined by cross section TEM images. Low magnification and high-resolution cross-sectional TEM images of 34 nm thick PZT film are shown Figure 4-10 (a) and (b).

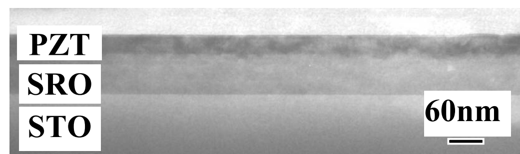

(a)

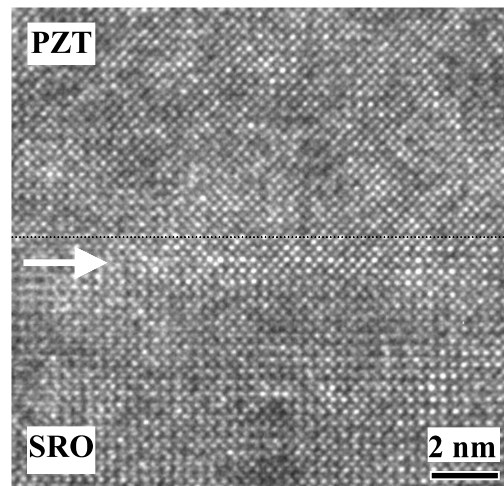

(b)

Figure 4-10 (a) low magnification and (b) high resolution cross-section TEM images of 34 nm thick PZT film.

There was no second phase observed in TEM images and the epitaxial growth with a sharp interface between PZT and SRO was confirmed. In addition, the 90° domains are not observed with this thickness range.

Figures 4-11 (a), (b) and (c) show piezoelectric response images for the 34, 17, and 8 nm thick films. First, the films were poled at a positive dc-bias by scanning over an area of 1×1 μm^2, followed by another poling at the opposite bias over a 0.5×0.5 μm^2 area inside the previously poled area. The magnitude of the piezoelectric response is defined as the peak-to-peak value of measured signal as shown in figures. The obtained signal magnitudes were 863.4 mV for 34 nm, 562.5 mV for 17 nm and 357.1 mV for 8 nm thick films, respectively.

A clear piezoresponse image with a signal magnitude of 5.2 mV, which is well above the noise level, was measured on a film as thin as 3.6 nm as shown in Figure 4-12 (c). This image was obtained after a 1.5 V dc poling, by scanning with the probe at an ac bias of 0.3 V_{pp}. From the high resolution TEM image in Figure 4-12 (b), 8 - 10 unit cells of PZT films were counted.

This thickness is very close to the theoretically calculated critical thickness for a $BaTiO_3$ ferroelectric film by Junquera and Ghosez, where they predicted the critical thickness for $BaTiO_3$ thin films under short circuit conditions is 6 unit cells which corresponds to 2.4 nm.[94]

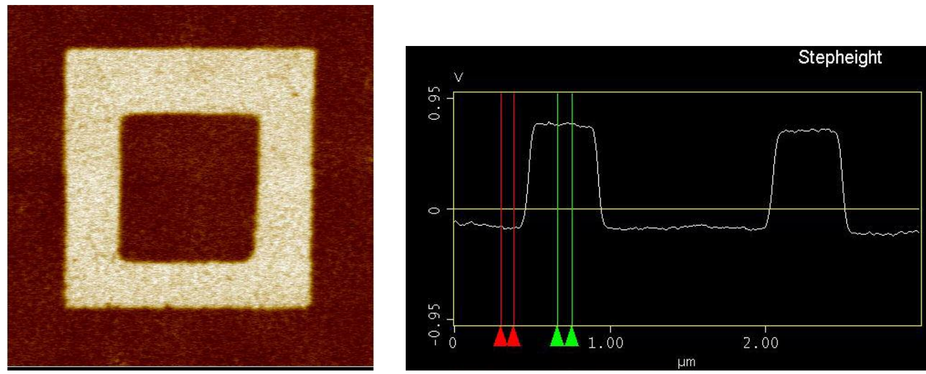

(a)

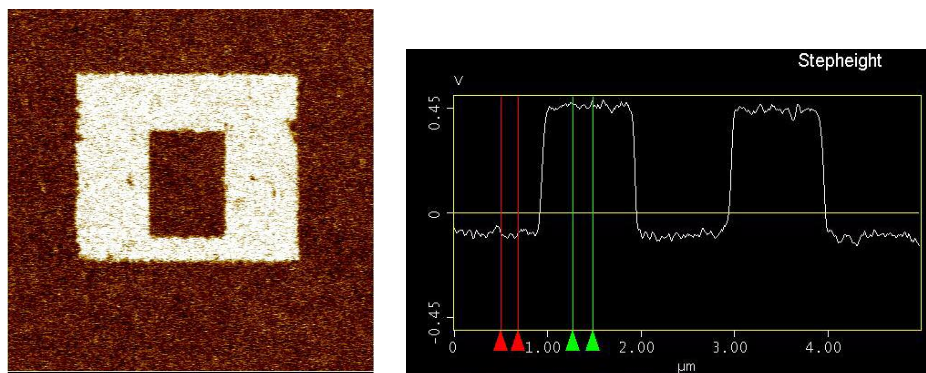

(b)

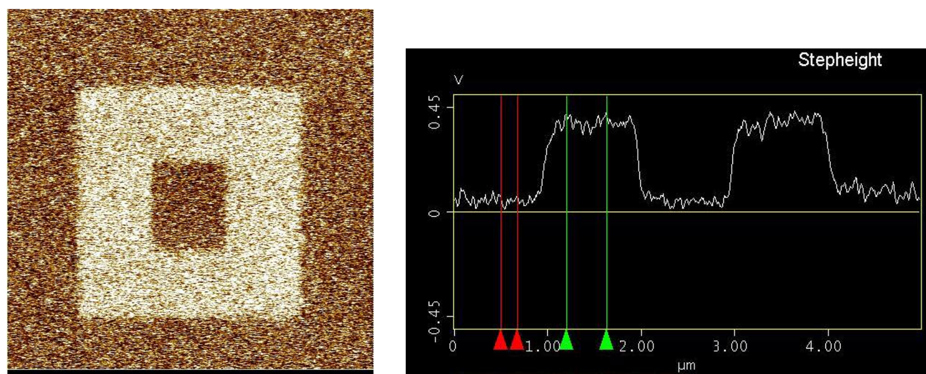

(c)

Figure 4-11. Piezoelectric response images for (a) 34 nm (b) 17nm and (c) 8 nm thick films. Piezoelectric response heights of 863.4 mV, 562.5 mV and 357.1 mV were observed, respectively.

(a)

(b)

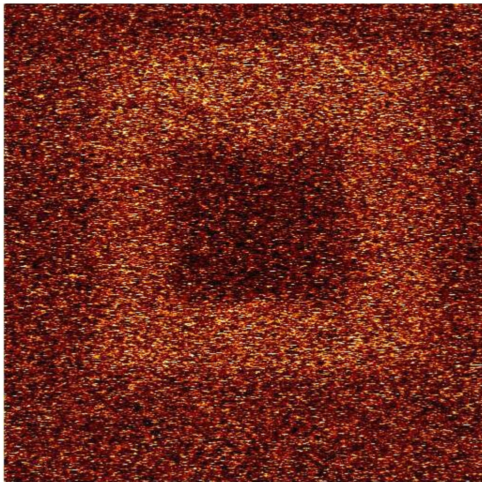

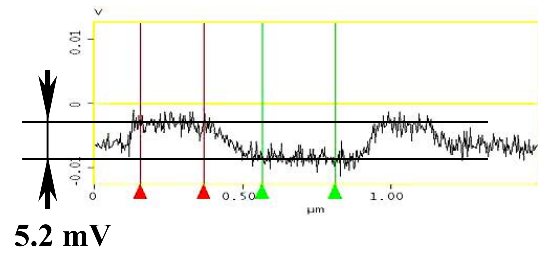

(c) (d)

Figure 4-12 (a), (b) Cross-section TEM images of 3.6 nm thick PZT film. (c) Piezoelectric response images from 3.6 nm thick PZT films (8-10 unit cells). (d) Piezoelectric response of 5.2 mV was observed with ± 1.5 V and 0.3 V_{pp}.

In contrast to polarization and d_{33}, a drawback of the PFM technique is the difficulty of making quantitative analyses because of the inherent variations in the tip elastic constants, and also the uncertainties in electric field distribution at the tip apex.

In order to quantify the thickness dependent behavior, the measured piezoelectric response signals were normalized to the value obtained from a 34 nm thick film (863.4 mV) with same electric field. All the measurements were carefully performed and confirmed by calibrating with the value obtained from 34 nm thick films before and after measuring new samples. This is a reasonable approach because the 34 nm thick films show almost the same polarization and converse piezoelectric coefficient values as the 130 nm thick films which are considered bulk-like in terms of the ferroelectric properties.

Figure 4-13 shows the dependence of ferroelectric order parameters (switching polarization, and d_{33}) on the film thickness, and the local piezoelectric response. Polarization and d_{33} values were normalized with respect to the theoretically expected values for substrate-clamped films.[110]

An abrupt drop of the normalized order parameters is observed between 10 nm and 20 nm thick films. Responsible for this decay can be imperfect film structures grown during the deposition process, but theoretical calculations suggest that intrinsic and extrinsic phenomena may produce the same effect.

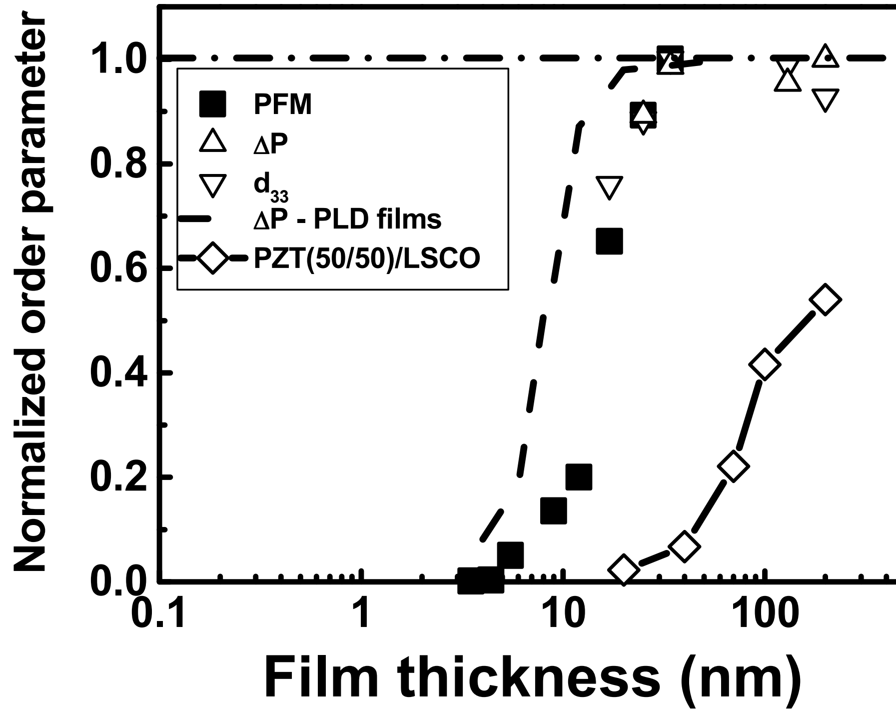

Figure 4-13. The behavior of ferroelectric order parameters in PZT films with film thickness. Normalized amplitudes from PFM (■), ΔP (Δ) and d_{33} (∇) measurements of $Pb(Zr_{0.2}Ti_{0.8})O_3$/SRO were plotted. The dash-line plot shows the experimental result from PLD-PZT (Nagarajan *et al.*). The dependence of polarization (*ΔP*) on thickness in $Pb(Zr_{0.5}Ti_{0.5})O_3$/LSCO is also plotted in same scale.

Experimentally induced imperfections involve the presence of a non-switching, and low-permittivity layer at the ferroelectric-electrode interface. As a comparison, the results on thickness scaling of polarization in $Pb(Zr_{0.5}Ti_{0.5})O_3$ films with a $LaSrCoO_3$ (LSCO) bottom electrode are shown in the same figure. In this

system, the mismatch strain ($\varepsilon = \frac{a_{PZT} - a_{LSCO}}{a_{PZT}}$) measured from XRD was 1.4 %, which is almost one order of magnitude larger than the one measured for $Pb(Zr_{0.2}Ti_{0.8})O_3$ on SRO (0.2 %). In the $Pb(Zr_{0.5}Ti_{0.5})O_3/LaSrCoO_3$ system, polarization does not saturate even at 250 nm thick films. As pointed out previous section, this demonstrates that the formation of misfit dislocations or imperfect interfacial layers due to large lattice mismatches or intermixing can induce a critical degradation of ferroelectricity in thin films.

The theoretical models take into account depletion, intrinsic surface and depolarizing effects, while a perfect structure is assumed. Recent results suggested that the depolarizing field governs the suppression of ferroelectricity. A quantitative study of the size effect was experimentally performed by Nagarajan *et al*.[89] In this study, a pulsed probing technique was used to measure the switching polarization of PZT films grown by PLD and the size effect was scaled. It was suggested that the depolarizing field governs the suppression of ferroelectricity as suggested by Junquera and Ghosez.[94] Those data are also plotted in Figure 4-13 for comparison, and show a similar behavior to the piezoelectric response results obtained on MOCVD-grown films.

Although the critical thickness observed from MOCVD-PZT films is almost same or even smaller than that of PLD-PZT films, small shift to the thicker side was observed. This small deviation in scaling behaviors between PLD-films and MOCVD-films may originate from two main factors. First, the possible existence of error range or sensitivity of different measurement techniques may give rise to the different values.

The other critical reason for this deviation may be induced by the film crystallinity or composition change with thickness.

The surface chemical bonding state analysis on 4 and 17 nm thick PZT films was performed by X-ray photoelectron spectroscopy (XPS). Typical XPS analysis uses an incidence angle normal to the sample surface. However, it is necessary to employ the low incidence angle (grazing incidence) to discern more clearly between the surface and bulk states. XPS analysis was carried out with two different incidence angle conditions. The high-resolution XPS results show no observable peak shift in Pb, Ti, and Zr peaks for 4 and 17 nm thick films in both incidence angle conditions as shown in Figure 4-14 (Pb 5d = 412.5 eV, Zr $3d_{5/2}$ = 180.4 and Zr $3d_{3/2}$ = 182.8, Ti $2p_{3/2}$ = 457.3 and Ti $2p_{1/2}$ = 463, O 1s = 528.9). However, it was found that the peak widths of Zr peaks are wider for the 4 nm film compared to the 17 nm films, which is more clearly observed in grazing incidence angle measurement. This demonstrates that the Zr chemical bonding states influenced by chemical surrounding could be different in 4 and 17 nm thick films and the broadening in a few top layers is more pronounced. XPS work on PZT films by Vaidya *et al*. showed that the spin-orbit split Zr 3d peak exhibits two binding states one at Zr $3d_{5/2}$ = 180.3 and Zr $3d_{3/2}$ = 182.7 eV and the other at Zr $3d_{5/2}$ = 181.4 and Zr $3d_{3/2}$ = 183.8 eV. The lower bonding energy doublet of the Zr 3d peak was assigned to Zr atoms present in the form of an oxide in PZT, while the second Zr 3d doublet (Zr $3d_{5/2}$ = 181.4 and Zr $3d_{3/2}$ = 183.8 eV) is shifted from the lower bonding energy doublet by about +1eV. It was suggested that this species is consistent with a hydroxylated metal species, probably of the form $PbZrO_x(OH)_{3-x}$.[111]

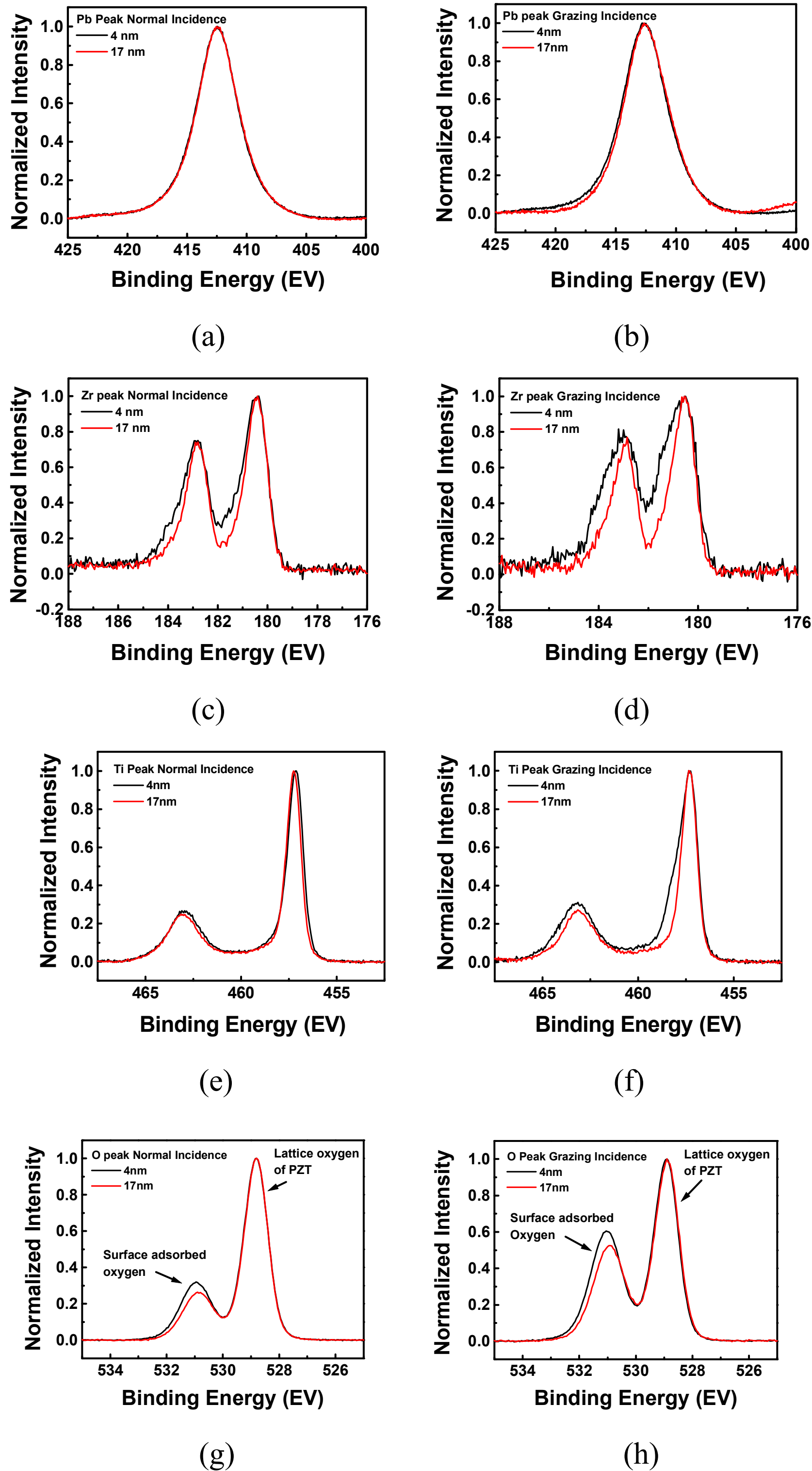

Figure 4-14. XPS analysis on 4 and 17 nm thick PZT films. Normal (a), (c), (e), (g) and grazing incidence (b), (d), (f), (h) measurements. (a) and (b) : Pb (5d); (c) and (d) : Zr (3d); (e) and (f) : Ti (2p); (g) and (h) : O (1s).

X-ray photoelectron spectrum obtained from Zr 3d in 4 nm thick film can be interpreted by using this model. The precursor of Zr used in this study is Tetrakis(dimethylheptanedionate)zirconium, [Zr(dmhd)$_4$, $(C_9H_{15}O_2)_4Zr$], and the hydroxide from this metalorganic source can be incorporated into PZT films when it is not completely decomposed to form ZrO_2. Accordingly, Zr spectrum measured from 4 nm thick film is composed of two different chemical states as proposed in Figure 4-15.

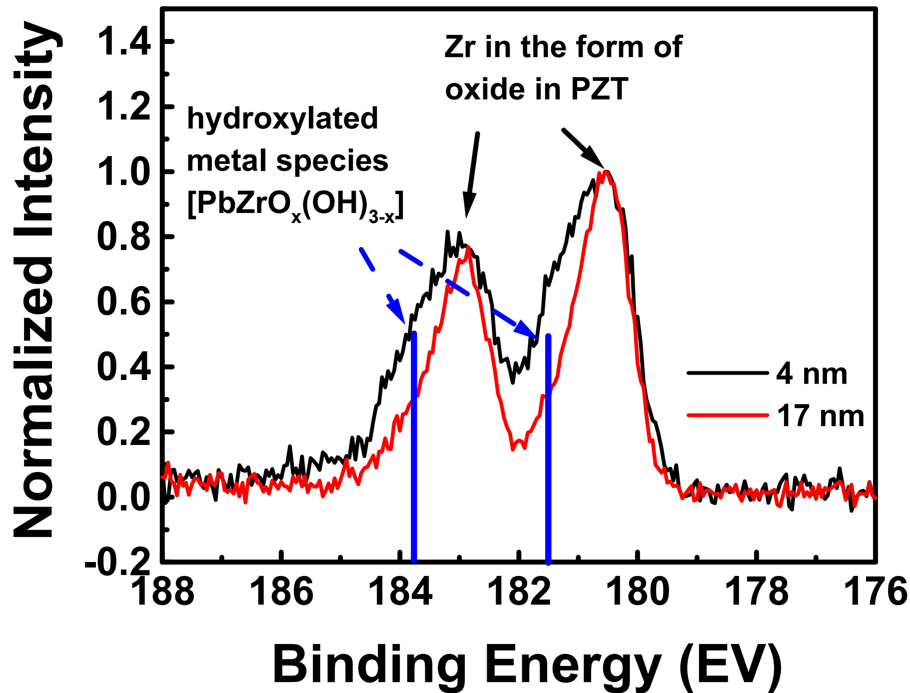

Figure 4-15. XPS spectrum of Zr 3d peak (Zr atoms present in the form of an oxide in PZT and hydroxylated metal species, probably of the form $PbZrO_x(OH)_{3-x}$).

Contrary to the peak width changes in Zr, the same peak shape and width from even for top layers were obtained from Pb. Now, the scaling behavior of MOCVD-PZT films can be interpreted with XPS results. As discussed in previous chapter, polarization and piezoelectric properties are the function of composition of Zr to Ti while the stoichiometric composition for perovskite is governed by the composition of Pb. This leads to the observation of piezoresponse in 4 nm thick films but small deviation in scaling behavior with order parameters which was calibrated with 34 nm thick $Pb(Zr_{0.2}Ti_{0.8})O_3$ films. This observation of clear difference of peak widths in Zr was not found in PLD-PZT samples (it was insignificant even there exists wider peak width in ~4 nm). However, further experiments to identify the bonding states for these observations are needed.

4.4 Disccussion

In summary of this chapter, ultra-thin PZT films have been prepared by liquid delivery MOCVD. The effect of reduced thickness on ferroelectricity in thin PZT films was studied by comparing the magnitude of the piezoresponse signal as measured by PFM with the quantitatively determined order parameters. It is found that the films as thin as 8–10 unit cell thick PZT films shows a measurable piezoelectric response.

It was found that the instability of surface chemical bonding state in ultra thin films found in XPS results may affect the scaling behavior obtained from MOCVD-PZT films. The formation of hydroxylated metal species is related to the activation

energy to form stable oxide phase and could be controlled by controlling the process parameters. However, chemical reaction control to suppress hydroxylated metal species is not clearly understood in this study. To carefully investigate chemistry and reaction mechanism in PZT thin film process, an *in-situ* diagnostic method such as FTIR or mass spectrometry can provide some more insights into the basic science of CVD process. Clearly careful analysis is required to clarify these observations.

Chapter 5: $BiFeO_3$ thin film growth by MOCVD

5.1 Background

There is currently significant interest in the field of ferroelectric thin film materials and devices, with a strong focus on the integration of thin films on Si-complementary metal-oxide semiconductor (CMOS) for non-volatile memory (FeRAM) applications. Two ferroelectric perovskites, namely the lead zirconate titanate (PZT) and strontium bismuth tantalite (SBT) family of materials have emerged as the most attractive candidates for the storage capacitor layer. Although considerable progress towards integration is being made, there are some key questions that are pertinent to these materials systems. The optimum processing temperatures are still quite high for the SBT system, although the recent progress in reducing the temperature is very encouraging[112, 113]; in the case of the PZT system, the inherent toxicity of lead is of great environmental concerns.

Therefore, it is quite desirable to have a ferroelectric material system that has the large polarization properties and low temperature processability of the PZT system with the chemical "benign-ness" of the SBT system.

In this regard, recently it has been reported that a significant ferroelectric polarization was observed in epitaxial thin films of the lead-free perovskite, bismuth ferrite (BFO)[114, 115], which was also observed by the studies of Yun and co-workers[116]. A perovskite BFO has high Curie temperature (850 ^{o}C)[117, 118] and

possesses a rhombohedrally distorted perovskite structure with space group $R3c - C^3_{v6}$ in the bulk[119]. It has been reported that bulk BFO showed a polarization of 3.5 μC/cm^2 along (001) at 70 K, indicating a polarization of 6.1 μC/cm^2 along (111)[120]. The unit cell parameters of rhombohedral and pseudocubic are a = 5.616 Å, and a = 3.96 Å, respectively.

It was found that bismuth ferrite could typically exist three different stable phases, i.e., $Bi_{25}FeO_{40}$, $BiFeO_3$, and $Bi_2Fe_4O_9$, as shown in Bi_2O_3 - Fe_2O_3 phase diagram (Figure 5-1)[121]. Therefore, careful analyses on the composition and the crystal structure must be performed to identify the phase of samples.

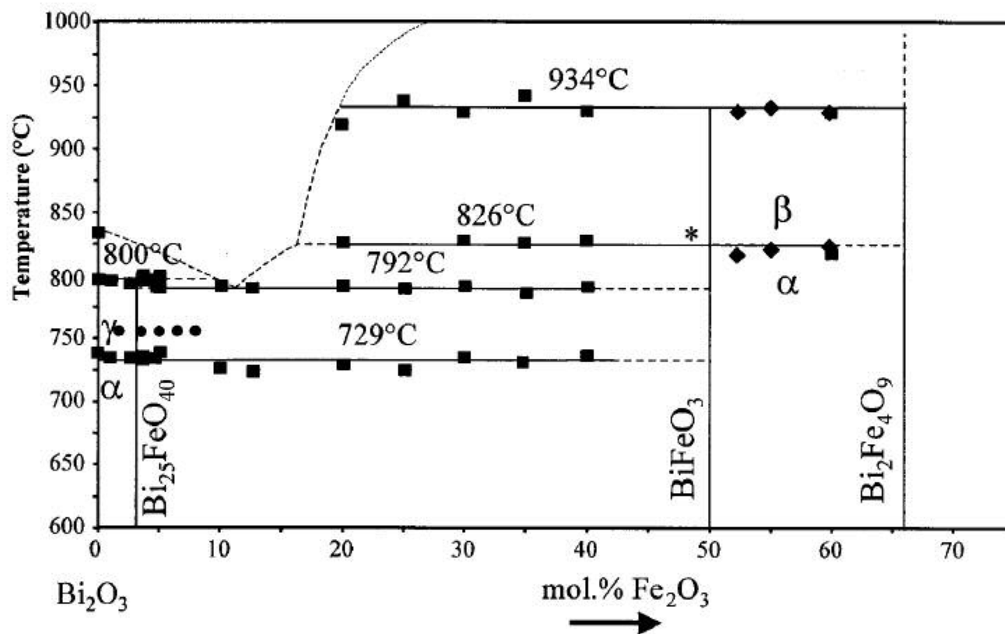

Figure 5-1. Bi_2O_3 - Fe_2O_3 phase diagram.

In the process of exploring the viability of using this materials system as an alternative ferroelectric system that embodies the positive attributes of both the PZT and SBT systems into a FRAM memory process flow, it is imperative that a viable, manufacturable process (such as a chemical vapor deposition) be available for the deposition of the ferroelectric layer. In this chapter, the precursor chemistry, the process window as well as the ferroelectric and piezoelectric properties of films deposited on single crystal (001) $SrTiO_3$ (STO) and STO / Si covered with an $SrRuO_3$ (SRO) electrode layer will be described.

5.2 Growth conditions

An MOCVD equipped with liquid delivery system (LDS) was used with Tris(2,2,6,6-tetramethyl-3,5-heptanedionate)bismuth (III) [$Bi(thd)_3$] and Tris(2,2,6,6-tetramethyl-3,5-heptanedionate)iron (III) [$Fe(thd)_3$] dissolved in tetrahydrofuran (THF) which are both based on β-diketonates as the liquid metalorganic precursor materials. Their intrinsic similarity in organometallic chemistry makes them reasonably compatible and the thermogravimetric (TG) curves of $Bi(thd)_3$ and $Fe(thd)_3$ are shown in Figure 5-2. As indicated in TG analysis, $Bi(thd)_3$ shows the imperfect vaporization property leaving ~30 % residue even at 350 ^{o}C. The vaporizer was clogged after about 5 hours of operation due to this residue.

An SRO layer was prepared by PLD at 650 ^{o}C as a bottom electrode and the growth condition of MOCVD process is summarized in Table 5-1.

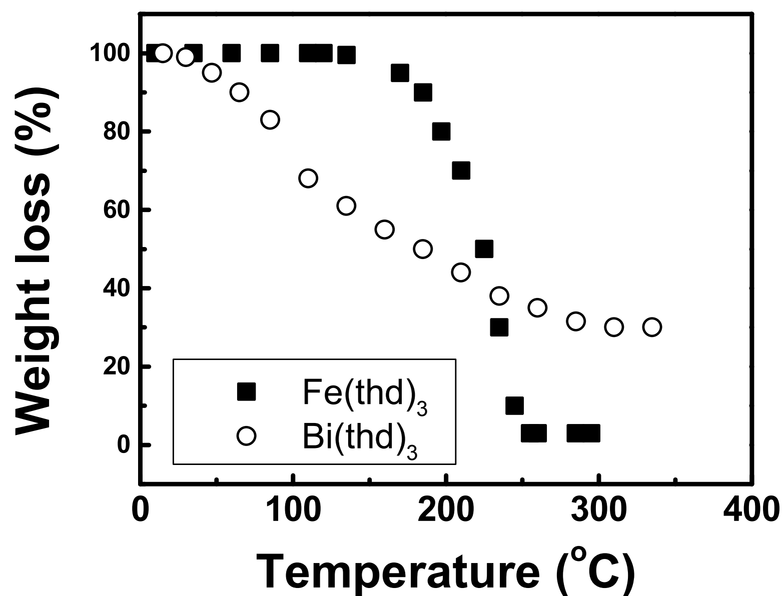

Figure 5-2. The thermogravimetric (TG) curves for $Bi(thd)_3$ and $Fe(thd)_3$.

precursors	$Bi(thd)_3$ $Fe(thd)_3$
Vaporizer temperature	190 - 210 °C
Carrier gas flow rate	200 sccm
O_2 gas flow rate	500 sccm
Substrate temperature	600 – 650 °C
Process pressure	2 Torr
Liquid solution flow rate	0.2 ml/min.

Table 5-1. Deposition parameters of BFO films prepared by liquid delivery MOCVD.

A showerhead that is designed to be heated with oil to avoid condensation of vaporized precursors and achieves high uniform film deposition over a 2 in. substrate was used.

Consistent with previous work on CVD process of PZT thin films, it was found that the film composition and structure are quite sensitive to the substrate temperature, the precursor delivery ratio as well as the vaporizer temperature[122]. The variation of film composition with different precursor supply ratios is shown in Figure 5-3.

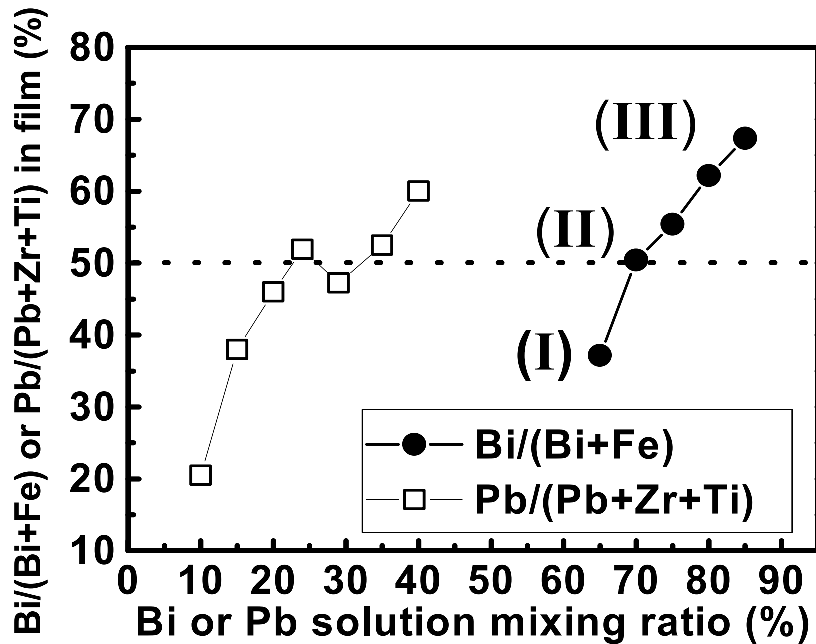

Figure 5-3. Relation between Bi and Fe atomic percentage in $BiFeO_3$ films as measured by Rutherford backscattering (RBS) and energy disperse spectrometry (EDS), for precursor mixing ratio prepared at growth temperature of 650 ^{o}C. Atomic percentage ratio in $Pb(Zr_xTi_{1-x})O_3$ is also plotted at the same scale for comparison.

The volumetric liquid source supply mixing ratio of Bi/(Bi+Fe) was changed from 0.50 to 0.85 and growth temperature was set at 650 ^{o}C. It should be noted that the mixing ratio represents the volumetric ratio of liquid sources at room temperature, and not the actual gas mixing ratio in the reactor. A stoichiometric composition was obtained from a Bi/(Bi+Fe) liquid source mixing ratio of 0.70. The high supply ratio of Bi precursor with respect to Fe precursor required to achieve stoichiometric composition in films can be understood as a consequence of the low vapor pressure of $Bi(thd)_3$ as compared with $Fe(thd)_3$. The vapor pressure of each precursor can be calculated from he empirical vapor pressure *vs.* temperature equations for $Bi(thd)_3$ and $Fe(thd)_3$ [Eqs. (5-1) and (5-2), respectively];

$$Bi(thd)_3;\ \log P = -5202.7/T + 12.4 \quad (5\text{-}1)$$

$$Fe(thd)_3;\ \log P = -4842/T + 12.5 \quad (5\text{-}2)$$

Where, pressure (P) in Pa and temperature (T) is in K.

At temperature of 190 ^{o}C, the vapor pressure of $Fe(thd)_3$ is about 2.5 times higher than that of $Bi(thd)_3$. In addition, $Bi(thd)_3$ is not completely vaporized and leaves ~30 % residue which is not volatile as deduced from thermogravimetric analysis (TGA). The incomplete vaporization of $Bi(thd)_3$ may require the high supply ratio of the Bi precursor. Accordingly, the equivalent amount of vapor can be introduced into the reaction chamber with a Bi/(Bi+Fe) liquid mixing ratio of 0.70. The change of Pb atomic content ratio that is obtained from our previous PZT process

performed at the same growth temperature (650 ^{o}C) is also plotted in Figure 5-3[122]. Here, it should be noted that the growth-window of BFO films appears to be much smaller than that of PZT as can be seen in Figure 5-3. The composition change in the Bi/(Bi+Fe) ratio shows an almost linear behavior with the liquid source mixing ratio, while there is a relatively wide plateau region for the PZT film growth process. This is generally explained by a "Pb self-regulating" mechanism at high temperature growth processes and is used as the growth window[123, 124] as discussed in previous chapter.

5.3 Crystal structure

Crystal structures for different composition films were determined by a typical θ - 2θ x-ray diffraction scan. Only (00*l*) diffraction peaks from BFO, SRO and STO without any second phase were observed for films with the stoichiometric composition [Figure 5-4 (designated as (II))].

The out-of plane lattice parameter calculated from the (002) peak of a 150 nm thick BFO film is 4.03 Å. This value is larger than bulk lattice constant (3.96 Å) because of the in-plane compressive strain induced by the substrate (SRO/STO). However, additional secondary phase peaks such as (024) α-Fe_2O_3 (Rhombohedral, $R\bar{3}c$, a = 5.112 Å, c = 13.82 Å) or (002) and (220) β-Bi_2O_3 (tetragonal, $P\bar{4}2_1c$, a = 7.741 Å, c = 5.634 Å) were observed in Fe- and Bi-rich films (designated as (I) and (III), respectively) in Figure 5-4.

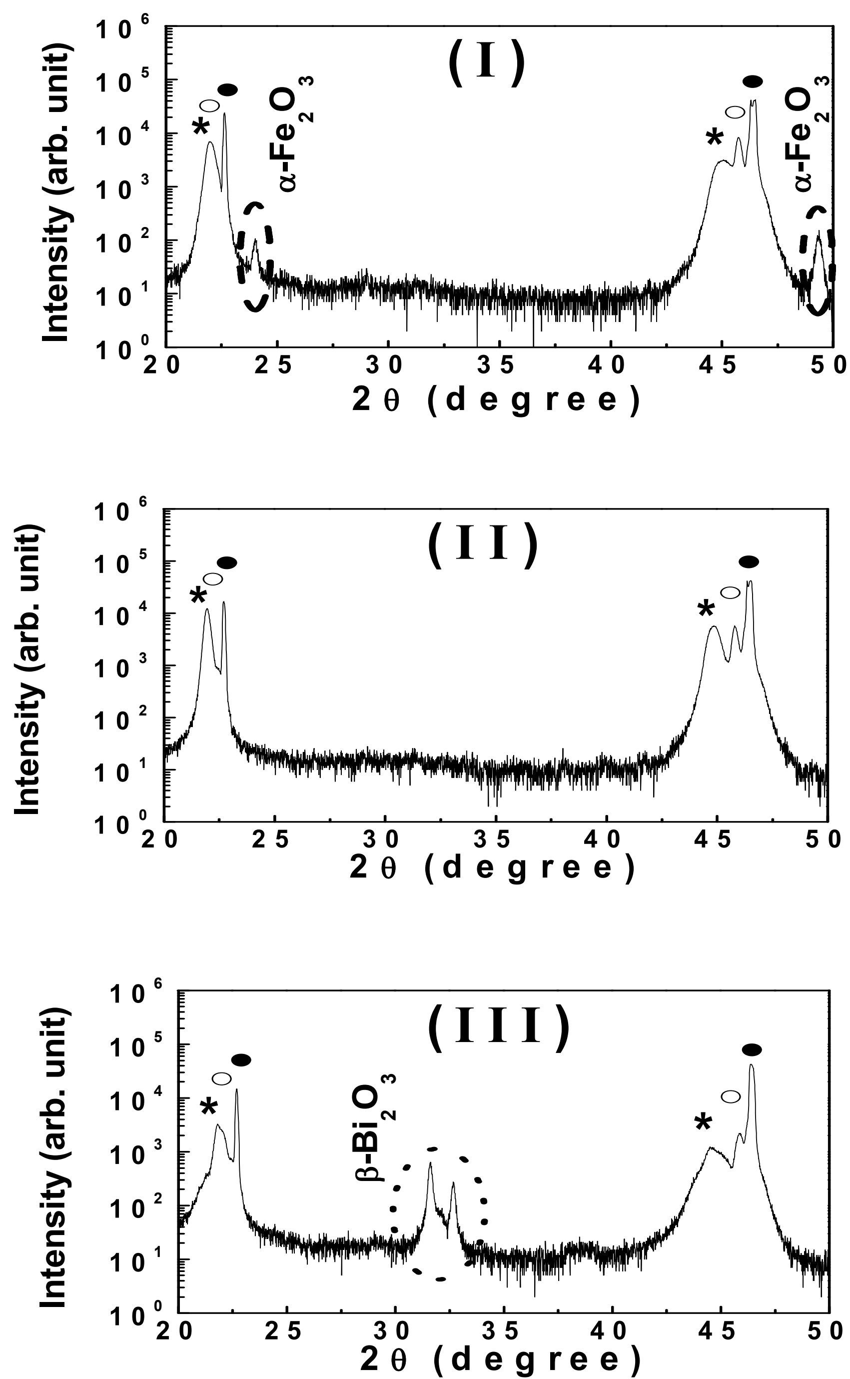

Figure 5-4. θ - 2θ X-ray diffraction scans for (I) Fe-rich phase, (II) stoichiometric composition and (III) Bi-rich phase. * : $BiFeO_3$; ● : $SrRuO_3$; ○ : $SrTiO_3$.

The interface between SRO and BFO, observed in the cross-sectional high-resolution transmission electron microscopy (HR-TEM) image as shown in Figure 5-5, is atomically sharp and coherent.

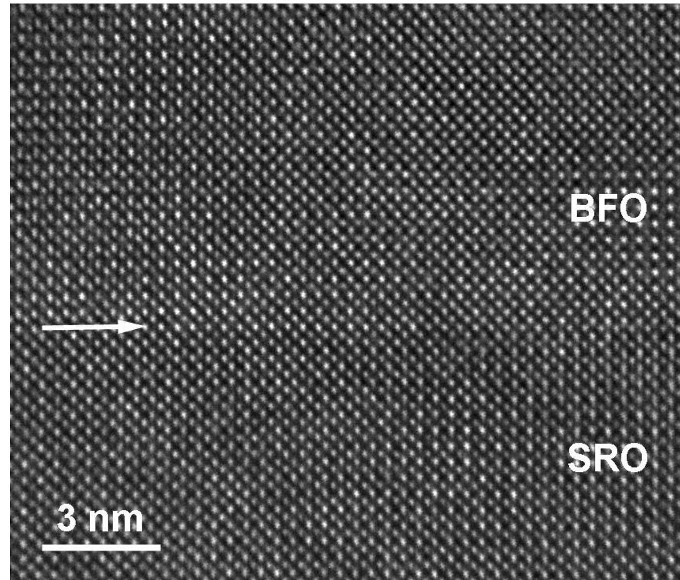

Figure 5-5. Cross-sectional HRTEM image of BFO/SRO interface.

5.4 Surface morphology and Electrical properties

Subsequent to the optimization of the Bi:Fe ratio in the precursors, it was proceeded to grow epitaxial films on single crystalline (001) STO and (001) STO / Si. To facilitate heteroepitaxy and to introduce a conducting perovskite bottom electrode, a 70 nm thick, epitaxial SRO layer deposited by pulsed laser deposition (PLD) was used. For the electrical and electromechanical measurements, circular platinum (Pt)

pads with 32 μm diameter were deposited as top electrodes by a standard lift-off process.

The surface morphologies of BFO films for different compositions measured by atomic force microscopy (AFM) are shown in Figures 5-6 (a), (b) and (c). Out-of-plane piezoelectric response measurements using piezoelectric force microscopy (PFM) were performed to study the piezoelectric properties of these films, and the results are shown in Figures 5-6 (d), (e) and (f).

The films were first poled at a negative dc-bias (-8 V) applied to a conducting probe while scanning over a 2×2 μm^2 area. In the case of stoichiometric films [figure 5-6 (e)], another poling was performed, with the probe biased at the opposite voltage (+8 V) during scanning over a 1×1 μm^2 area inside the previously poled area. Details on the PFM technique can be found elsewhere[125, 126].

A flat surface with 2 nm of peak-to-peak height was observed within the area of 3×3 μm^2 on 250 nm thick film with stoichiometric composition as shown in Figure 5-6 (b). A sharp piezoelectric response with complete reversible switching was also observed as shown in Figure 5-6 (e). In the case of Fe-rich films, a rough, granular surface was observed [Figure 5-6 (a)] and no piezoresponse was detected [Figure 5-6 (d)]. On the other hand, Bi_2O_3 islands were formed on a BFO matrix in the case of Bi-rich films as shown in Figures 5-6 (c) and (f).

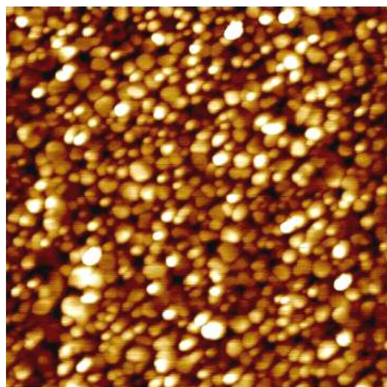

(a) Fe-rich

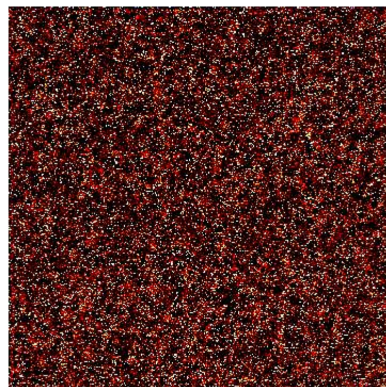

(d) Fe-rich

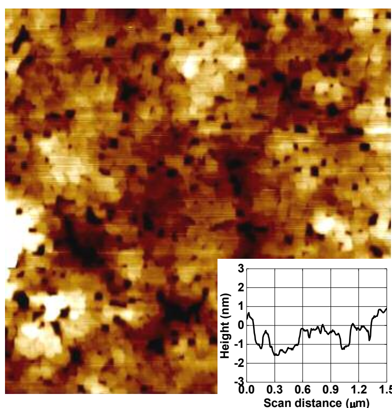

(b) stoichiometric $BiFeO_3$

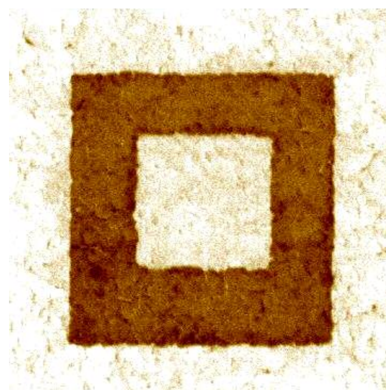

(e) stoichiometric $BiFeO_3$

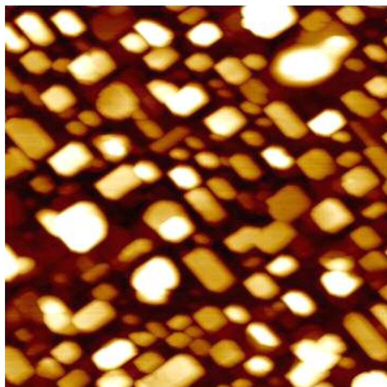

(c) Bi-rich

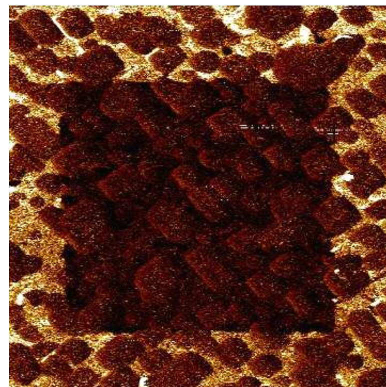

(f) Bi-rich

Figure 5-6. Surface morphologies (a), (b), (c) and out-of-plane piezoelectric response measurements (d), (e), (f) using a piezoelectric force microscopy (PFM). The thickness of films is ~250 nm.

An out-of-plane piezoelectric coefficient, d_{33}, of 50 – 60 pm/V was measured at room temperature, as shown in Figure 5-7 (a). The polarization-electric field (*P*-*E*) hysteresis loops measured at 16 kHz on the 250 nm thick BFO film are shown in Figure 5-7 (b). The sharp and square loops yield a $2P_r$ value of 110 - 120 μC/cm^2. This value is comparable to the theoretically predicted and experimentally obtained values from PLD-grown films[114, 127].

In order to extract the real switched polarization properties, PUND measurements (ΔP = P^* (switched polarization) - $P^\wedge$ (non-switched polarization)) were also performed to confirm these values and the result is shown in Figure 5-7 (c). The obtained switched polarization (ΔP) is 110 - 120 μC/cm^2 which is consistent with the $2P_r$ value from the *P*-*E* hysteresis loop.

The electric field dependence of polarization with the results obtained for BFO films grown by PLD and sputtering[125] were compared. These three films prepared by different growth methods showed very similar behavior. In all the cases, switched polarization values of ~120 μC/cm^2 were observed, which began to saturate at 400 – 450 kV/cm. Moreover, the polarization showed weak pulse width dependence in the range of 1 μsec - 1 msec, as shown in Figure 5-7 (d). This demonstrates that the measured polarization switching is an intrinsic property of BFO films, and is not dominated by leakage, which was a critical obstacle in determining the ferroelectric property of bulk BFO[120].

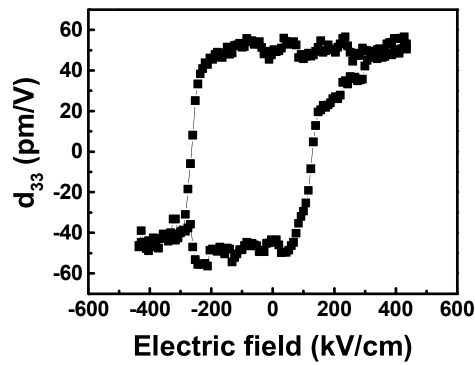

(a)

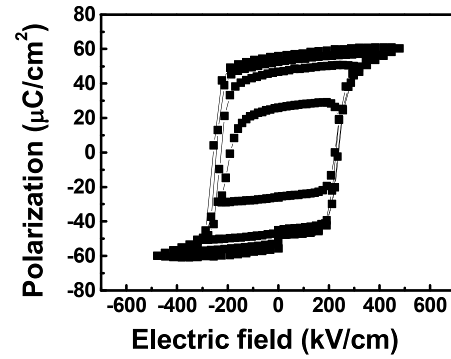

(b)

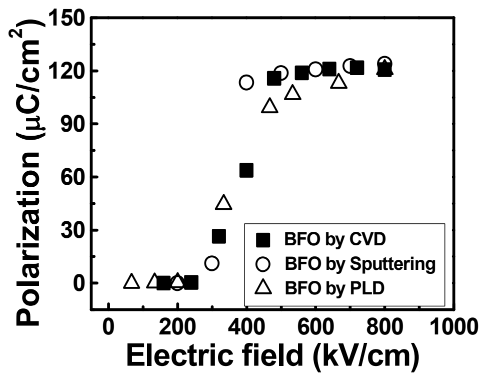

(c)

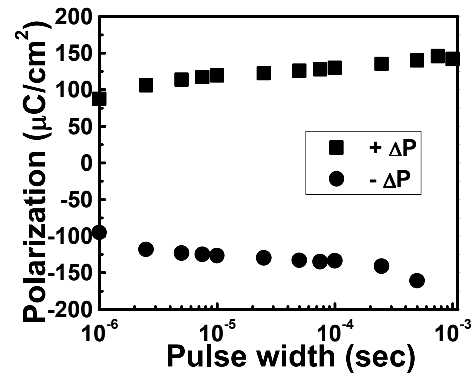

(d)

Figure 5-7 (a) Piezoelectric coefficients, d_{33}, loop as a function of applied voltage from 250 nm thick BFO film. (b) *P*-*E* hysteresis loops as a function of applied voltage from 250 nm thick BFO film measured at frequency of 20 kHz. (c) Pulsed polarization (*ΔP*) as a function of applied voltage at frequency of 20 kHz. (d) Pulse-width dependence of switched polarization (*ΔP*) in the range from 1μsec. to 1 msec. at 15 V.

BFO films were also prepared on (001) Si using a 20 nm thick STO layer as a template, and their properties were compared with those of films grown on STO substrates.

Figure 5-8 shows *P-E* loops of BFO films grown on such substrates. Polarization values (ΔP) of 85 – 90 μC/cm^2 and coercive fields of ~ 225 kV/cm were measured for BFO films grown on Si substrate. These values are smaller than those obtained for BFO films grown on STO, due to the in-plane tensile stress induced by large thermal mismatch with silicon[115]. Out-of-plane lattice constants of 4 Å and 3.96 Å were observed for BFO films (200 nm) grown on STO and Si substrates, respectively.

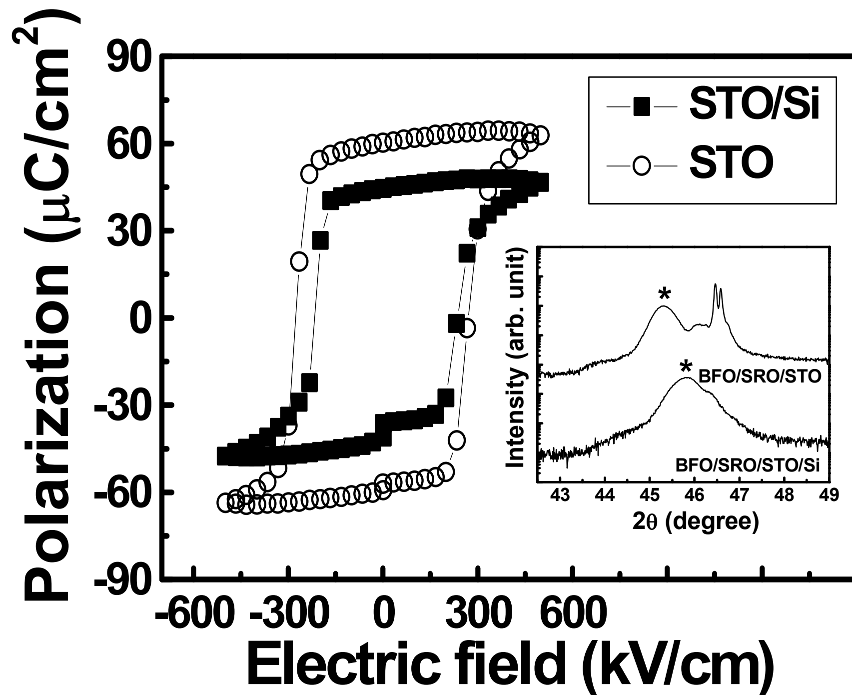

Figure 5-8. *P-E* hysteresis loops obtained from BFO films on SRO / STO and SRO / STO / Si substrates. XRD patterns around (002) BFO peaks are shown in inset.

5.5 Discussion

It has been demonstrated that a viable chemical vapor deposition process enables the growth of high quality $BiFeO_3$ thin films in this chapter. The implementation of such a process into the potential FeRAM technology requires the solution for some key issues.

First, the leakage current must be lowered by at least an order of magnitude. This requires a careful study of the defect chemistry of the films as a function of Bi-Fe ratio as well as other process parameters such as the substrate temperature and oxygen ambient during cooling.

Second, the coercive field must be reduced to ~ 50 kV/cm (e.g., 1 V for a 200 nm thick film). Ferroelectric properties of BFO and PZT films are shown in Figure 5-9. These figures clearly show the direction of the future study. Even though BFO film shows the comparable polarization value, it has about 2-3 times higher coercive field than that of PZT (20 / 80) film.

Lowering the coercive field of BFO film is a key question needs to be solved for the realization of device applications. Careful studies of the switching mechanisms in these films (180° versus $71/109^{o}$ switching, and the interplay between ferroelectric and ferroelastic switching[125, 128]) are needed.

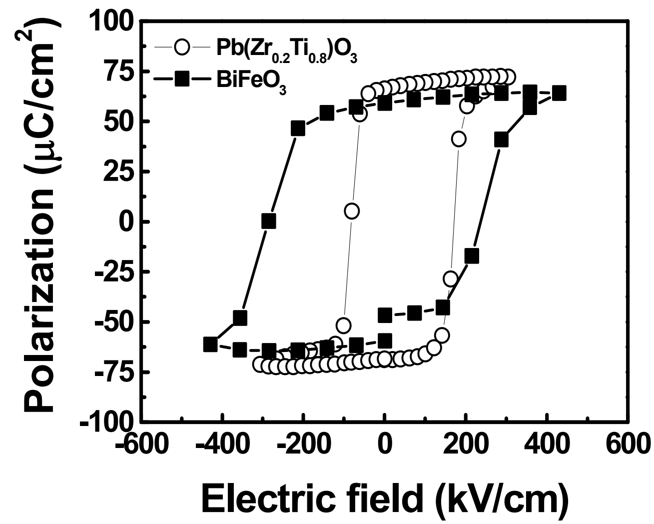

(a)

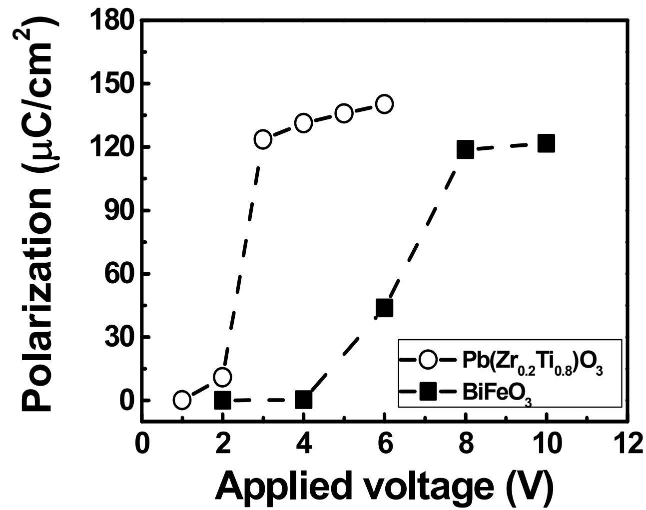

(b)

Figure 5-9. Comparison of (a) *P*-*E* hysteresis loops and (b) coercive fields dependence obtained from BFO and PZT films on SRO / STO.

Third, the growth temperature must be reduced. Preliminary studies indicate that this should be possible, in agreement with the reports of Yun *et al*.[116]. From the CVD chemistry point of view, it is critical to explore the processing space to identify the possibility of a "self-regulating" reaction zone. In this regard, preliminary results show that a post-deposition oxygen flush of the film surface appear to hold promise in terms of removing the excess Bi on the surface.

Chapter 6: Summary and future work

In this dissertation, a systematic study of the process controls as well as the ferroelectric and piezoelectric properties of two ferroelectric material systems, lead zirconate titanate (PZT) and bismuth ferrite (BFO), prepared by MOCVD has been carried out. In order to feasibly control the precursor partial pressure and flow rate a liquid delivery system (LDS) was equipped to MOCVD chamber. Precursors based on β-diketonate were used for thin film growth and the characteristics of deposited films showed crucial dependence on deposition temperature, deposition environment, and kinetic factors such as the precursor partial pressure and flow rate.

In PZT system, the changes of spontaneous polarization (P_s) and piezoelectric coefficient (d_{33}) with Ti/(Zr+Ti) ratio are presented and compared with theoretical values. Ferroelectric and piezoelectric properties at the composition close to morphotropic phase boundary (MPB) region ($Pb(Zr_{0.5}Ti_{0.5})O_3$) have been investigated for application in nonvolatile ferroelectric random access memories (FeRAM) and microelectromechanical system (MEMS). These capacitors show desirable ferroelectric properties such as high polarization and small coercive field, which proves that this approach is very promising for both fundamental study and potential applications.

The scaling of ferroelectric properties with film thickness in $Pb(Zr_{0.2}Ti_{0.8})O_3$ films grown on $SrRuO_3/SrTiO_3(001)$ was studied. The PZT films are single crystalline, *c*-oriented, and showed bulk-like properties for thickness above ~20nm. Piezoelectric force microscopy (PFM) was employed to investigate the ferroelectric

properties of films thinner than 20 nm. Piezoelectric response was observed down to a film thickness of 8 – 10 unit cells. A quantitative analysis of the size effect in $Pb(Zr_{0.2}Ti_{0.8})O_3$ films was performed using the piezoelectric response. From the high resolution XPS analysis, it was found that a hydroxylated metal species were formed on a top few layers. This imperfect chemical state induced by unstable chemical reaction in MOCVD process can be the main factor for the deviation in determining the ferroelectric scaling in ultra thin films (thinner than 10 unit-cells).

Epitaxial $BiFeO_3$ thin films were grown by MOCVD using $Bi(thd)_3$ and $Fe(thd)_3$ as precursors. This research was the first challenge to prepare this material system by MOCVD process. A systematic study on deposition process control such as stoichiometric composition, structure change and growth temperature was carried out. The film composition and phase equilibrium are sensitive to the Bi:Fe ratio in the precursor. In the optimized growth condition which is very small growth window, high quality epitaxial single perovskite phase thin films were obtained. Electrical measurements using both quasi-static hysteresis and pulsed polarization measurements confirm the existence of ferroelectricity with a switched polarization of 110-120 $\mu C/cm^2$, ΔP (= P^* - $P^\wedge$). Out-of plane piezoelectric (d_{33}) measurements using an atomic force microscope yield a value of 50 – 55 pm/V. These values are comparable to the theoretically predicted and experimentally obtained values from PLD-grown films.

Further research will be performed on both material systems (PZT and BFO) which has not been completely understood in this study.

1) A careful quantitative analysis of the effect of hydroxylated metal species on the thickness effect on the ferroelectric properties can extract the real thickness effect of PZT films prepared by MOCVD. This study needs precise computing simulation of XPS results and careful analysis on the structure in ultra thin films.

2) A perovskite $BiFeO_3$ system could be a promising alternative ferroelectric material for the current most popular PZT system due to its large ferroelectric polarization and environmentally favorable nature. This makes it an interesting replacement candidate for Pb-based ferro/piezoelectrics. However, $BiFeO_3$ has about 3 times higher coercive field than that of PZT film and lowering the coercive field of $BiFeO_3$ film is a key question needs to be solved for the realization of device applications as discussed in Chapter 5. One of the possible approaches is by doping $BiFeO_3$ with other elements, e.g. lanthanum.[129,130,131] This design is inspired from lowering the Curie temperature or tailoring the domain switching mechanism by doping with lanthanum.[132] The spontaneous polarization and coercive field are expected to be lowered by reducing the distortion of the structure.

3) As indicated in Chapter 5, the growth window for $BiFeO_3$ film is very small in MOCVD process and secondary phase is prone to form which is also applicable in pulsed laser deposition.[133] A relatively wide "self-regulating" growth window with stoichiometric composition is very attractive aspect in the growth process. This can lead to the availability of large-scale wafer process and greater process flexibility. In order to verify the existence of "self-regulating" growth

mechanism in $BiFeO_3$ system, the following directions can be considered for further research.

i) The effect of growth temperature.

ii) The effect of oxygen partial pressure.

iii) Growth process control such as cooling rate and cooling in oxygen atmosphere.

REFERENCES

[1] J. Valasek, Phys. Rev. **15** (6), 537 (1920); **17** (4), 475 (1921).

[2] D. W. Chapman, J. Appl. Phys. **40**, 2381 (1969).

[3] R. B. Atkin, Ferroelectrics **3**, 213 (1972).

[4] M. Francombe, Ferroelectrics **3**, 199 (1972).

[5] P. M. Heyman and G. H. Heilmeier, Proc. IEEE **54**, 842 (1966).

[6] S. Mathews, R. Ramesh, T. Venkatesan, J. Benedetto, Science **276**, 238 (1997).

[7] J. F. Scott and C. A. Paz de Arauzo, Science **246**, 1400 (1989).

[8] A. Mannish, Ferroelectrics **102**, 69 (1990).

[9] B. Jaffe, W. R. Cook, and H. Jaffe, "Piezoelectric Ceramics", Academic Press (1971).

[10] M. E. Linesand A. M. Glass, Priciples and applications of Ferroelectrics and Related Materials (Oxford University Press, Oxford, 1997).

[11] M. J. Haun, E. Furman, S. J. Jang, and L. E. Cross, Ferroelectrics **99**, 45 (1989).

[12] Fujitsu's FRAM technology solution, "What's new about FRAM", **20** (2002).

[13] A. Erbil, W. Braun, B. S. Kwak, B. J. Wilkens, L. A. Boatner and J. D. Budai, J. Crystal Growth **124**, 684 (1992).

[14] D. L. Schulz and T. J. Marks, Adv. Mater., **6**, 719 (1994).

[15] Toshio Hirai and Hisanori Yamane, J. Crystal Growth **107**, 683 (1991).

[16] K. Endo, H. Yamasaki, S. Misawa, S. Yoshida, and K. Kajimura, Nature **355**, 327 (1992).

[17] Mikko Ritala, Kaupo Kukli, Antti Rahtu, Petri I. Raisanen, Markku Leskela, Timo Sajavaara, Juhani Keinonen, Science **288**, 319 (2000).

[18] Anthony C. Jones, Chem. Vap. Deposition **4**, 169 (1998).

[19] Hiroshi Funakubo, Tsuyoshi Hioki, Masato Otsu, Kazuo Shinozaki and Nobuyasu Mizutani Jpn. J. Appl. Phys. **32**, 4175 (1993).

[20] A. C. Jones, P. A. Williams, P. R. Chalker, S. Taylor, A. Zoolfakr, L. M. Smith, P. McGraw, Integr. Ferroelectr. 57, 1271 (2003).

[21] K. J. Hubbard and D. G. Schlom, J. Mater. Res. **11**, 2757 (1996).

[22]T. Nakagawa, J. Yamaguchi, M. Okuyama and Y. Hamakawa, Jpn. J. Appl. Phys. **21**, L655 (1982).

[23] M. Okada, K. Tominaga, T. Araki, S. Katayama and T.Sakashita, Jpn. J. Appl.Phys. **29**, 718 (1990).

[24] Yukio Sakashita, Hideo Segawa, Kouji Tominaga, and Masaru Okada, J. Appl. Phys. **76**, 2405 (1994).

[25] P. K. Larsen, G. J. M. Dormans, D. J. Taylor and P. J. Van Veldhoven, J. Appl. Phys. **73**, 7857 (1993).

[26] M. De Keijser, J. F. M. Cillessen, R. B. F. Janssen, A. E. M. De Veirman and D. M. de Leeuw, J. Appl. Phys. **79**, 393 (1996).

[27] C. M. Foster, G.-R. Bai, R. Csencsits, J. Vetrone, R. Jammy, L. A. Wills, E. Carr, and Jun Amano, J. Appl. Phys. **81**, 2349 (1997).

[28] Hiroshi Funakubo,a) Masanori Aratani, Takahiro Oikawa, Kouji Tokita, and Keisuke Saito, Appl. Phys. Lett. **92**, 6768 (2002).

[29] Hajime Nonomura, Hironori Fujisawa, Masaru Shimizu and Hirohiko Niu, Jpn. J. Appl.Phys. **41**, 6682 (2002).

[30] Vladislav V. Krisyuk, Aciya E. Turgambaeva, and Igor K. Igumenov, Chem. Vap. Deposition, **4**. 43 (1998).

[31] K. Nagashima, H. Funakubo, S. Seki, Y. Sawada, Y. Miura, N. Higuchi, and H. Matchida, Chem. Vap. Deposition. **6**, 311 (2000).

[32] J. F. Roeder, T. H. Baum, S. M. Bilodeau, G. T. Stauf, C. Ragaglia, M. W. Russell, and P. C. Van Buskirk, Adv. Mater. Opt. Electron. **10**, 145 (2000).

[33] H. K. Ryu, J. S. Heo, S. I. Cho, and S. H. Moon, J. Electrochem. Soc. **146**, 1117 (1999).

[34] R. Ramesh, S. Aggarwal, and O. Auciello, Materials Science and Engineering R, **32**, 191 (2001).

[35] D. L. Schultz, T. J. Marks, Adv. Mater. **6**, 719 (1994).

[36] T. J. Marks, Pure Appl. Chem. **67**, 313, (1995).

[37] Introduction to Solid State Physics, C. Kittel, (1976).

[38] A. L. Roytburd, S. P. Alpay, V. Nagarajan, C. S. Ganpule, S. Aggarwal, E. D. Williams, and R. Ramesh, Phys. Rev. Lett. **85**, 190 (2000).

[39] M. D. Glinchuk, E. A. Eliseev, and V. A. Stephanovich, Physica B **322**, 356 (2002).

[40] J. Junquera and P. Ghosez, Nature **422**, 506 (2003).

[41] I. P. Batra, P. Wurfel, and B. D. Silverman, J. Vac. Sci. Technol. **10**, 687 (1973).

[42] R. R. Mehta, B. D. Silverman, and J. T. Jacobs, J. Appl. Phys. **44**, 3379 (1973).

[43] Y. Sotome, J. Senjaki, S. Morita, S. Tanimoto, T. Hirai, T. Ueno, K. Kuroiwa, and Y. Tarui, Jpn. J. Appl. Phys. **33**, 4066 (1994).

[44] T. Y. Kim, D. Kim, and C. W. Chung, Jpn. J. Appl. Phys. **36**, 6494 (1997).

[45] C. M. Foster, G.-R. Bai, R. Csencsits, J. Vetrone, R. Jammy, L. A. Wills, E. Carr, and Jun Amano, J. Appl. Phys. **81**, 2349 (1997).

[46] H. Fujisawa, M. Yoshida, M. Shimizu and Hirohiko Niu, Jpn. J. Appl. Phys. **37**, 5132 (1998).

[47] I. S. Chen, B. C. Hendrix, S. M. Bilodeau, Z. Wang, C. Xu, S. Johnston, P. C. Van Buskirk, T. H. Baum and J. F. Roeder, Jpn. J. Appl. Phys. **41**, 6695 (2002).

[48] H. Yamazaki, T. Tsuyama, I. Kobayashi, and Y. Sugimori, Jpn. J. Appl. Phys. **31**, 2995 (1992).

[49] G. Asano, T. Oikawa and H. Funakubo, Jpn. J. Appl. Phys. **42**, 2801 (2003).

[50] K. Tokita, M. Aratani, and H. Funakubo, Appl. Phys. Lett. **82**, 4122 (2003).

[51] H. K. Ryu, J. S. Heo, S. I. Cho, and S. H. Moon, J. Electrochem. Soc. **146**, 1117 (1999).

[52] A. C. Jones, Chem. Vap. Deposition, **4**, 169 (1998).

[53] H. M. Duiker, P. D. Beale, J. F. Scott, C. A. Paz de Araujo, B. M. Melnick, J. D. Cuchiaro, and L. D. McMillan, J. Appl. Phys. **68**, 5783 (1990).

[54] I. E Scott, C. A. Araujo, B. M. Melnick, L. D. McMillan, and R. Zuleeg, J. Appl. Phys. **70**, 382 (1991).

[55] H. N. Al-Shareef, K. R. Bellur, 0. Auciello, and A. I. Kingon, Proceedings of 5th International Symposium on Integrated Ferroelectrics, Colorado Springs, CO, 1994.

[56] K. Maki, B. T. Liu, H. Vu, V. Nagarajan, R. Ramesh, Y. Fujimori, T. Nakamura, and H. Takasu, Appl. Phys. Lett. **82**, 1263 (2003).

[57] R. Ramesh, H. Gilchrist, T. Sands, V. G. Keramidas, R. Haakenaasen, and D. K. Fork, Appl. Phys. Lett. **63**, 3592 (1993).

[58] C. B. Eom, R. B. Van Dover, Julia M. Phillips, D. J. Werder, J. H. Marshall, C. H. Chen, R. J. Cava, R. M. Fleming, and D. K. Fork, Appl. Phys. Lett. **63**, 2570 (1993).

[59] http://superconductivity.et.anl.gov/Techniques/PLD.html

[60] R. Ramesh, S. Aggarwal, and O. Auciello, Materials Science and Engineering R, **32**, 191 (2001).

[61] O. Auciello, J. F. Scott and R. Ramesh, Physics Today, **22** (1998).

[62] S. Aggarwal, A. M. Dhote, H. Li, S. Ankem, and R. Ramesh, Appl. Phys. Lett. **74**, 230 (1999).

[63] H. N. Al-Sharreef, B. A. Tuttle, W. L. Warren, D. Dimos, M. V. Raymond, Appl. Phys. Lett. **68**, 272 (1996).

[64] B. T. Liu, Z. Hao, Y. F. Chen, B. Xu, H. Chen, F. Wu and B. R. Zhao, Yu. Kislinskii, E. Stepantsov, Appl. Phys. Lett. **74**, 2044 (1999).

[65] T. Wu, S. B. Ogale, J. E. Garrison, B. Nagaraj, Amlan Biswas, Z. Chen, R. L. Greene, R. Ramesh, and T. Venkatesan, Phys. Rev. Lett. **86**, 5998 (2001).

[66] Ing-Shin Chen, Jeffrey F. Roeder, Dong-Joo Kim, Jon-Paul Maria, and Angus I. Kingon, J. Vac. Sci. Technol. B, **19**,1833 (2001).

[67] S. A. Impey, Z. Huang, A. Patel, R. Beanland, N. M. Shorrocks, R. Watton, R. Watton, R. W. Whatmore, J. Appl. Phys. **83**, 2202 (1998).

[68] T. Yamaguti, Proc. Phys. Math. Soc. Jpn. **17**, 443 (1935).

[69] R. Sato, J. Phys. Soc. Jpn. **6**, 527 (1951).

[70] M. Ihara, Y. Arimoto, M. Jifuku, T. Kimura, S. Kodama, H. Yamawaki, and T. Yamaoka, J. Electrochem. Soc. **129**, 2569 (1982).

[71] S. Matsubara, N. Shohata, and M. Mikami, Jpn. J. Appl. Phys., Suppl. **24**,10 (1985).

[72] R. A. McKee, F. J. Walker, and M. F. Chisholm, Phys. Rev. Lett. **81**, 3014 (1998).

[73] A. Lin, X. Hong, V. Wood, A. A. Verevkin, C. H. Ahn, R. A. Mckee, F. Walker, and E. D. Specht, Appl. Phys. Lett. **78**, 2034 (2001).

[74] K. Eisenbeiser, J. M. Finder, Z. Yu, J. Ramdani, J. A. Curless, J. A. Hallmark, R. Droopad, W. J. Ooms, L. Salem, S. Bradshaw, and C. D. Overgaard, Appl. Phys. Lett. **76**, 1324 (2000).

[75] Y. Wang, C. Ganpule, B. T. Liu, H. Li, K. Mori, B. Hill, M. Wuttig, R. Ramesh, J. Finder, Z. Yu, R. Droopad, and K. Eisenbeiser, Appl. Phys. Lett. **80**, 97 (2000).

[76] M. De Keijser, P. J. Van Veldhoven and G. J. M. Dormans, Mat. Res. Soc. Symp. Proc. **310**, 223 (1993).

[77] M. V. Ramana Murty, S. K. Streiffer, G. B. Stephenson, J. A. Eastman, G. R. Bai, A. Munkholm, and O. Auciello, Appl. Phys. Lett. **80**, 1809 (2002).

[78] S. R. Gilbert, S. Hunter, D. Ritchey, C. Chi, D. V. Taylor, J. Amano, S. Aggarwal, T. S. Moise, T. Sakoda, S. R. Summerfelt, K. K. Singh, C. Kazemi, D. Carl, and B. Bierman, J. Appl. Phys. **73**, 1713 (2003).

[79] P. K. Larsen, G. J. M. Dormans, D. J. Taylor and P. J. Van Veldhoven, J. Appl. Phys. **76**, 2405 (1994).

[80] A. H. Carim, B. A. Tuttle, D. H. Doughty, and S. L. Martinez, J. Am. Ceram. Soc. **74**, 1455 (1991).

[81] R. Ramesh, W. K. Chan, B. Wilkens, H. Gilchrist, T. Sands, J. M. Tarascon, V. G. Keramidas, D. K. Fork, J. Lee, and A. Safari, Appl. Phys. Lett. **61**, 1537 (1992).

[82] P. Muralt, J. Micromech. Microeng. **10**, 136 (2000).

[83] C. S. Ganpule, A. Stanishevsky, Q. Su, S. Aggarwal, J. Mengailis, E. Williams, and R. Ramesh, Appl. Phys. Lett. **75**, 4091 (1999).

[84] Dennis L. Polla, Lorraine F. Francis, Annu. Rev. Mater. Sci. **28**, 563 (1998).

[85] V. Nagarajan, A. Stanishevsky, L. Chen, T. Zhao, B. T. Liu, J. Melngailis, A. L. Roytburd, and R. Ramesh, Appl. Phys. Lett. **81**, 4215 (2002).

[86] M. J. Haun, E. Furman, S. J. Jang, and L. E. Cross, Ferroelectrics **99**, 45 (1989).

[87] A. F. Devonshire, Philos. Mag. **42**, 1065 (1951).

[88] K. Lefki and G. J. M. Dormans, J. Appl. Phys. **76**, 1764 (1994).

[89] V. Nagarajan, S. Praserchoung, T. Zhao, H. Zheng, J. Ouyang, R. Ramesh, W. Tian, X. Q. Pan, D. M. Kim, C. B. Eom, H. Kohlstedt and R. Waser, Appl. Phys. Lett. **84**, 5225 (2004).

[90] C. H. Lin, P. A. Friddle, C. H. Ma, A. Daga, and Haydn Chen, J. Appl. Phys. **90**, 1509 (2001).

[91] S. Horii, S. Yokoyama, H. Nakajima and S. Horita, Jpn. J. Appl. Phys. **38**, 5378 (1999).

[92] P. K. Larsen, G. J. M. Dormans, D. J. Taylor and P. J. van Veldhoven, J. Appl. Phys. **76**, 2405 (1994).

[93] N. Yanase, K. Abe, N. Fukushima and T. Kawakubo, Jpn. J. Appl. Phys. **38**, 5305 (1999).

[94] J. Junquera and P. Ghosez, Nature, **422**, 506 (2003).

[95] Y. S. Kim, D. H. Kim, J. D. Kim, Y. J. Chang, T. W. Noh, J. H. Kong, K. Char, Y. D. Park, S. D. Bu, J.-G. Yoon, J.-S. Chung, Appl. Phys. Lett. **86**, 102907 (2005).

[96] J. Rodriguez Contreras, H. Kohlstedt, U. Poppe, R. waser, Ch. Buchal, Appl. Phys. Lett. **83**, 126 (2003).

[97] H. Nonomura, H. Fusisawa, M. Shimizu, and H. Niu, Jpn. J. Appl. Phys. 41, 6682 (2002).

[98] Y. Sakashita, H. Segawa, K. Tominaga and M. Okada, J. Appl. Phys. **73**, 7857 (1993).

[99] H. Morioka, G. Asano, T. Oikawa, H. Funakubo, and K. Saito, Appl. Phys. Lett. **82**, 4761 (2003).

[100] D. D. Fong, G. B. Stephenson, S. K. Streiffer, J. A. Eastman, O. Auciello, P. H. Fuoss, and C. Thompson, Science, **304**, 1650 (2004).

[101] T. Tybell, C. H. Ahn and J. –M. Triscone, Appl. Phys. Lett. **75**, 856 (1999).

[102] C. H. Ahn, T. Tybell, L Antognazza, K. Char, R. H. Hammond, M. R. Beasley, Ø. Fischer, J. –M. Triscone, Science, **276**, 1100 (1997).

[103] A. Roelofs, N. A. Pertsev, R. Waser, F. Schlaphof, L. M. Eng, C. Ganpule, V. Nagarajan and R. Ramesh, Appl. Phys. Lett. **80**, 1424 (2002).

[104] A. M. Bratkovsky and A. P. Levanyuk, Phys. Rev. B **63**, 132103 (2001).

[105] S. P. Alpay, I. B. Misirlioglu, V. Nagarajan, and R. Ramesh, Appl. Phys. Lett. **85**, 2044 (2004).

[106] V. Nagarajan, C. L. Jia, H. Kohlstedt, R. Waser, I. B. Misirlioglu, S. P. Alpay, and R. Ramesh, Appl. Phys. Lett. **86**, 192910 (2005).

[107] M. J. Haun, E. Furman, S. J. Jang, and L. E. Cross, Ferroelectrics **99**, 45 (1989).

[108] Jun Ouyang, S. Y. Yang, L. Chen, R. Ramesh, and A. L. Roytburd, Appl. Phys. Lett. **85**, 278 (2004).

---

[109] V. Nagarajan, A. Stanishevsky, L. Chen, T. Zhao, B.-T. Liu, J. Melngailis, A. L. Roytburd, R. Ramesh, J. Finder, Z. Yu, R. Droopad, and K. Eisenbeiser, Appl. Phys. Lett. **81**, 4215 (2002).

[110] L. Chen, V. Nagarajan, R. Ramesh, and A. L. Roytburd, J. Appl. Phys. **94**, 5147 (2003).

[111] R. Vaidya, R. J. Simonson, J. Cesarano III, D. Dimos, G. P. Lopez, Langmuir **12**, 2830 (1996).

[112] M. Aratani, T. Oikawa, T. Ozeki, and H. Funakubo, Appl. Phys. Lett. **79**, 1000 (2001). N. Nukaga, M. Saito, K. Okuwada and H. Funakubo, Jpn. J. Appl. Phys. **41,** L710 (2002).

[113] M. Shimizu, M. Okaniwa, H. Fujisawa, H. Niu, J. Eur. Ceram. Soc. **24**, 1625 (2004).

[114] J. Wang, J. B. Neaton, H. Zheng, V. Nagarajan, S. B. Ogale, B. Liu, D. Viehland, V. Vaithylyanathan, D. G. Schlom, U. V. Waghmare, N. A. Spaldin, K. M. Rabe, M. Wuttig and R. Ramesh, Science **299**, 1719 (2003).

[115] J. Wang, H. Zheng, Z. Ma, S. Prasertchoung, M. Wuttig, R. Droopad, J. Yu, K. Eisenbeiser and R. Ramesh, Appl. Phys. Lett. **85**, 2574 (2004).

[116] K. Y. Yun, M. Noda and M. Okuyama, Appl. Phys. Lett. **83**, 3981 (2003).

[117] Yu. N. Venevtsev, G. Zhadanov, and S. Solov'ev, Sov. Phys. Crystallogr. **4**, 538 (1960).

[118] G. Smolenskii, V. Isupov, A. Agranovskaya, and N. Kranik, Sov. Phys. Solid State **2**, 2651 (1961).

[119] C. Michel, J. M. Moreau, G. D. Achenbach, R. Gerson, and W. J. James, Solid State Commun. **7**, 701 (1969).

[120] J. R. Teague, R. Gerson and W. J. James, Solid State Commun. **8**, 1073 (1970).

[121] A. Maitre, M. Francois and J. C. Gachon, J. Phase Equil. and Diff. 25, 59 (2004).

[122] S. Y. Yang, B. T. Liu, J. Ouyang, V. Nagarajan, V. N. Kulkarni, J. Kidder, R. Droopad, K. Eisenbeiser and R. Ramesh, J. Electroceramics **14**, 37 (2005).

[123] M. De Keijser, P. J. Van Veldhoven and G. J. M. Dormans, Mat. Res. Soc. Symp. Proc. **310**, 223 (1993).

[124] S. R. Gilbert, S. Hunter, D. Ritchey, C. Chi, D. V. Taylor, J. Amano, S. Aggarwal, T. S. Moise, T. Sakoda, S. R. Summerfelt, K. K. Singh, C. Kazemi, D. Carl, and B. Bierman, J. Appl. Phys. **93**, 1713 (2003).

[125] F. Zavaliche, R. R. Das, D. M. Kim, S. Y. Yang, P. Shafer, C. B. Eom and R. Ramesh, submitted to Appl. Phys. Lett. (2005).

[126] V. Nagarajan, A. Stanishevsky, L. Chen, T. Zhao, B.-T. Liu, J. Melngailis, A. L. Roytburd, J. Finder, Z. Yu, R. Droopad, K. Eisenbeiser and R. Ramesh, Appl. Phys. Lett. **81**, 4215 (2002).

[127] J. Li, J. Wang, M. Wuttig, R. Ramesh, N. Wang, B. Ruette, A. P. Pyatakov, A. K. Zvezdin, D. Viehland, Appl. Phys. Lett. **84**, 5261 (2004).

[128] F. Kubel, H. Schmid, Acta Cryst. **B46**, 698 (1990).

[129] M. Polomska, W. Kaczmarek, and Z. Pajak, Phys. Status Solidi. **23**, 567 (1974).

[130] Yu. E. Roginskaya, Yu. N. Venevtsev, S. A. Fedulov, and G. S. Zhdanov, Sov. Phys. Crystallogr. **8**, 490 (1964).

[131] Y. H. Chu[a)], T. Zhao, Q. Zhan, S. Y. Yang, F. Zavaliche, M. P. Cruz, P. T. Joseph, I. N. Lin, D. G. Schlom, and R. Ramesh *will be submitted to* Appl. Phys. Lett.

[132] M. Polomska, W. Kaczmarek and Z. Pajak, Phys. Stat. Sol. (a) **23**, 567 (1974).

[133] H. Béa, M. Bibes, A. Barthélémy, K. Bouzehouane, E. Jacquet, A. Khodan, J.-P. Contour, S. Fusil, F. Wyczisk, A. Forget, D. Lebeugle, D. Colson, and M. Viret, Appl. Phys. Lett. **87**, 072508 (2005).